



**Gas-Cooled Fast Reactor (GFR)  
FY04 Annual Report**

Submitted September 30, 2004

## Contributors

### **Idaho National Engineering and Environmental Laboratory**

K. D. Weaver  
T. C. Totemeier  
D. E. Clark

### **Argonne National Laboratory-East**

E. E. Feldman  
E. A. Hoffman  
R. B. Vilim  
T. Y. C. Wei

### **Argonne National Laboratory-West**

J. Gan  
M. K. Meyer

### **Auburn University**

W. F. Gale

### **Massachusetts Institute of Technology**

M. J. Driscoll  
M. Golay  
G. Apostolakis

### **University of Nevada- Las Vegas**

K. Czerwinski

## Table of Contents

<b>1. Introduction .....</b>	<b>5</b>
<b>2. Design Options for the GFR.....</b>	<b>6</b>
2.1 <i>Reference Design .....</i>	6
2.2 <i>Optional Designs.....</i>	6
2.3 <i>GFR Fuel .....</i>	7
<b>3. GFR System Design and Integration .....</b>	<b>8</b>
3.1 <i>PRA Guided Design .....</i>	8
3.2 <i>System Integration .....</i>	9
<b>4. GFR Safety System Optimization and Transient Analysis Support.....</b>	<b>9</b>
4.1 <i>600 MWt Anticipated Transients without Scram.....</i>	11
4.1.1 Plant Description.....	12
4.1.2 Plant Model.....	15
4.1.3 Loss of Heat Sink.....	16
4.1.4 Small Leak Depressurization .....	20
4.2 <i>Core Layout Design .....</i>	23
4.2.1 Design Requirements and Constraints.....	24
4.2.2 Natural Convection Studies .....	24
4.2.3 Core Design Selection.....	29
4.2.4 Current Core Design .....	33
<b>5. GFR Materials for Moderate to High Temperature Use.....</b>	<b>38</b>
5.1 <i>CO2 Radiolysis Experiments .....</i>	38
5.2 <i>ODS Joining.....</i>	38
5.2.1 Transient Liquid Phase Bonding.....	38
5.2.2 Diffusion Bonding .....	41
5.2.3 Pressure Forge Welding.....	45
5.2.3.1 Background.....	45
5.2.3.2 Specimen Design .....	46
5.2.3.3 Parameter Development.....	46
5.2.3.4 Weld Cross-Sections.....	47
5.2.3.5 Tensile Test Results .....	48
5.2.3.6 Further Work.....	51
<b>6. GFR High Temperature Fuels.....</b>	<b>51</b>
6.1 <i>Screening and Down-Selection of GFR Fuel Concepts .....</i>	51
6.2 <i>Pin-Type Fuel.....</i>	52
6.2.1 Overview and Requirements.....	52
6.2.2 Fissile Phase Considerations.....	53
6.2.3 Cladding Selection.....	54
6.2.4 Reference and Alternate Concepts.....	55
6.3 <i>Particle Bed Fuel.....</i>	55
6.3.1 Overview.....	55
6.3.2 Fuel Design.....	55
6.3.3 Reference Concept.....	56
6.4 <i>Dispersion Fuel.....</i>	57
6.4.1 Overview.....	57

6.4.2	Dispersion Fuel Particle Concepts .....	58
6.4.3	Matrix Selection.....	62
6.4.4	Reference and Alternate Dispersion Fuel Concepts .....	69
6.4.4.1	Reference Dispersion Fuel Concept.....	69
6.4.4.2	Alternate Dispersion Fuel Concept.....	71
6.5	<i>Modeling to Determine the Feasibility of MA-bearing GFR Fuel</i> .....	72
6.5.1	Pin-type fuel.....	73
6.5.1.1	Vented Fuel pins .....	75
6.5.2	Dispersion Fuel .....	75
6.5.2.1	Macroscopic Stress Model.....	76
6.5.2.2	Microscopic Stress Model.....	79
6.6	<i>Ion irradiation of ZrC</i> .....	83
6.6.1	Experimental Procedure and Results .....	83
6.6.2	Discussion and Conclusion .....	89
6.7	<i>GFR Program Documents</i> .....	91
7.	<b>GFR Fuels Support</b> .....	<b>91</b>
7.1	<i>Fuel Material Interactions</i> .....	91
7.2	<i>ATR Calculations and Irradiations</i> .....	91
8.	<b>References</b> .....	<b>92</b>

## 1. Introduction

The gas-cooled fast reactor (GFR) was chosen as one of the Generation IV nuclear reactor systems to be developed based on its excellent potential for sustainability through reduction of the volume and radio toxicity of both its own fuel and other spent nuclear fuel, and for extending/utilizing uranium resources orders of magnitude beyond what the current open fuel cycle can realize. In addition, energy conversion at high thermal efficiency is possible with the current designs being considered, thus increasing the economic benefit of the GFR. However, research and development challenges include the ability to use passive decay heat removal systems during accident conditions, survivability of fuels and in-core materials under extreme temperatures and radiation, and economical and efficient fuel cycle processes. Nevertheless, the GFR was chosen as one of only six Generation IV systems to be pursued based on its ability to meet the Generation IV goals in sustainability, economics, safety and reliability, proliferation resistance and physical protection.

GFR funding for FY04 included FY03 carryover funds, and was comprised of multiple tasks. These tasks involved a consortium of national laboratories and universities, including the Idaho National Engineering and Environmental Laboratory (INEEL), Argonne National Laboratory (ANL), Auburn University (AU), the Massachusetts Institute of Technology (MIT), and the University of Nevada-Las Vegas (UNLV). The total funding for FY04 was \$400K, with FY03 carryover of \$486K. The cost breakdown can be seen in Table 1.1.

Table 1.1. GFR cost breakdown for FY04 (in \$k).

Activity (WP)	INEEL	ANL-W	ANL-E	AU	MIT	UNLV	TOTAL
GFR system design and integration (I0401J01)**	320				30		350
GFR materials for moderate to high temperature use (I0402J01)**	75			75	50		200
GFR fuels support (I0404J01)**	101					35	136
GFR high temperature fuels (A0404J01)		120					120
GFR safety system optimization and transient analysis support (A0401J01)			80				80
TOTAL	496	120	80	75	80	35	886

\*\*Includes FY03 carryover.

## 2. Design Options for the GFR

### 2.1 Reference Design

The reference GFR system features a fast-spectrum, helium-cooled reactor and closed fuel cycle (see Figure 2.1). This was chosen as the reference design due to its close relationship with the VHTR, and thus its ability to utilize as much VHTR material and balance-of-plant technology as possible. Like thermal-spectrum helium-cooled reactors such as the Gas-Turbine Modular Helium Reactor (GT-MHR) and the Pebble Bed Modular Reactor (PBMR), the high outlet temperature of the helium coolant makes it possible to deliver electricity, hydrogen, or process heat with high conversion efficiency. The GFR reference design uses a direct-cycle helium turbine for electricity (42% efficiency at 850°C), and process heat for thermochemical production of hydrogen.

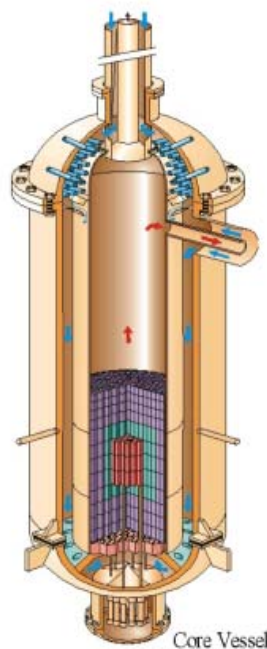


Figure 2.1. Possible GFR vessel and core configuration for block/plate core.

### 2.2 Optional Designs

The primary optional design is also a helium-cooled system, but utilizes an indirect Brayton cycle for power conversion. The secondary system of the alternate design utilizes supercritical CO<sub>2</sub> (S-CO<sub>2</sub>) at 550°C and 20 MPa (see Figure 2.2). This allows for more modest outlet temperatures in the primary circuit (~ 600-650°C), reducing the strict fuel, fuel matrix, and

material requirements as compared to the direct cycle, while maintaining high thermal efficiency (~ 42%).

The secondary optional design is a S-CO<sub>2</sub> cooled (550°C outlet and 20 MPa), direct Brayton cycle system. The main advantage of this design is the modest outlet temperature in the primary circuit, while maintaining high thermal efficiency (~ 45%). Again, the modest outlet temperature (comparable to sodium-cooled reactors) reduces the requirements on fuel, fuel matrix/cladding, and materials, and even allows for the use of more standard metal alloys within the core. This has the potential of significantly reducing the fuel matrix/cladding development costs as compared to the reference design, and reducing the overall capital costs due to the small size of the turbo machinery and other system components. The power conversion cycle is equivalent to that shown in Figure 2.2, where the IHX would be replaced by the reactor and reactor pressure vessel.

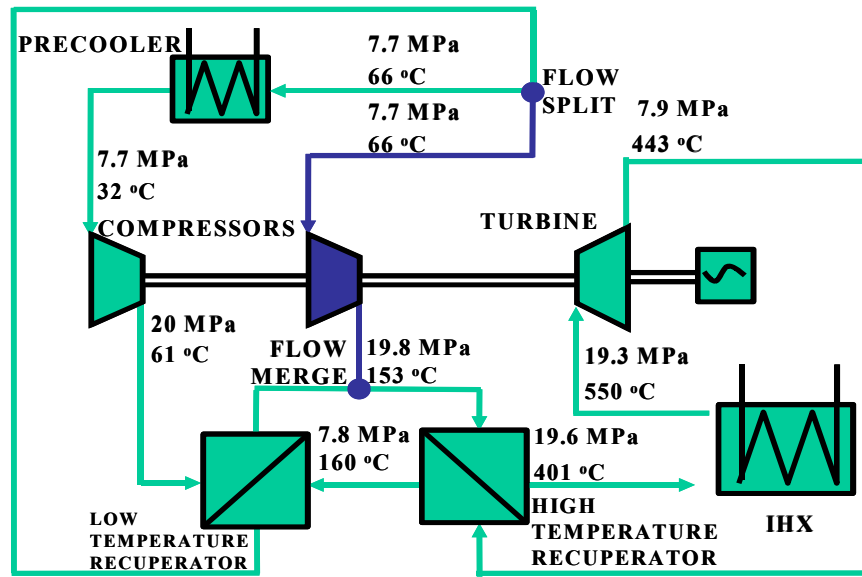


Figure 2.2. Schematic of the S-CO<sub>2</sub> recompression cycle.

## 2.3 GFR Fuel

The safety system design will be affected by the choice of primary coolant, whether a direct or indirect power conversion cycle is used, and the core geometry (i.e., block, plate, or pin). The trade-off between high conductivity and high temperature capabilities has led to the choice of ceramics, including refractory ceramics. The reference fuel matrix for the Generation IV GFR is a cercer dispersion fuel, based on a balance between conductivity and high temperature capability. Figure 2.3 is a graphical representation of two of the reference fuel types being considered.

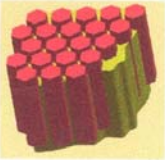


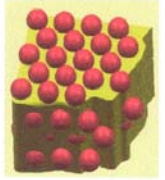

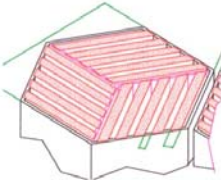
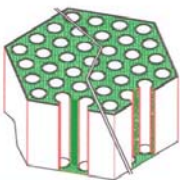
	Fuel	Fuel element	Sub-assembly
1- DISPERSION FUEL	Cylindrical or Hexagonal sticks 	Coated compact 	Pseudo-hexagonal sub-assembly with compact stack 
	Spheres / particles 	Coated plates 	Sub-assembly with plates  Prismatic block type with coated channels 

Figure 2.3. Dispersion fuel.

Current fuel designs are based on dispersion fuels (either as fibers or particles) in an inert plate/block type matrix, with an option to use solid solution fuel clad in a refractory ceramic (e.g., SiC/SiC composites). The reference fuels chosen for the GFR are UC and UN for their high heavy metal density, high conductivity, and minimal impact on neutron spectrum (although limited irradiation data exists). The matrix materials are dependent on the coolant and operating temperatures, and can be classified into three categories: ceramic (for high temperatures), refractory metal (for modest to high temperatures), and metal (for modest temperatures). As the fuels are of ceramic composition, the resulting fuel forms can be classified into two categories: cercler and cermet. The fuel fibers, or “sticks”, are to be extruded into the matrix, where the matrix has square lattice “honeycomb” appearance. The particles may be coated, but, unlike the thermal spectrum gas reactor fuel, will most likely have a single buffer coating to maximize the heavy metal content within the matrix.

It is important to note that fuel development, including fabrication and irradiation performance, is a key viability issue for the GFR, and cannot be separated from the safety design and performance of the GFR. Fuel mechanical and thermal properties are needed from beginning to end-of-life of the reactor to support the safety case, and will have a significant impact on the safety system design work. In addition, fuel development will include the viability of using minor actinide bearing material, which will have further affects on the performance of the GFR.

### 3. GFR System Design and Integration

#### 3.1 PRA Guided Design

PRA guided design task has identified options for improving reliability for various GFR systems. This includes:



- Identification of initiating events for the GFR system, where nine initiating events were used in the development of event trees for the baseline GFR PRA model.
- Candidates for improving on-site electric power reliability were identified; including the use of so-called “microturbines”. This approach will likely shift the focus to the electrical power distribution system as the limiting factor in loss of power causes.
- For PRA-guided design, an overall approach based on risk-informed decision making was formulated, objectives were defined, and steps were identified for application of multi-attribute utility theory (MAUT). An application to the shutdown/emergency cooling system is presented in a topical report at the Massachusetts Institute of Technology (MIT-GFR-008) published in March 2004, and released in April 2004, where it is shown that a mean core damage frequency of  $3.03 \times 10^{-7}$  is achievable using the current decay heat removal systems.

### **3.2 System Integration**

The Generation IV GFR R&D program is managed in the U.S. by the GFR System Integration Manager (SIM). The activities for the GFR SIM during FY04 include:

- Revision of the international R&D plan. Two revisions were issued, and answers to the comments/questions given by the GIF Experts Group were completed.
- Attendance at Steering Committee meetings, held in Belgium (January 2004), in Germany (April 2004), and in the United Kingdom (September 2004).
- Integration of Generation IV GFR activities with Advanced Fuel Cycle Initiative (AFCI) work, including attendance at the semi-annual meetings (Livermore, February 2004, and Salt Lake City, September 2004), and the periodic meetings of the Fuel Development Working Group.
- Coordination of other GFR related R&D currently funded by other sources.
- Promotion of the GFR at technical meetings, conferences, seminars, and special workshops.
- Reporting to DOE-NE on the technical progress and budget for GFR activities, and development/maintenance of the GFR R&D plan.

## **4. GFR Safety System Optimization and Transient Analysis Support**

In conjunction with the CEA-France/ANL-US I-NERI collaboration project [<sup>1</sup>] on the development of Gen IV advanced gas-cooled reactors with hardened/fast neutron spectrum, the Gen IV effort at ANL focused on safety system optimization and transient analysis support. The safety system optimization part of the effort has concentrated on low-pressure drop core designs for the large 2400 MWt plant option (economies-of-scale), while the transient analysis part of the effort has concentrated on the anticipated transient without scram (ATWS) response of the modular 600MWt plant. For both the 600MWt and 2400MWt plant options, the selected plant design is the direct cycle helium cooled system.

Several core designs exist [<sup>2</sup>] and are presently being assessed using several performance measures, including safety characteristics that are addressed here. The GFR differs from the thermal gas reactor in several respects important for safety behavior. Past studies of the thermal gas reactor operating under a direct cycle have shown that safety for unprotected accidents is assured largely as a result of a very low power density, and a combination of a high temperature to fuel failure, large Doppler feedback, and large thermal inertia. By contrast, the power density

in the GFR is an order of magnitude greater, the coolant density coefficient adds reactivity during depressurization accidents (which has no counterpart in the thermal core), and the absence of large blocks of graphite (thermal inertia). These fundamental differences give the reactivity feedbacks a more prominent role in the safety of the fast reactor compared to the thermal gas reactor. As a consequence, an important design objective is to engineer the fast reactor core to have sufficient inherent negative reactivity feedback that core power safely adjusts to the available heat sink.

Analyses of the ATWS behavior of a 600 MWt design, one of several proposed designs, have been performed [2]. In the ATWS events the reactor fails to scram following the transient initiator, and the control system is assumed to operate normally in response to the upset. In the case presented here, the initiators include loss of heat sink and slow depressurization. While a core layout and balance of plant exist for the 600 MWt design studied, the plant control system has not yet been designed. In part, the ATWS analysis was conducted to provide insight into control requirements for mitigating ATWS response. The ATWS analysis is performed with the GAS-PASS/H systems code [3]. This code models components as lumped parameter regions, and, through the use of a general purpose numerical solver, is designed to allow easy reconfiguration of plant equipment. This capability is used to study various options for location of the turbine bypass valve, and the effect of leak location on plant response. The code incorporates turbomachinery performance curves for modeling the balance of plant, and a core thermal model for computing reactivity feedbacks.

For the 2400 MWt gas-cooled fast reactor that is evaluated, the important aspect of the design is the removal of decay heat under depressurized conditions. Because the current fast reactor design is to have a power density of 100 W/cc, most of the decay heat must be removed by a flowing reactor coolant. A requirement that the reactor be passively safe during a total loss of power at the reactor site necessitates the employment of natural convection. Past studies have shown that natural convection is not effective at atmospheric pressure. Therefore, a guard containment that encloses the primary vessel is used to preserve a backpressure that maintains a high coolant density. During a total loss of site power, the leakage around the seals of the primary system will allow the reactor pressure to slowly decrease toward atmospheric pressure if it were not for the secondary (or guard) containment. The design goal is to limit the pressure that the guard containment must maintain, since the cost of the guard containment increases with its required pressure capability.

The pressure requirement of the guard containment is determined by the coolant density that permits sufficient natural convection through the reactor core during the prescribed off-normal or upset conditions. In a direct cycle reactor plant, the hydraulic resistance through the power conversion unit would essentially preclude natural convection flow. Therefore, one or more additional emergency cooling loops, that are isolated from the primary loop by check valves during normal operation, will be needed. Each of these loops will have an emergency heat exchanger (EHX), probably of the Heatric® printed circuit heat exchanger (PCHE) type, which will use natural convection to reject heat to the environment. The most significant hydraulic resistances in these loops are typically in the reactor core and the EHXs. Larger core resistances will require greater guard containment pressure capabilities. Therefore, the focus of the current effort is to design reactor cores with an absolute minimum hydraulic resistance.

The current focus is on a pin core, and the obvious way to minimize core hydraulic resistance is to design a short core with a large flow area and large coolant channels. The reactor vessel diameter, which is about 7 meters, limits the flow area. The radial reflector and shielding together are about 1 meter in width. Neutronic considerations, to a large extent, govern the coolant fraction, which limits the amount of the reactor cross-sectional area that can be allotted to coolant flow. Neutronic considerations also dictate the core fuel fraction. For a given fuel fraction, larger coolant channels are achieved by using a relatively small number of larger diameter pins. However, large diameter pins in large coolant channels have higher clad and fuel temperatures than do small pins in small channels. The fuel pins are to be uranium carbide pellets in a silicon carbide clad. For nominal full-power operation, the peak fuel and clad temperature limits are 1500°C and 1100°C, respectively. This report documents the work performed during this year on the neutronics and thermal-hydraulic calculations for the core design, and the essential iterations between the corresponding results.

#### **4.1 600 MWt Anticipated Transients without Scram**

The 600MWt plant safety analysis must address the class of upsets referred to as Anticipated Transients Without Scram (ATWS) events. These events are initiated by several different upset conditions where it must be shown that the plant control system is capable of maintaining a safe operating state following an assumed failure of the protection system to scram the reactor. The initiating events are normally expected to occur during the life of the plant. Umbrella initiating events include loss of electric load, inadvertent rod worth insertion, loss of Power Conversion Unit (PCU) heat sink, and depressurization from a slow leak. The first two initiations were scoped and results reported previously [4].

The loss of electric load event with turbine bypass was previously simulated with GAS-PASS/H. The shaft over-speed response presented by the loss of electric load is a characteristic of direct cycle gas reactors, and has been addressed in gas thermal reactor designs studies. The approach taken is, upon loss of load, to raise the outlet pressure of the turbine so that it is closer to the inlet pressure, thereby reducing the work performed by the turbine. This is achieved by diverting high-pressure compressor outlet coolant around the reactor and turbine. A bypass line could be connected from the compressor outlet to the recuperator hot side inlet. As the coolant leaving the compressor is several hundred degrees cooler than the point it is bypassed to, we refer to this as *cold turbine bypass*. This results in a power spike. The core power spike (in the first ten seconds of the transient) can be reduced by taking bypass flow from the cold side outlet of the recuperator, rather than the inlet. This is referred to as *hot turbine bypass*. The bypass coolant temperature is only 20°C below the reactor inlet temperature, and thus introduces only a negligible reduction on reactor inlet temperature upon opening the bypass valve.

These results indicate the plant control system is an important element for meeting both short and long term requirements for safe operation. It appears that all ATWS events will result in the generator being dropped from the grid. As a consequence, a fast-acting turbine bypass valve is needed to prevent shaft over-speed during the first few seconds of disconnection from the grid.

The outcome of the negative inlet temperature reactivity coefficient and low heat capacity of the GFR is that the bypass line should divert coolant from the outlet of the cold side of the recuperator rather than the inlet. The former minimizes the temperature change seen at the reactor with associated thermal stressing of core components and a related spike in reactivity. This initial control system strategy has been used for the follow-on results reported in this chapter.

#### 4.1.1 Plant Description

The plant analyzed is a single shaft machine with the turbine, a low pressure compressor, a high pressure compressor, and the electric generator all mechanically linked together. The coolant is helium gas and circulates through a direct cycle circuit as shown in Figure 4.1. The inlet to each compressor is cooled by a heat exchanger that is assumed to be cooled on its secondary side by liquid water that enters at the temperature of the environment. The secondary side is pressurized to remain single phase during all transients. The gas volumes and the mass of the structures associated with each of the primary system components are shown in Table 4.1 [5].

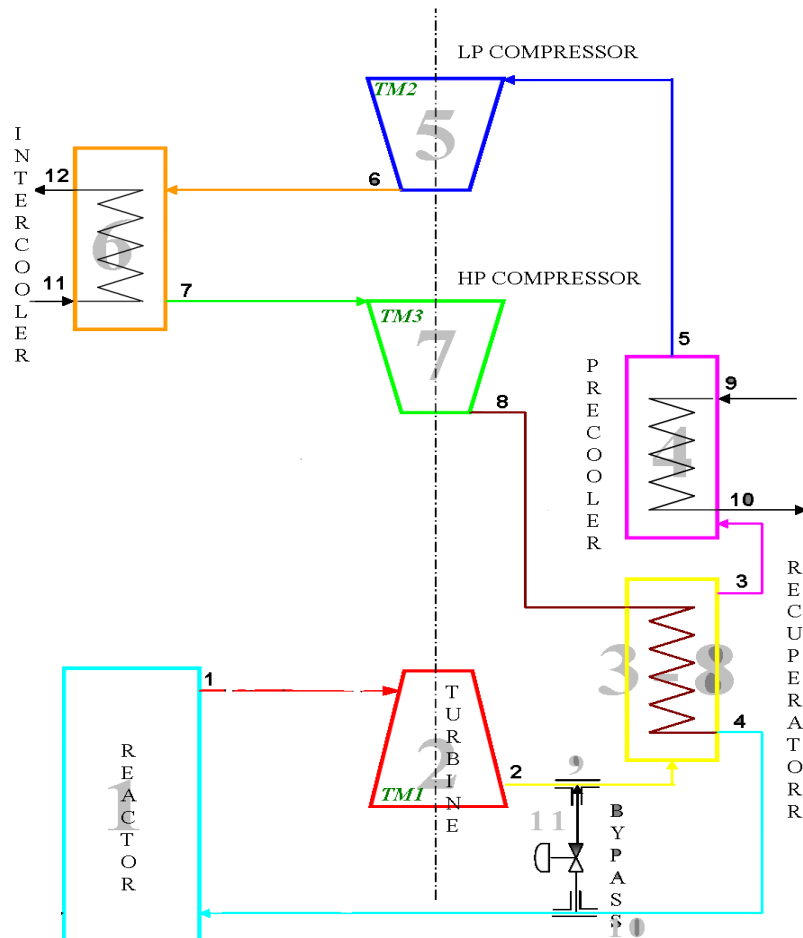


Figure 4.1. Schematic of Equipment Configuration during Operation with Hot Bypass of Turbine.

Table 4.1. Gas Volumes and Component Masses.

Component	Gas Volume (m <sup>3</sup> )	Structure Mass (MTonne)
Turbine	38	245
Recuperator-Hot Side	95	217
Recuperator-Cold Side	95	217
Precooler	177	199
Intercooler	174	211
High Pressure Compressor	38	245
Low Pressure Compressor	83	248

The core layout is shown in Figure 4.2. The reactor core consists of carbide fuel pins mounted on a high-nickel content steel (Alloy 800H) grid plate. The fuel pellets are (U,Pu)C and the cladding is SiC. The thermal-hydraulic model for the core is based on an average fuel pin as described earlier. Dimensions and the thermal-physical properties of the fuel pin materials are given in Ref. [4]. It is important to note that material properties for candidate core materials are critical. Ref. [4] lists thermal expansion coefficients for various materials and provides insight into the relative strength of reactivity feedbacks that rely on temperature induced geometry change. Note that Alloy 800H has a thermal expansion coefficient about twice the size of zirconium and niobium, two alternate materials. During ATWS upsets where the inlet temperature rises above the full power value, Alloy 800H will provide more negative reactivity and, as a result, reduced outlet temperature and power.

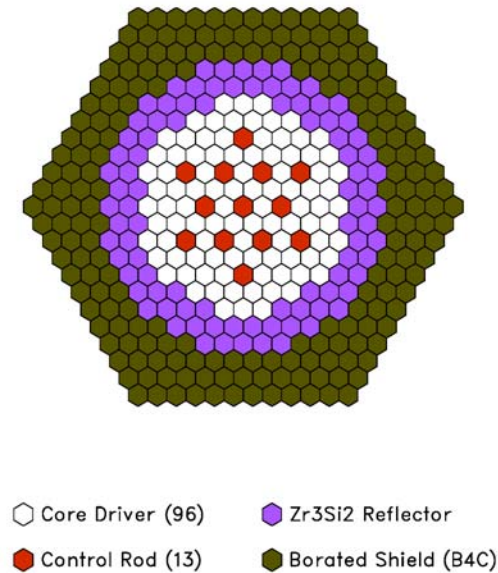


Figure 4.2. Core Layout for 600 MWt Gas Fast Reactor.

The steady-state operating conditions for the 600MWt Gas Fast Reactor are defined in this design project to be close to those of the GT-MHR. Table 4.2 shows these conditions. Also shown are the actual conditions predicted by GAS-PASS/H after specification of heat transfer areas and pressure drop data. The conditions obtained, while not identical, are sufficiently close for the purpose of studying ATWS behavior.

A normal operating requirement is that the shaft speed be maintained constant during load changes so that the generator remains synchronized to the grid. A requirement during loss of load events is that the shaft be prevented from over-speed when the mechanical load imposed by the generator goes to near zero. As discussed, the initial control system strategy developed previously [4] has this requirement as a control objective.

Table 4.2. Full Power Operating Condition for 600 MWt Gas Fast Reactor.

	Point Design Calculations	GASS-PASS/H
<b>Reactor</b>		
Core Power, MW(t)	600	600
Core Inlet/Outlet Temperatures, °C/°C	490/850	499/850
Core Upper Plenum Inlet Pressures, MPa	7.07	7.27
Helium Mass Flow Rate, kg/s	3.20	327
<b>Turbomachinery</b>		
Turbine Mass Flow Rate, kg/s	320	327
Turbine Inlet/Outlet Temperatures, °C/°C	850/510	850/519
Turbine Inlet/Outlet Pressures, MPa/MPa	7.02/2.65	7.17/2.8
Compressor Inlet/Outlet Temperatures, °C/°C	33/112	27/102
Compressor Inlet/Outlet Pressures, MPa/MPa	2.60/7.24	2.7/7.4
Compressor Overall Pressure Ratio	2.82	2.74
<b>Recuperator</b>		
Mass Flow Rate, kg/s	322	327
Hot Side Inlet/Outlet Temperatures, °C/°C	510/131	519/129
Cold Side Inlet/Outlet Temperatures, °C/°C	112/490	108/499
<b>Precooler</b>		
Mass Flow Rate, kg/s	322	327
Inlet/Outlet Temperatures, °C/°C	131/33	128/28
<b>Intercooler</b>		
Mass Flow Rate, kg/s	322	327
Inlet/Outlet Temperatures, °C/°C	112/33	103/28
<b>Power Plant</b>		
Thermodynamic Efficiency, %	50.5	49.3

### 4.1.2 Plant Model

The ATWS simulations were performed with the Gas Plant Analyzed and System Simulator/Hydrogen (GAS-PASS/H). This computer code is both fast running and easily reconfigurable for studying different component configurations of interest in safety analysis and control studies of GFR concepts. The capability for ease of reconfigurability is achieved through the use of modular components, where a general purpose equation solver provides for this. The code can be applied to the study of both direct and indirect cycle concepts.

Several capabilities are included for investigating aspects unique to direct cycle gas reactors. Of interest are the safety characteristics of single shaft plants during coastdown, and transition to shutdown heat removal following unprotected accidents, including depressurization, and requirements for safety grade control systems. Basic components provided include turbine, compressor, recuperator, cooler, bypass valve, leak, accumulator, containment, and flow junctions. The capability for flexible configuration of these components permits the safety consequences of alternate arrangements of components to be more easily assessed.

Models are available for the principal gas reactor systems components. The conservation equations are written for lumped regions in space. For a coolant volume, it is assumed that the incoming fluid mixes instantaneously (perfect mixing). In this case, the conditions at the outlet are the same as in volume interior. The inertia and acceleration pressure drop of the coolant is neglected in the momentum equation of the components. A general form of the time dependent energy and continuity equations are used to model the time dependent behavior of the system.

A nodalization diagram prepared for the plant is shown in Figure 4.1 and forms the basis for the conservation equations solved by GAS-PASS/H. A description of how the code interprets this diagram to configure a collection of components that form the plant system is given in [6]. Some definitions, however, prove useful before proceeding. A *node* is a collection of structure and/or coolant material at some average temperature representative of its energy content. A *component* is a piece of equipment whose behavior is represented by a set of conservation balances. A *link* is the connection between two components through which mass and energy are exchanged. A *state point* is that node in a component whose state variables feed into the next component via a link.

Each component appears as a single and unique color in the nodalization diagram and is labeled with a unique identifying integer. In Figure 4.1, the component numbers appear as large lightly shaded integers inside each component. The state points are also labeled with uniquely identifying integers. In Figure 4.1 the state points appear as bold integers at the links. For example, the turbine is component number “2”. It takes its input from state point “1” of the reactor. The turbine output appears at state point “2”. The information in the nodalization diagram is used to compose inputs and outputs for component software modules that contain the conservation balances. When all components in the network diagram have been cast as calls to these software modules, numerical solution procedures solve for the plant conditions. The software module for a component has an interface (subroutine call) that the user configures so that the component interacts with other components according to the network diagram. The interface provides access to input process variables and output process variables. The input variables are the forcing functions that drive the component and are either process variables at

state points in other components that link with the component or are user supplied forcing functions. The output variables are at the state point where the component response appears. Each component must be represented by a call to a component module with the input variables in the module set as just described. One sees that for two linked components, the output variables from the upstream module will be the input variables to the downstream module.

#### **4.1.3 Loss of Heat Sink**

In the Loss of Heat Sink event, the normal means for heat removal is lost. In the GFR this would encompass the intercooler and precoolers. With the loss of heat removal, the ability of the turbomachinery to perform work is diminished. However, the generator remains connected to the grid and continues to present the same mechanical load to the shaft. As a consequence of the torque imbalance, the shaft speed begins to decrease. The near term objective in this situation is to maintain shaft speed so that coolant continues to circulate around the primary system, removing the core heat. For the long term, the core power must be lowered to bring it into equilibrium with the shutdown heat removal system heat removal capacity. Since active means of adding negative reactivity is assumed unavailable, the design must rely on inherent temperature reactivity effects.

The simulation begins with the loss of the precoolers and intercoolers to remove heat while the plant is at full power. The heat removal rates are supplied as forcing functions and they are shown in Figure 4.3. The heat removal rates go to a very low value over 5 seconds beginning at 25 seconds. In response, the shaft speed begins to decrease as described above, and as shown in Figure 4.4. At 28 seconds, the speed has dropped to 90 percent, at which time the generator is assumed to trip from the grid as shown in Figure 4.4. As a consequence of the loss of generator mechanical load, the shaft speed accelerates. At 28.4 seconds, the bypass valve opens as the shaft speed control attempts to maintain constant speed. The flowrate through the turbine (and core) is reduced as seen in Figure 4.5 as the pressure at the turbine outlet rises. In general, the low pressure side of the plant rises as seen in Figure 4.7 as the bypass valve redirects high pressure side coolant to the low pressure side. With the loss of the coolers, the temperature at the outlet of the coolers rises, and this rise propagates to the reactor inlet. The increase in reactor inlet temperature is seen in Figure 4.6. The reactivity components of the reactivity driving the core are shown in Figure 4.8. The coolant density reactivity initially goes positive as the core pressure initially decreases with a decrease in outlet pressure of the high pressure compressor, due to the initial shaft speed decrease. However, when the speed recovers to a value above the full power value, the core pressure rises above the full power value and the coolant density reactivity becomes negative. Core coolant density temperature dependence introduces positive reactivity, but is a smaller component than that due to pressure. Overall, the temperature reactivity components introduce negative reactivity as seen in Figure 4.8, and are responsible for the reduction in core power seen in Figure 4.4.



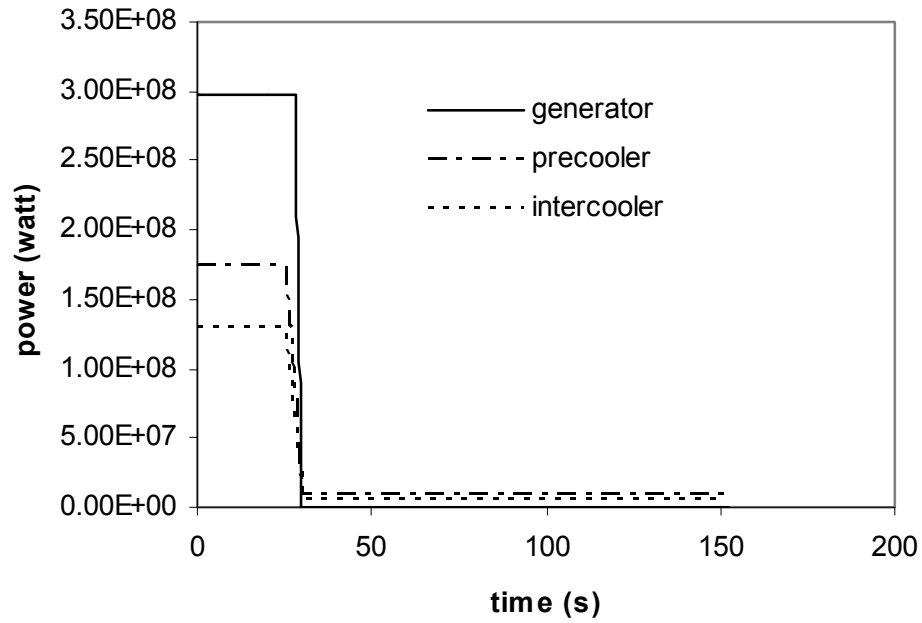


Figure 4.3. Forcing Functions for Unprotected Loss of Heat Sink: Hot Bypass of Turbine.

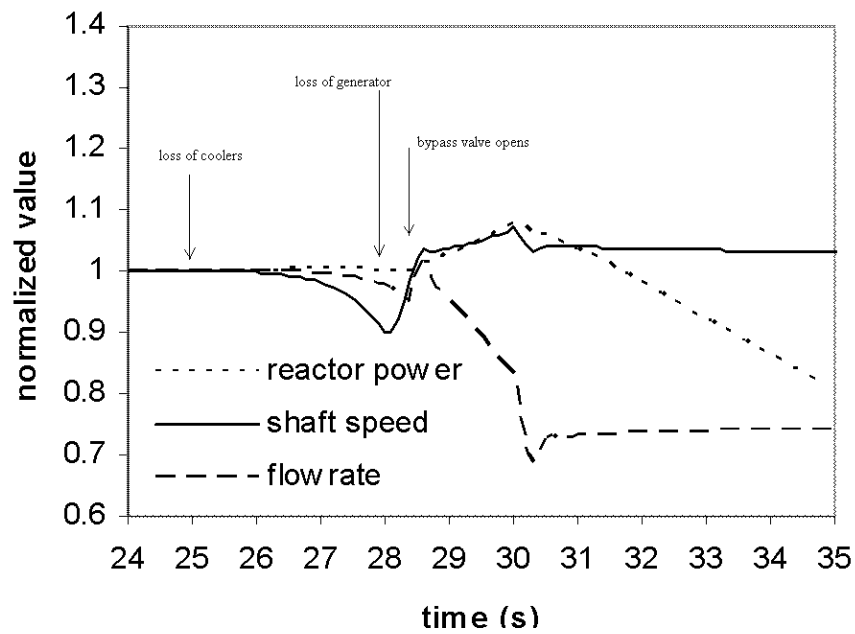


Figure 4.4. Normalized Reactor Power and Flowrate and Turbomachinery Shaft Speed Response for Unprotected Loss of Heat Sink: Hot Bypass of Turbine.

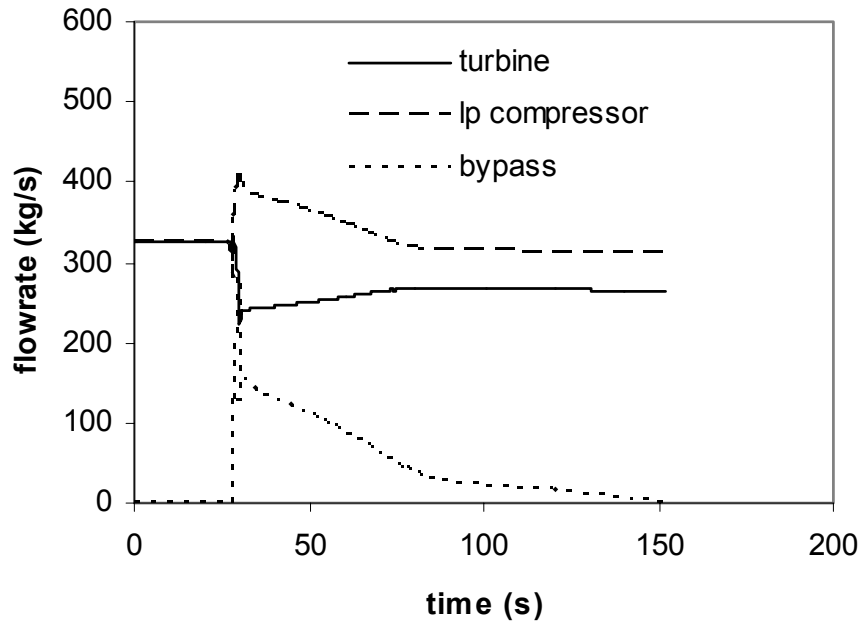


Figure 4.5. Turbine, Bypass and Compressor Mass Flowrates for Unprotected Loss of Heat Sink: Hot Bypass of Turbine.

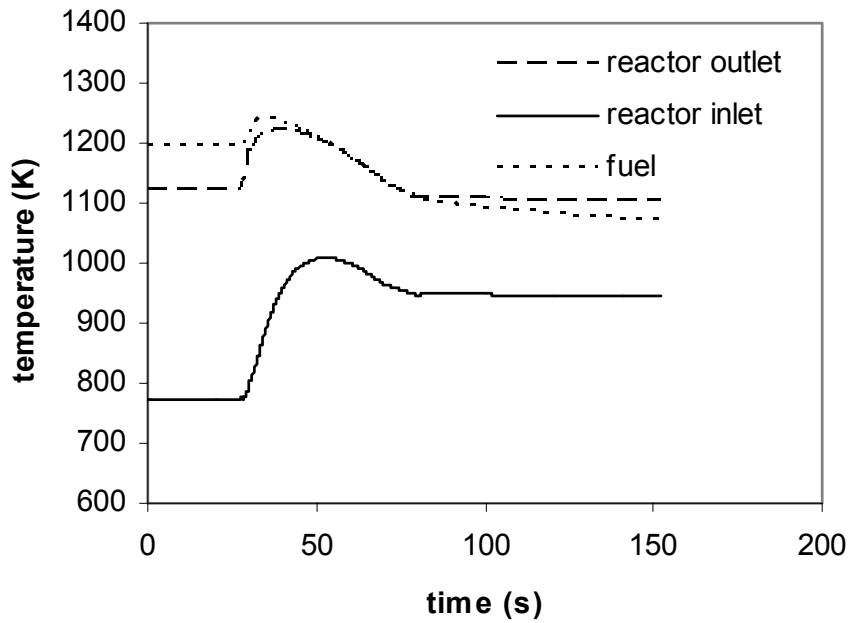


Figure 4.6. Reactor Core Temperatures for Unprotected Loss of Heat Sink: Hot Bypass of Turbine.

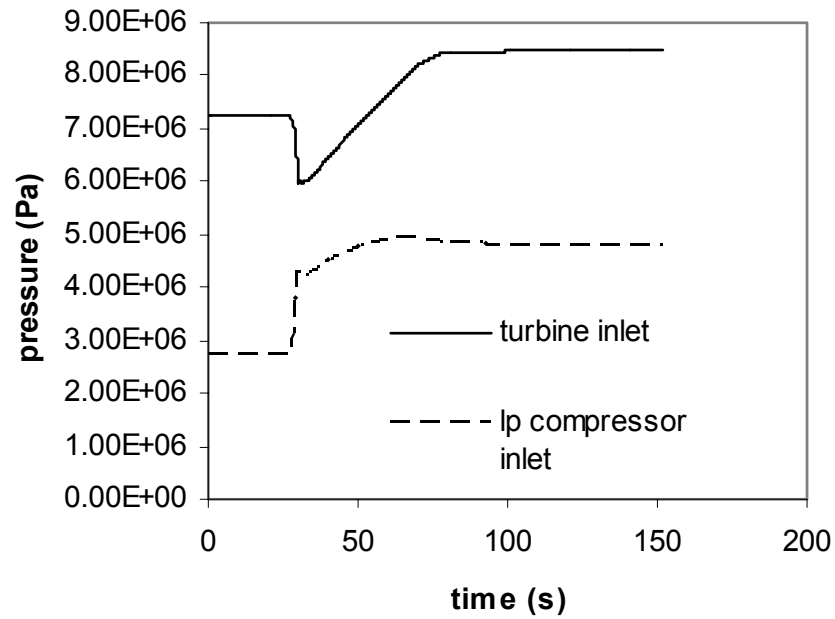


Figure 4.7. Power Conversion System Pressures for Unprotected Loss of Heat Sink: Hot Bypass of Turbine.

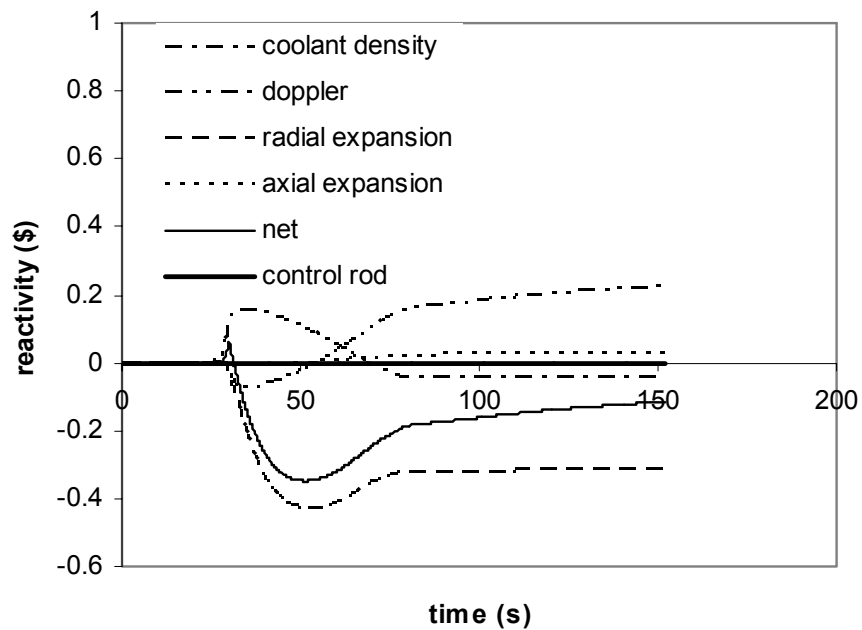


Figure 4.8. Reactivity Components of Core Response for Unprotected Loss of Heat Sink: Hot Bypass of Turbine.

#### 4.1.4 Small Leak Depressurization

A small leak in the primary system will result in helium loss, and a gradual depressurization of the primary system. The behavior of the plant for a small leak, defined here as a leak that reduces primary system pressure from 7 MPa to 2MPa over a period of 3600 seconds, was investigated. We assume that the generator remains connected to the grid, and that it presents a constant mechanical load to the shaft. The leak flowrate is supplied as a forcing function and is shown in Figure 4.9. The leak occurs at the outlet to the high pressure compressor.

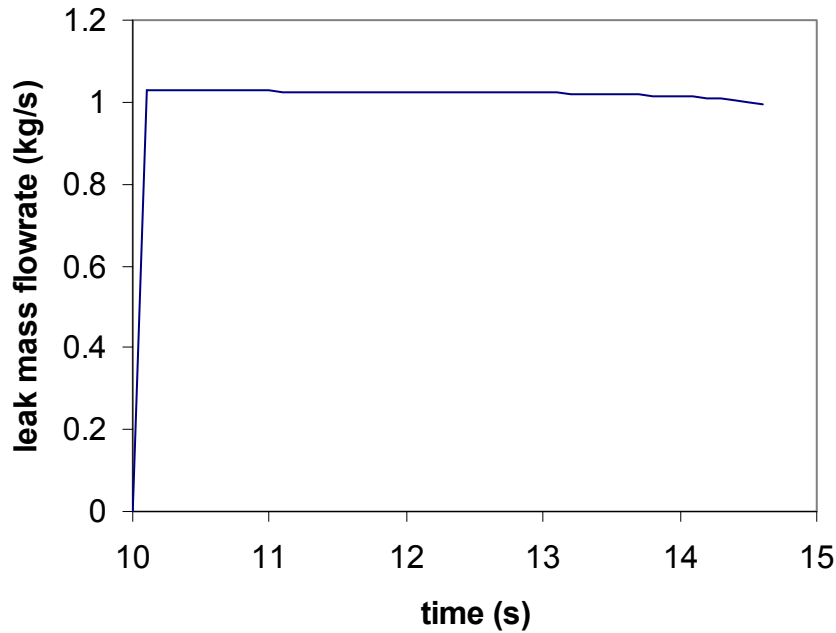


Figure 4.9. Forcing Functions for Unprotected Small Leak Depressurization: Hot Bypass of Turbine.

As gas is lost from the plenum at the outlet of the high pressure compressor, the pressure in the plenum is reduced. This is essentially the same pressure seen at the turbine inlet. As the pressure at the turbine inlet decreases, as seen in Figure 4.13, the pressure differential across the turbine decreases. This decrease results in a reduction in mechanical power by the turbine and, hence, a reduction in shaft speed, as seen in Figure 4.10, as the mechanical load of the generator remains constant. As the shaft speed decreases, the power of the compressors decreases. This, in turn, results in decreased pumping power and reduced flowrate, as seen in Figure 4.10. Shaft speed decreases as a result, and the process repeats. Essentially, the natural processes regulating the shaft speed are unstable and the speed rapidly decreases. Figures 4.11 and 4.12 show the corresponding flowrates and temperatures.

The stability of the system for the small leak is strongly dependent on the efficiency curve for the compressors and the selection of the full power operating point. Note in Figure 4.10 that the flowrate to speed ratio increases during the transient. The full power operating point of the compressors is to the right of the peak efficiency point on the compressor efficiency curve. Hence, as flowrate to speed ratio increases, compressor efficiency decreases. This would appear to be the source of the instability. Placing the full power operating point to the left of the peak efficiency point would provide an increase in efficiency with flowrate to speed ratio increase. Thus, compressor power would increase and tend to drive flowrate to speed in the desired direction providing a more stable response.

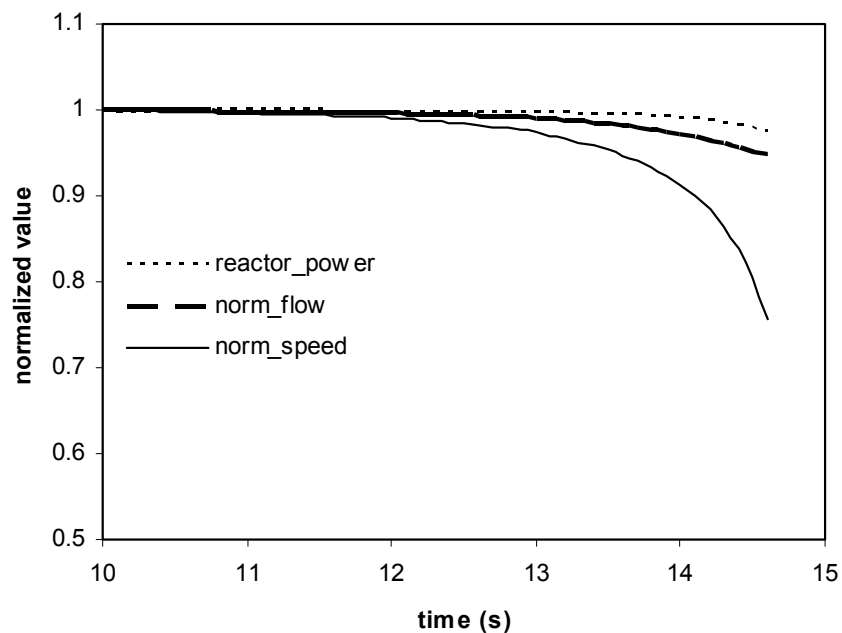


Figure 4.10. Normalized Reactor Power and Flowrate and Turbomachinery Shaft Speed Response for Unprotected Small Leak Depressurization: Hot Bypass of Turbine.

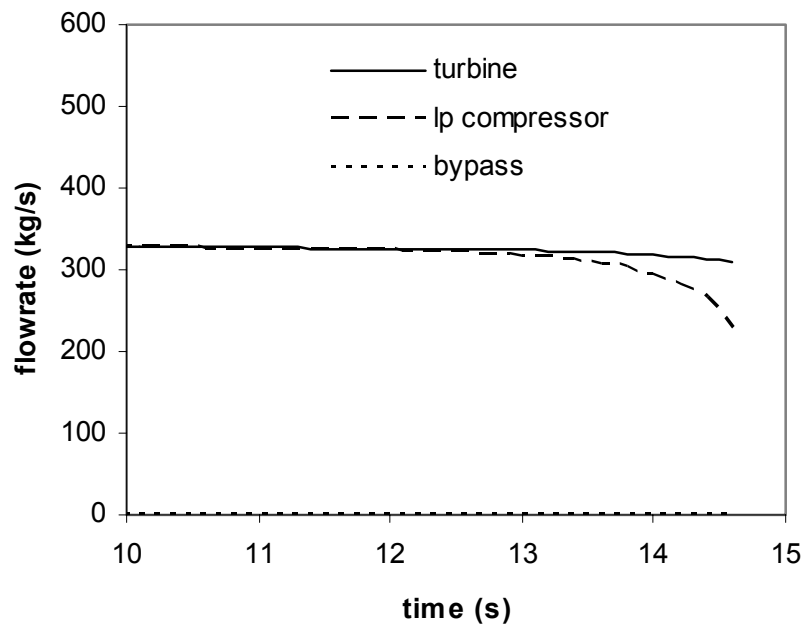


Figure 4.11. Turbine, Bypass and Compressor Mass Flowrates for Unprotected Small Leak Depressurization: Hot Bypass of Turbine.

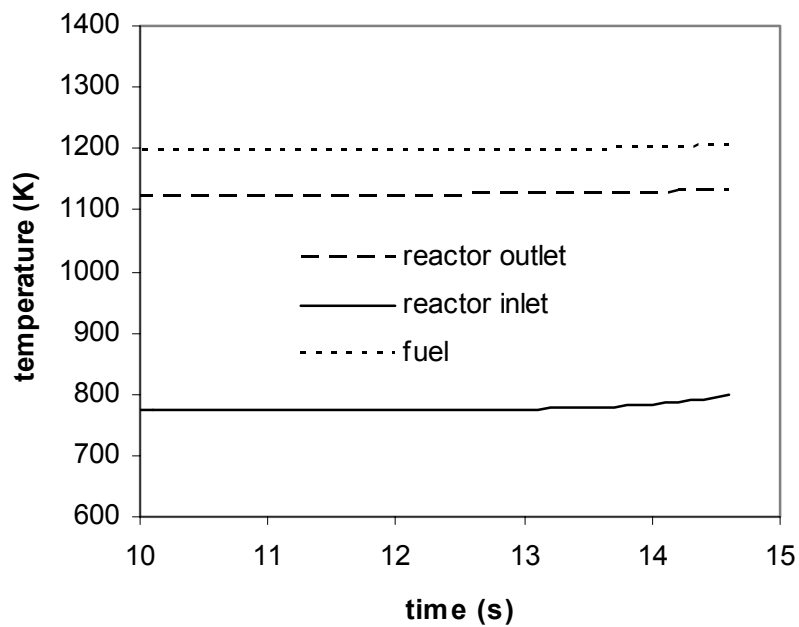


Figure 4.12. Reactor Core Temperatures for Unprotected Small Leak Depressurization: Hot Bypass of Turbine.

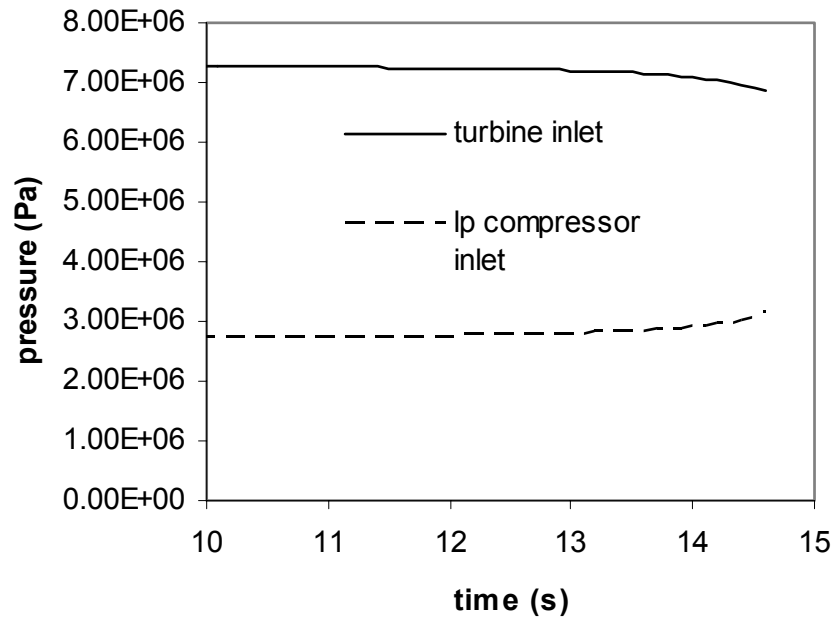


Figure 4.13. Power Conversion System Pressures for Unprotected Small Leak Depressurization: Hot Bypass of Turbine.

## 4.2 Core Layout Design

Based on economy of scale, a 2400 MWt core has been analyzed. The approach to the problem is to find a 2400 MWt core design that meets the steady state, full-power design requirements, and has as low a pin-bundle pressure drop as needed. To establish the criteria on designed core pressure drop, a steady-state thermal-hydraulic analysis of the natural convective loop used for decay heat removal is performed. Decay heat generation rates up to 3% of full power are considered, and the required primary system pressure for each decay power level is determined. For all calculations, the natural convective head was produced by coolant temperature differences around the emergency heat removal coolant circuit. The hydraulic model of this loop balances the buoyancy head with the pressure drops produced by hydraulic resistances, such as those of the core and the EHXs. The distance from the top of the fuel pins to the top of the EHXs was assumed to be 10 meters. The layout of the core subassembly at these natural circulation conditions is selected on the basis of the acceptable primary system pressure at the chosen decay heat level. A single basic pin core design layout is considered. This is the conventional configuration with the pins aligned vertically, which then produces the steady-state pressure drop during normal operation. This should be consistent with the pumping power studies conducted previously for the 600 MWt core design.

### 4.2.1 Design Requirements and Constraints

During normal full-power operation, the reactor power is 2400 MWt and the inlet and outlet temperatures are specified as 480° C and 850° C, respectively. The reactor coolant is helium at 7.0 MPa. Since the coolant enthalpy rise between the reactor inlet and outlet is equal to the reactor power, the helium flow rate is 1249 kg/s.

In most cases the core power density was taken to be 100 W/cc. Since the core power is 2400 MWt, and the power density is 100 W/cc, the core volume must be 24 m<sup>3</sup>. The lowest pressure drop in a conventional core design is obtained by distributing the volume so that core is short and the cross-sectional area is large, i.e., short coolant subchannels with low flow velocities. The neutronic design took this and the diameter of the reactor vessel into consideration, and performed parametric studies that varied the core height-to-diameter ratio. This ratio, together with the power density, determines the equivalent core diameter and the core height. The neutronic design also requires assumptions regarding the fraction of the core that is voided (gas). This includes the fission gas inside the pins, the stagnant coolant between adjacent subassemblies, the material inside the control rod thimbles, and the flowing coolant used to cool the pin bundles. After allowances were made for the first three items that are classified as gas, the only fraction of the core gas cross-sectional area that remains is for the flowing coolant used to cool the core. Power densities other than 100 W/cc were considered to a lesser extent. The remaining core fraction is divided between fuel and structural material. Note that this is from a neutronic design perspective.

From the fuel pin performance perspective, another constraint for a conventional pin design is that each pin has an upper and a lower reflector, and a gas plenum volume for the fission gas. These add about 1 meter of unheated length to both the top and the bottom of each fuel pin. Spacer grids separate the fuel pins within each pin bundle, and it is assumed that these grids are axially spaced 25.4 cm (10 inches) apart.

From the subassembly thermal-hydraulic design perspective, since the core height, overall pin length, and coolant flow area have been specified by the neutronic design and the fuel performance design, the only parameter that can be adjusted to minimize pressure drop is the number of fuel pins. Using a minimum number of pins can minimize pressure drop. As the number of fuel pins is decreased, the average linear power (or power of each pin per unit length of the core) must be increased, and the cross-sectional area of each pin must also increase so that the cross-sectional area occupied by coolant and the cross-sectional area occupied by fuel pellets both remain unchanged. This also leads to a larger spacing between adjacent pins, which correspond to a larger hydraulic diameter for the subchannels within the pin bundles. Greater linear pin powers and larger hydraulic diameters each produce greater clad and fuel temperatures. Thus, there is a trade-off between fuel bundle pressure drop and fuel pin temperatures.

### 4.2.2 Natural Convection Studies

As indicated at the outset, a low pressure drop core design is being sought in order to facilitate natural convection in the emergency cooling loop during depressurized conditions when the reactor is shutdown. An important issue is how low the hydraulic resistance of pin-bundle must be in order to facilitate sufficient natural convection at shutdown conditions. This, of course,



depends on what the pressure is during depressurized conditions. The decay heat curve is shown in Figure 4.14. Uranium fueled reactors reach a decay power level of 2% within 15 minutes of reactor shutdown. Therefore, this decay power level could be considered to be a reasonable maximum capability for the emergency cooling loop. The integrated decay energy is shown in Figure 4.15 for a set of constant heat losses (%). It can be seen that peak fuel energy deposition is determined at the point where the after-heat decays below the decay heat removal capability. However, an equally important consideration is the level of the decay heat. Furthermore, Figure 16 shows that at a power density of 100 W/cc, the stored energy of 4.6 fps occurs for a temperature change of 500°C. This 4.6 fps occurs at 2% heat removal capacity. The potential for 400-500°C change in fuel temperature during the depressurized decay heat accidents without violating the fuel coating criteria of 1600°C is possible because the core coolant inlet temperature can be dropped by ~400°C with emergency water cooled heat exchangers. The 2% level decay heat will therefore be used as the starting point for the design calculations.

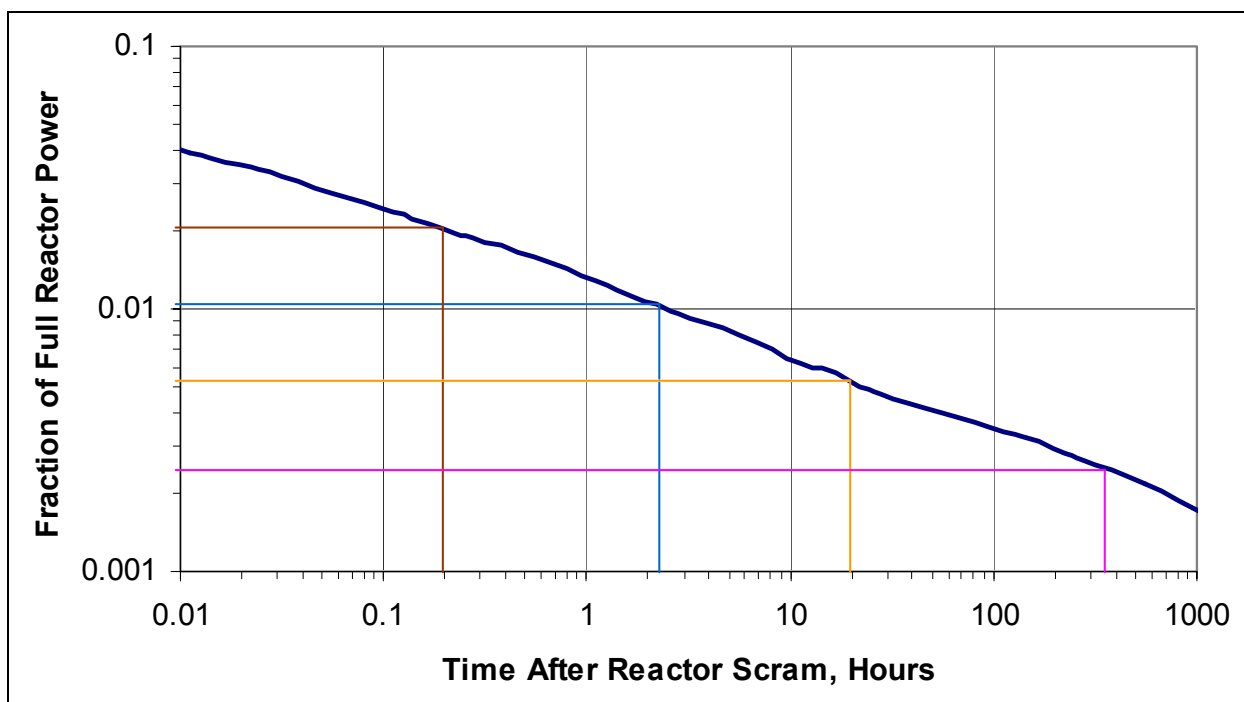


Figure 4.14. Decay Heat Curve for Uranium-Fueled Reactors

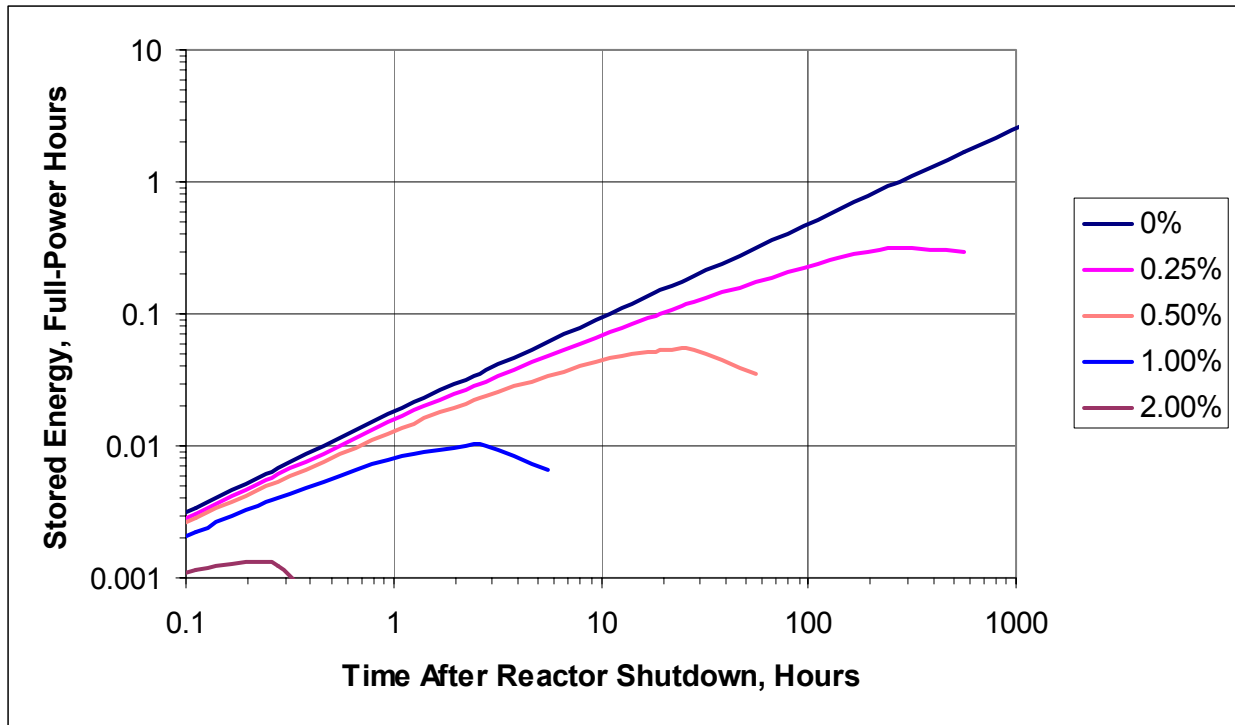


Figure 4.15. Stored Energy for Parametric Values of Decay Heat Removal Rate.

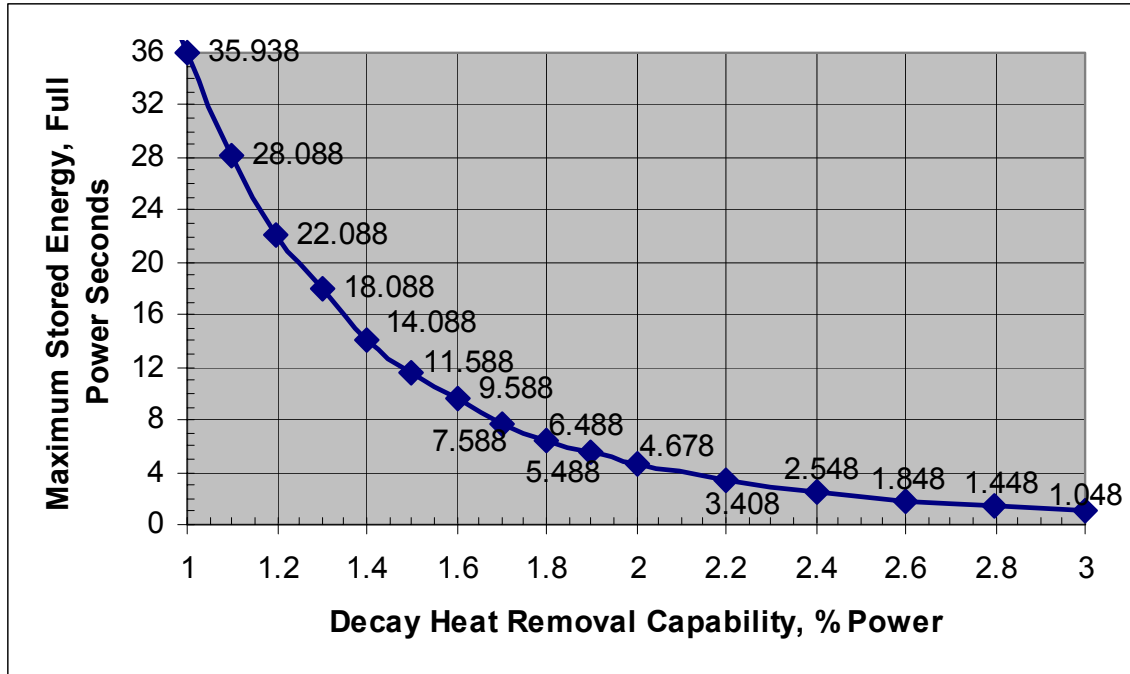


Figure 4.16. Maximum Stored Energy.

- Stored Energy (fps)

$q''' \text{ wcc} \delta T^{\circ}\text{C}$	100	250	500
50	1.8	4.6	9.2
100	0.9	2.3	4.6

$$\text{Fps} = \frac{\delta T}{q''' / \rho c}$$

For carbide fuel pin and  $\text{VF}_{\text{fuel}} = 0.25$

Cores of various pin-bundle full-power pressure drops were analyzed as part of the emergency cooling loop, at the reference decay heat level. The only hydraulic resistances in these loops are the pin-bundle and the EHX. Note that the hydraulic resistance of the EHX can be much larger than that of the pin-bundle. The EHX design was assumed to be that used in the earlier 600 MWt gas-cooled reactor studies. However, it was assumed that in the current study that four times as many parallel units would be used, since the current reactor is to have four times the power. In one of the studies, a bounding calculation was done in which the hydraulic resistance of the EHX was essentially eliminated. This, in concept, could be accomplished by having a very large number of parallel heat exchanger units. Parametric studies were performed on a number of core pressure drops (100% steady state operation) by varying the core-height-to-diameter ratio.

One of the first 2400 MWt 100 W/cc designs considered had a core height-to-diameter-ratio of 0.1, corresponding to a core height of 0.674m and a core equivalent diameter of 6.74m. For this geometry, the peak clad temperature was at its limit of 1100°C. The corresponding peak fuel temperature of 1174°C was easily within its 1500°C limit. It was assumed that 11 grid spacers were needed, one every 25.4 cm (10 inches). The pin-bundle pressure drop was found to be 0.1304 bars for this design. Although this pressure drop is extremely low, the core diameter is too large for a 7-m diameter reactor vessel, when 1 m of radial reflector and shielding is included around the core. Also, the flowing coolant fraction of 0.5525 was larger than what the current neutronic design allows. Another early design had a core height-to-diameter ratio that was only 0.2, corresponding to a core height of 1.069 m and a core equivalent diameter of 5.25 m. This design had 12 grid spacers, a pin-bundle pressure drop of 0.2823 bar, a peak clad temperature of 1100°C, and a peak fuel temperature of 1213°C. The third design, for which natural convection was studied in the emergency cooling loop, was the 0.5042 bar pin-bundle core that is the current reference design.

In the natural convection studies, steady-state analyses were performed for various decay power levels between 0.2% and 3% of full power. The reactor coolant inlet temperature was assumed to be 250° C, which is assumed to be the temperature exiting the primary-side of the EHX. The maximum allowed reactor coolant temperature was assumed to be either 900 or 1600° C. The former is a realistic value if the failure of structure components is to be avoided. The higher value is the maximum allowed fuel temperature and was considered only to show the sensitivity of the results to choice of allowed coolant outlet temperature. For each decay power level selected, spreadsheet solvers were used to determine the loop, or system, pressure that would be needed to achieve the prescribed outlet temperature (900 or 1600° C) under steady state conditions. Both helium and carbon dioxide coolants were considered for each of the two reactor outlet temperatures. For the carbon dioxide coolant, the length of the emergency heat exchange was assumed to be 0.5 m, which is twice as long as that assumed for the helium cases. This assumption is a result of the earlier studies of the 600 MWt GFR. Results for the 0.5042 bar case are provided in Figure 4.17. For the 0.5042 bar reference design with helium coolant, and an allowed outlet temperature of 900°C and a decay power level of 2% of full power, the guard containment would have to maintain the emergency loop pressure at 22.3 bar.

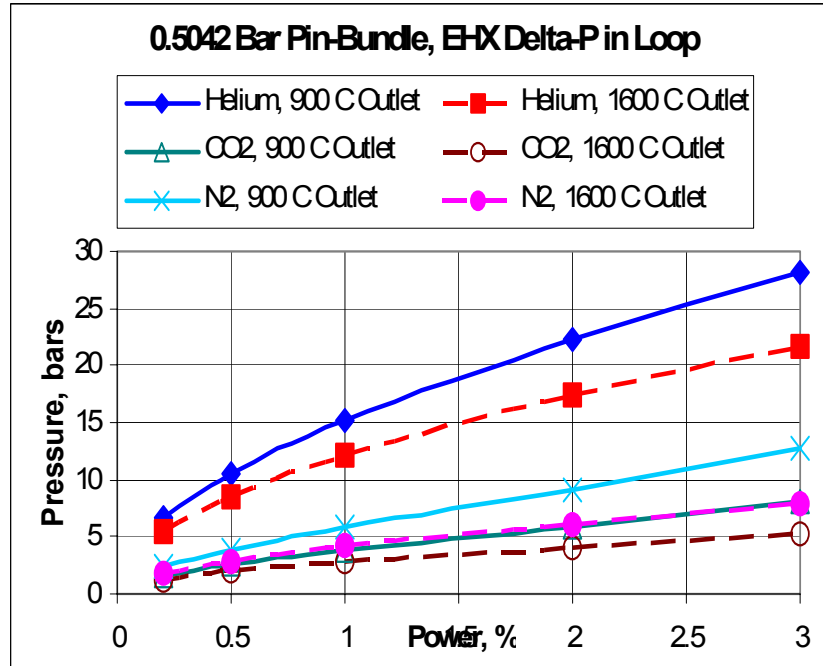


Figure 4.17. Natural Convection for the 0.5042-Bar Pin-Bundle Core.

### 4.2.3 Core Design Selection

For the 0.5042 bar core design, a study was performed in which the fraction of the total core cross-sectional area allocated to flowing coolant was varied. Although about 65% of the core cross-sectional area is gas in the reference design, only about 50% is flowing and available to cool the fuel pins. The pin-bundle pressure drop, due to friction and form losses, was maintained at the reference value of 0.5042 bar. For reasons that will be explained in Section 4.3, the peak clad temperature was maintained at 1105.5° C instead of 1100° C. The core power density was maintained at 100 W/cc. Sample results of the study are shown in Figures 4.18 and 4.19 for the core height variation and the linear power variation. Eight steady state solutions were obtained and are represented by the eight points on each of the figures. As the flowing coolant fraction is increased, the core becomes taller and smaller in diameter in order to maintain the pressure drop while keeping the volume fixed. This is shown in Fig. 18. In each solution, the clad temperature was maintained by appropriately adjusting the number and diameter of the fuel pins, which are assumed to be in a triangular pitch. The clad thickness was held constant at 0.4 mm and the fuel fraction was maintained at 22.1% of the total core cross sectional area. These constraints caused an inconsistency between the fuel and clad dimension for the two highest coolant volume fractions studies. For the one at 0.595, the fuel pellet diameter interfered with the clad inner diameter; and for the case at 0.680, the fuel pellet diameter was larger than the pin diameter. Thus, the results for these last two points are suspect. Corresponding to Figure 4.18 for the 0.5042 bar case, Figure 4.20 shows the core height-to-diameter variation for a set of core pressure drop design cases ranging from 0.5 bar to 2 bar. The dependence upon flowing coolant volume fraction shows similar behavior. These figures only show the thermal-hydraulic behavior of the various possible subassembly designs. To narrow down the selections, the neutronic criteria also have to be involved. Figure 4.21 shows the corresponding neutronic core design results for the similar case height-to-diameter ratio versus coolant volume fraction plot.

The design parameters which are varied are: 1) the number of fuel batches from three to six, 2) the clad material, ODS and SiC, and 3) the fuel composition, ANL TRU and Recycle TRU. The fuel target burnup is maintained at 10%. This is for the breakeven core design (conversion ratio = 1.0), which meets the Gen IV GFR top level design goal of sustainability. Since the current candidates are SiC cladding and homogeneous recycle, this curve is utilized together with the thermal-hydraulic results from Figure 4.20 to better define the subassembly design. Figure 4.22 presents the results. It will be seen that the combined T-H results and the neutronic results give a core design with height-to-diameter ratio of 0.282, and a gas volume fraction of 0.59 at a core pressure drop of 0.5 bar.

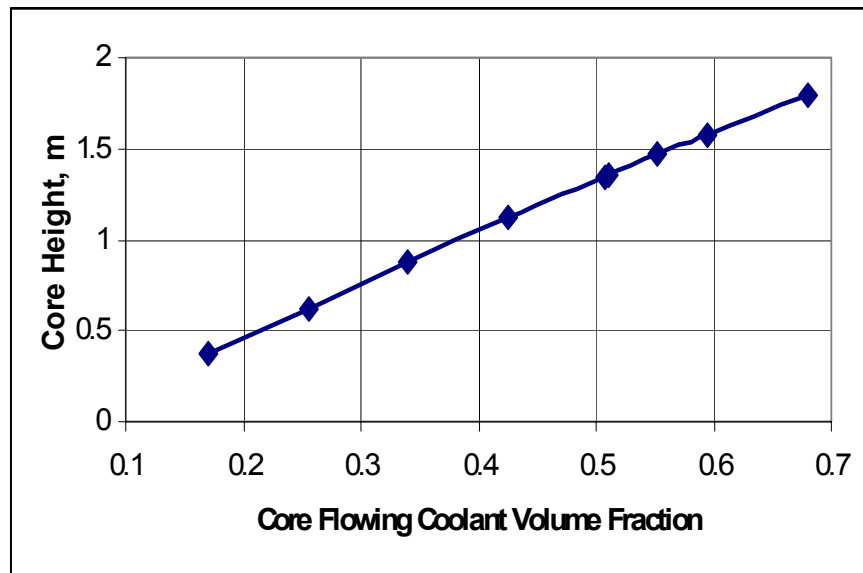


Figure 4.18. Sensitivity of Core Height to Variations in Core Flowing Coolant Volume Fraction in 0.5042-Bar Reference Design.

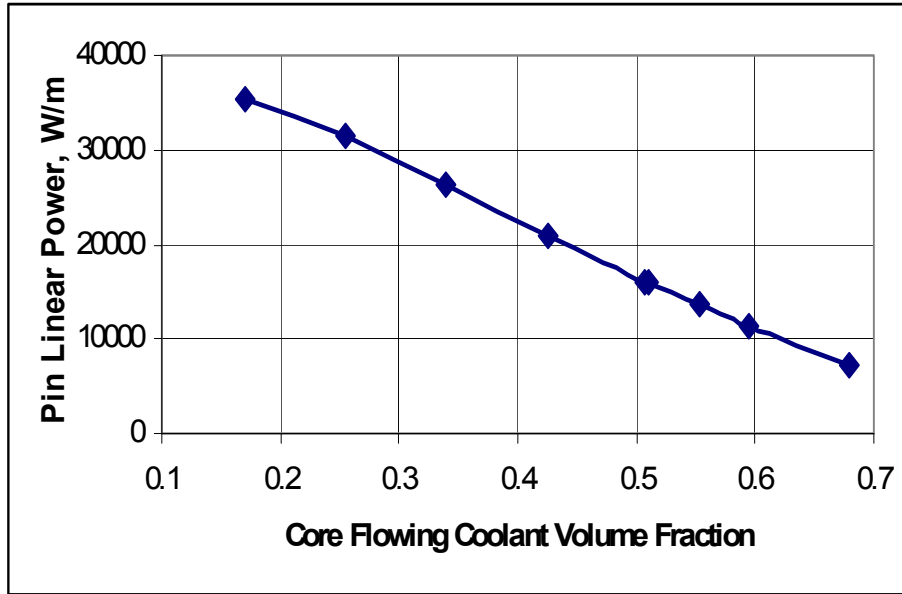


Figure 4.19. Sensitivity of Pin Linear Power to Variations in Core Flowing Coolant Volume Fraction in 0.5042-Bar Reference Design.

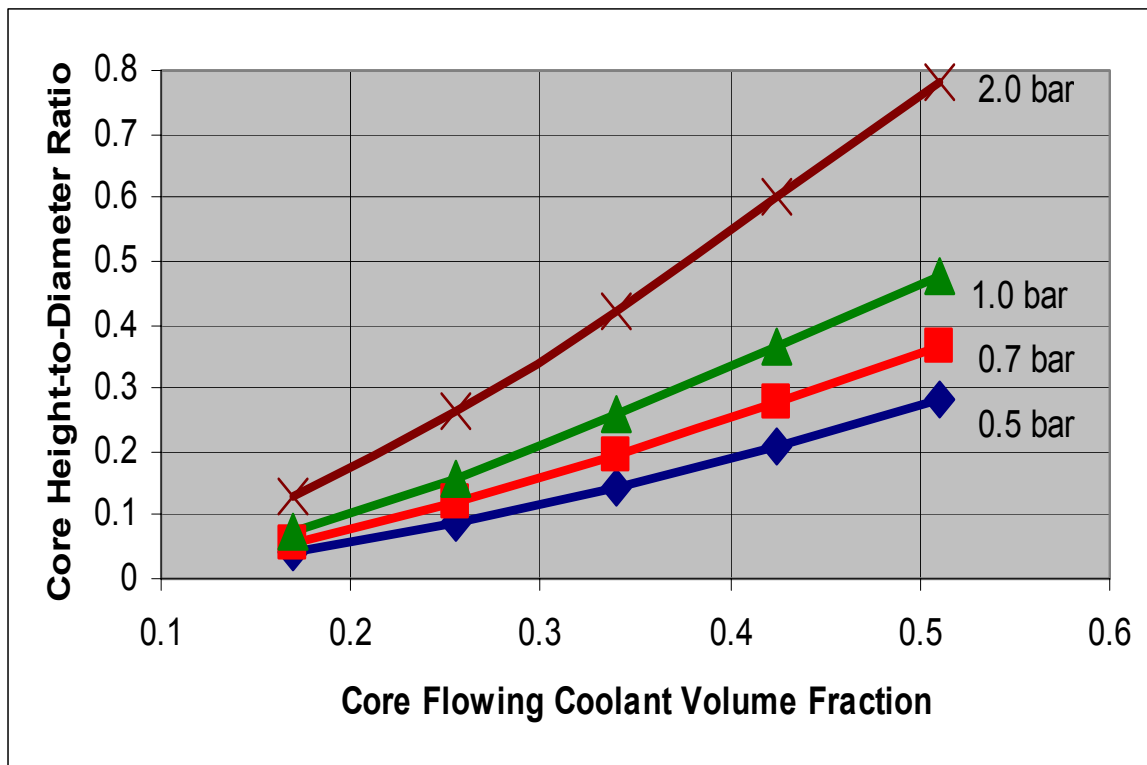


Figure 4.20. 2400 MWt Core Pressure Drop.

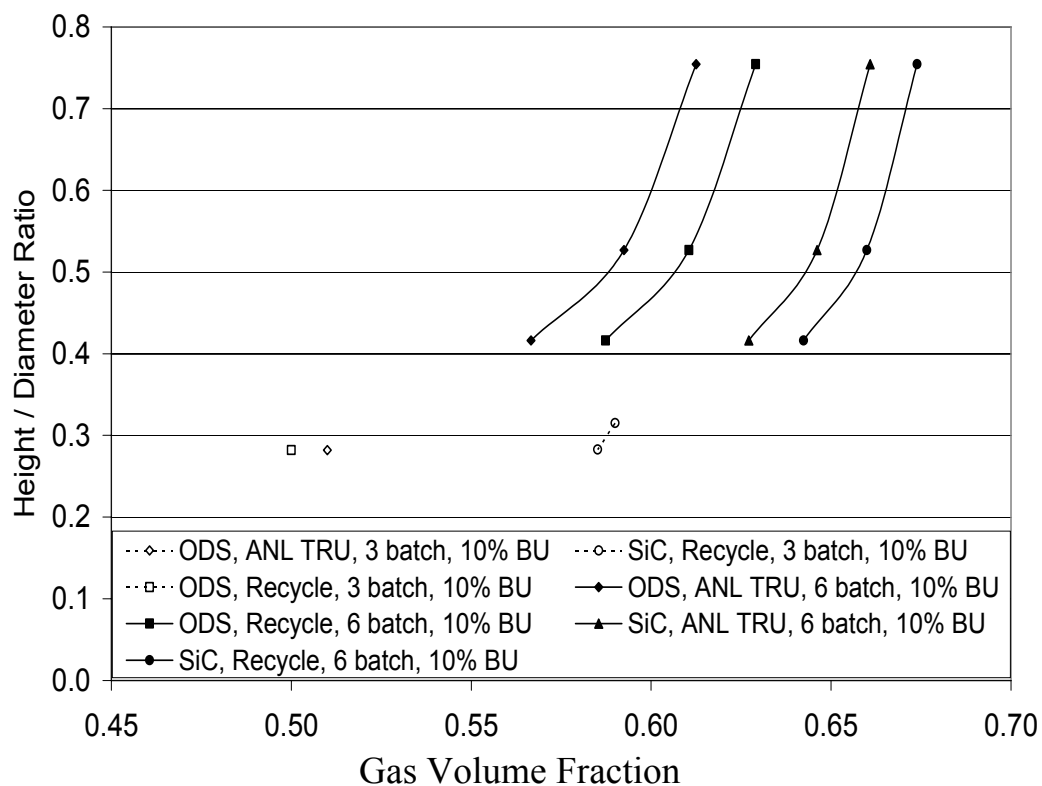


Figure 4.21. TRU breakeven curves for 2400 MWt, 10% burnup, 100 W/cc (fuel).

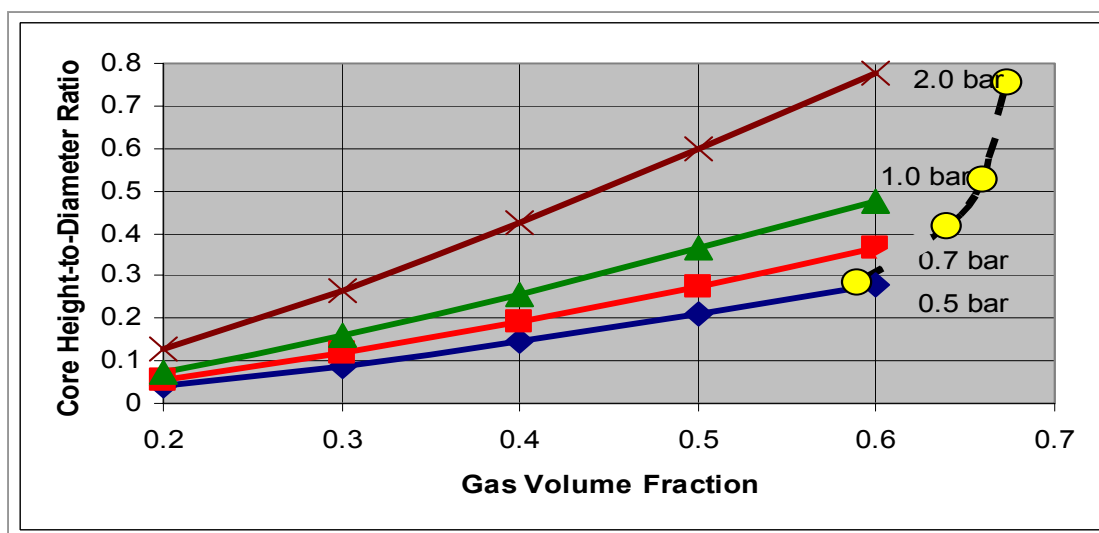


Figure 4.22. 2400 MWt Fuel Assembly Pressure Drop.



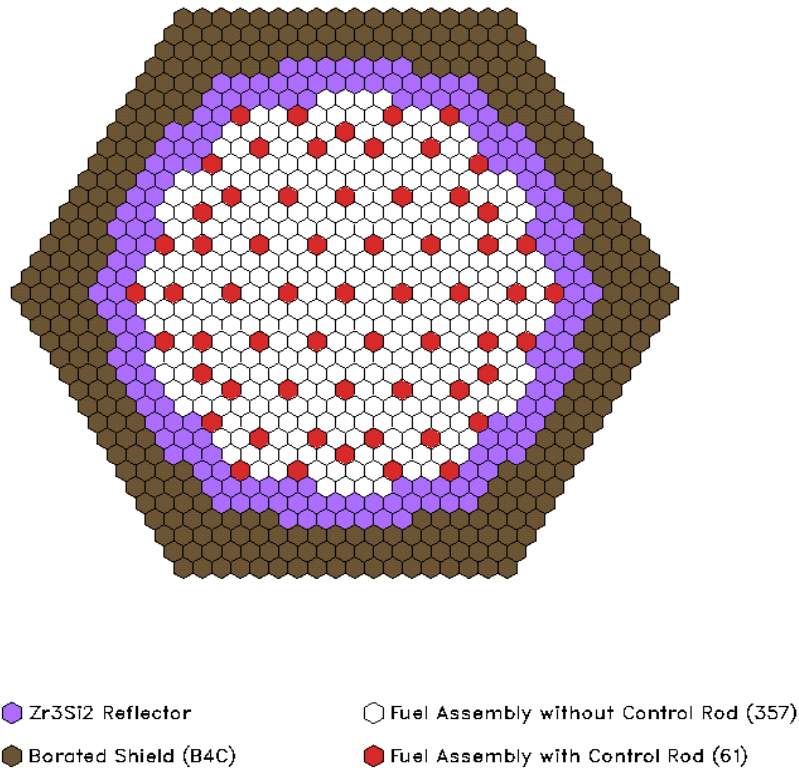
#### 4.2.4 Current Core Design

Table 4.3 shows the current design parameters for a 2400 MWt, 100 W/cc core with a core height-to-diameter ratio of 0.282 and flowing coolant fraction of 50.15. The 50.15 value is the result of the assumption that 85% of the core cross-section is to be available for the pin-bundle and 59% of the pin-bundle cross-sectional area was assumed to be coolant. The power and power density together constrain the core volume to be  $24 \text{ m}^3$ . This volume, and the core height-to-diameter ratio, causes the core height and equivalent diameter to be 1.34 m and 4.67 m, respectively, and 13 grid spacers were used. The equivalent diameter determined the core cross-sectional area, where 50.15% of this is  $8.95 \text{ m}^2$ . The linear power was determined so that the core pressure drop was 0.5 bars, (50,000 Pa). However, this solution produced a peak clad temperature of  $1127^\circ \text{C}$ . Therefore, a second solution for the same core height and diameter combination was obtained in which the peak clad temperature was constrained to be  $1100^\circ \text{C}$ . This produced a core pressure drop of 0.5208 bars and required 111019 fuel pins. The total cross-sectional area can be thought of as being divided into 111019 hexagonal cells. Figure 23 shows the core layout that was produced. There are 357 standard subassemblies that have 271 fuel pins each, and 61 control subassemblies that have 234 fuel pins each, for a total of 111,021 pins. The control subassemblies are equivalent to the standard subassemblies, except for the central 37 pins, which have been replaced by a hexagonal control rod thimble where a round control rod could be inserted. The area of the thimble itself, and the area enclosed by it, is considered to be gas.

Table 4.3. Distribution of Gas within the Core.

Location	% of Entire Core Cross Section
Coolant Within Pin Bundles	50.8
Coolant In Gaps Between Assemblies	6.2
Gas Inside Fuel Pins	6.5
Coolant Inside Control Rod Thimbles	1.7
Total Gas Fraction	65.2

The hexagonal duct of both subassembly types is the same. The flat-to-flat outer dimension of the duct was first sized to provide the same area as 271 hexagonal pin cells. The two duct thickness of 3.7 mm each was added, and the result rounded up to the nearest mm to obtain an outer dimension of 215 mm. The pin-bundle area inside the control subassembly is assumed to be 234/271 times that of the standard subassembly. The as-designed flowing coolant area in the 418 subassemblies, 357 standard ones plus 61 control ones, was calculated and found to  $9.06 \text{ m}^2$  instead of the  $8.95 \text{ m}^2$  originally assumed. The distribution of structure, gas, and fuel is the same as in the calculated case. However, the 65.2% that is gas has been slightly redistributed so that as shown in Table 3, 50.8 % rather than 50.15% is used to cool the pin bundles in the 418 subassemblies.



\*111,021 Pins in 418 Subassemblies

Figure 4.23. Layout of 2400 MWt Pin Core\*.

A new analytical case was also solved in which the area of flowing coolant was increased from 8.95 m<sup>2</sup> to 9.06 m<sup>2</sup>. This case had a pin-bundle pressure drop of 0.5042 bar and a peak clad temperature of 1105.5° C instead of the required 1100° C. The required temperature could be achieved by increasing the number of fuel pins, which would increase the pressure drop slightly. It was decided to not make these adjustments, and to accept the slightly higher peak clad temperature. To do otherwise would require that 15 or 16, 271-pin subassemblies be added to accommodate 4138 additional fuel pins. Table 4.4 shows the two designs. The column labeled “starting” represents the design with the 8.95 m<sup>2</sup> coolant flow area, and the column labeled “ending” shows the effects of increasing the coolant flow area to 9.06 m<sup>2</sup>. The former has a pin-bundle pressure drop of 0.5208 bar and a peak clad temperature of 1100° C and the latter has a pin-bundle pressure drop of 0.5042 bar and a peak clad temperature of 1105.5° C.

For this particular design, Table 4.5 shows details of the neutronic fuel cycle calculation as well as safety reactivity coefficients. Additional results are also shown for parametric variations on core height-to-diameter ratio and fuel composition. The column heading Pu2016 refers to the recycle plutonium fuel anticipated to be available in France in the year 2016.

Finally, very preliminary fuel pin clad performance results are presented in Figure 4.24 for the design parameters tabulated in Table 4.6.

Table 4.4. Database for Starting and Reference (Ending) Core Designs.

<b>2400 MWt PIN CORE</b>	<b><u>STARTING</u></b>	<b><u>ENDING</u></b>
(U,Pu)C		
<b>T-H Parameters</b>		
reactor power, MWt	2400	
core power density, MW/m <sup>3</sup>	100	
core inlet temperature, C	480	
core outlet temperature, C	850	
system pressure, MPa	7	
core ΔP, bar	0.52	0.50
peak clad temperature, C	1100	1105
spacer pressure drop, Pa	33400	32500
friction pressure drop, Pa	16800	16100
acceleration pressure drop, Pa		
inlet pressure drop, Pa	1090	1060
outlet pressure drop, Pa	810	769
<b>Core Geometry</b>		
active core volume, m <sup>3</sup>	24	
core length-to-diameter ratio	0.282	
active core diameter (equivalent), m	4.77	
hex-to-hex active core diam. along diagonal, m	5.106	
radial reflector thickness, m	0.4	
radial shield thickness, m		
lower axial reflector length, m	1	
active core length, m	1.34	
upper axial reflector length, m	1	
number of core subassemblies (control subs. exclu.)	357	
area fractions (structure, gas, fuel), %	13, 65, 22	
number of control assemblies	61	
area fraction (control subassemblies), %	15	
total core flow area, m <sup>2</sup>	<b>8.95</b>	<b>9.06</b>
<b>Fuel Assembly Geometry</b>		
flat-to-flat of hexagonal duct (outside), mm	215	
duct wall thickness, mm	3.7	
interassembly gap, mm	7	
number of pins per core subassembly	271	
number of rings (excluding center one)	9	
number of spacers	13	
hydraulic diameter, mm	12.2	
pin pitch (average), mm	12.6	
<b>Fuel Pin Geometry</b>		
total pin length, m	3.34	
fuel pellet diameter, mm	6.73	
fuel clad thickness, mm	0.4	
fuel pin diameter, mm	8.45	

Table 4.5. 2400 MWt Core Neutronic (SiC Clad) Performance Data at 10% Burnup.

TRU Feed		ANL TRU	Recycled TRU	Pu2016	Pu2016	ANL TRU	Recycled TRU	Pu2016
H/D		0.315	0.315	0.315	0.315	0.282	0.282	0.282
Core Power Density		100.00	100.00	100.00	100.00	100.00	100.00	100.00
Fuel Power Density		118.15	118.15	118.15	118.15	116.67	116.67	116.67
Fuel Pellet Diameter		5.92	5.78	5.77	5.71	6.02	5.87	5.87
Cycle Length		790	752	749	367	828	786	785
Batches		3	3	3	6	3	3	3
Fuel Volume Fraction		0.26	0.25	0.25	0.24	0.27	0.26	0.26
Structure/Matrix Volume Fraction		0.14	0.14	0.14	0.14	0.14	0.14	0.14
Coolant Volume Fraction		0.58	0.59	0.60	0.60	0.57	0.59	0.59
BOC HM Loading (kg)		56,684	54,034	53,754	52,225	59,417	56,396	56,352
EOC HM Loading (kg)		54,729	52,171	51,901	51,317	57,367	54,451	54,410
Charge TRU Enrichment (%)		16.8	16.5	16.3	16.3	16.8	16.5	16.2
BOC TRU Inventory (kg)		9,847	9,245	9,052	8,869	10,314	9,625	9,472
EOC TRU Inventory (kg)		9,846	9,245	9,053	8,870	10,310	9,625	9,472
Burnup Reactivity Loss (%dk)		1.0	1.6	2.6	1.3	1.0	1.4	2.6
$\beta$	BOC						0.00355	0.00370
	EOC						0.00350	0.00359
Prompt Neutron Lifetime	BOC						1.0E-06	1.0E-06
	EOC						9.4E-07	9.6E-07
Depressurized Reactivity (\$)	BOC						1.33	1.20
	EOC						1.39	1.32
DTC (pcm/K)	BOC						-0.68	-0.72
	EOC						-0.61	-0.63
Axial Expansion Coefficient (\$/cm)	BOC						-0.077	-0.073
	EOC						-0.076	-0.074
Radial Expansion Coefficient (\$/cm)	BOC						-0.523	-0.50
	EOC						-0.531	-0.52

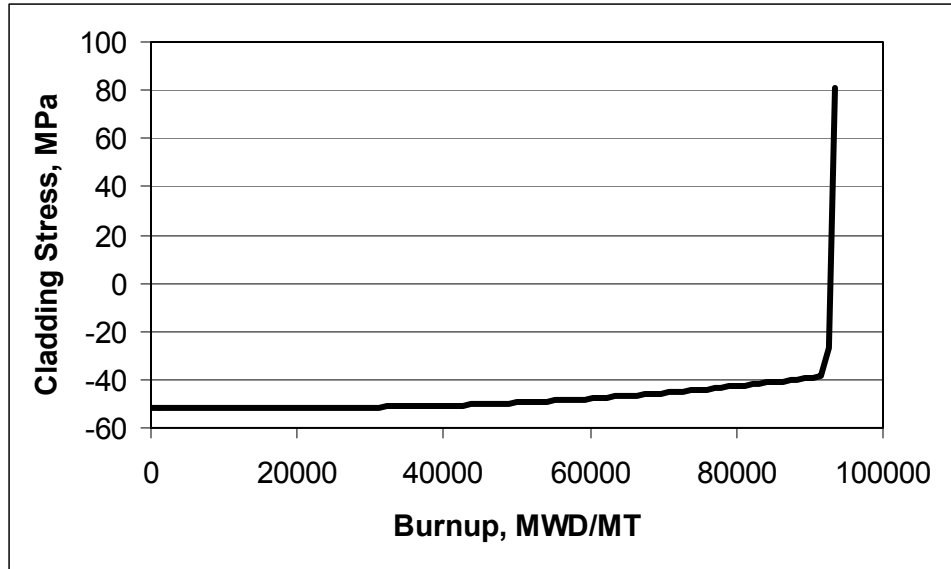


Figure 4.24. Fuel Pin Clad Performance.

Table 4.6. Fuel Pin Design Parameters.

Parameter	Value
Fuel	(U-15Pu)C
Cladding OD	8.45 mm
Cladding wall thickness <sup>1</sup>	0.4 mm
Pellet diameter	6.73 mm
Pellet density <sup>2</sup>	97%
Active core height	1.34 m
Plenum height	1.0 m
Core inlet/outlet temperature	480/850°C
Plenum temperature used for calculation	665°C
Average burnup	10 at. %
Pin fill gas pressure	5 atm
Core pressure	7 MPa
Fuel centerline temperature	1275°C (E. Feldman)
Fractional fission gas release at EOL	37%

1. A more realistic value for SiC/SiCf would be 1-1.2 mm, due to manufacturing constraints.
2. Pellet density of 97% may not be realistic due to manufacturing and fuel performance issues.

## **5. GFR Materials for Moderate to High Temperature Use**

### **5.1 CO<sub>2</sub> Radiolysis Experiments**

The following work was performed during FY04 on a supercritical CO<sub>2</sub> (S-CO<sub>2</sub>) radiolysis loop:

- An initial isometric CAD layout of the physical footprint of the loop for the laboratory setting was completed.
- In order to determine the actual performance for the system pump for the purpose of system modeling, a pump test was performed; an initial design was completed for the system's non-regenerative heat exchanger; and a more comprehensive thermal model of the out of pile S-CO<sub>2</sub> loop was developed in MATLAB in order to study a variety of different operating parameters and resulting conditions.
- The initial design of the overall loop for both the ex and in-reactor loops was completed; the detailed design of the ex-reactor loop and the identification of key challenges to the construction of the loop were completed; a detailed design of the autoclave that will be used was completed; and an analysis of the required modifications for the MIT radiolysis model, originally designed for aqueous radiolysis modeling, to allow modeling of supercritical CO<sub>2</sub> was completed.

This task was completed, and an interim report on the CO<sub>2</sub> radiolysis was issued on 3/24/2004, which outlines the progress on design and construction of the CO<sub>2</sub> loops. Due to funding constraints, this task was not continued.

### **5.2 ODS Joining**

ODS alloys have been joined with Transient Liquid Phase (TLP) bonding, diffusion bonding, and Pressure Forge Welding (PFW). The TLP bonding process for MA956 is almost optimized, while the PFW was successfully developed for joining fine-grained PM2000 in a fuel rod end cap configuration. Significant progress has been made with TLP bonding PM2000 and creep testing of bulk PM2000. Characterization of PM2000 TLP bonds and comparison with the earlier MA956 results is underway.

An interim report on ODS joining studies was issued on 3/24/2004, which outlines in more detail the progress to date on joining of MA956 and PM2000.

#### **5.2.1 Transient Liquid Phase Bonding**

TLP bonding has been used to successfully joint Inconel MA956 in the longitudinal direction. Bonds show minimal recrystallization and the bond-line is barely distinguishable from the bulk, as seen in Figure 5.1. Use of a very short bonding time and a multistage post-bond heat treatment (PBHT) is required to achieve high quality bonds. Initial bonds of PM2000 fine grained material with very short bonding times followed by PBHT resulted in a recrystallized grain growth across the bondline (Figure 5.2). Longitudinal bonds generally have much more desirable microstructures than transverse bonds, as can be seen in Figures 5.1 and 5.3, respectively. Work is ongoing to develop bonding procedures that produce consistent results with bulk material that is of variable quality.

Creep tests were performed on bulk PM2000 to provide a baseline for future comparison with bonded specimens. PM2000 fine grain material (as-received) was heat treated at 1385 °C for 4 hours to create coarse-grained, recrystallized material. The creep testing results are shown in Table 5.1. The size of the PM2000 creep samples is on the order of the grain size after heat treatment, and so the creep specimens may be tricrystals, bicrystals, or, in extreme cases, single crystals rather than true polycrystals. Hence, to create a consistent dataset, it is suggested that specimens of larger diameter be used. However, the need to bond in the longitudinal orientation with respect to the working direction limits the present specimen dimensions.

The recrystallization behavior of the batch of PM 2000 received from Plansee is highly inconsistent, with the frequent presence of localized, equiaxed, relatively fine grain regions being a severe problem. These inconsistencies hinder establishment of processing - microstructure relationships for the TLP bonds. Work is currently underway to characterize the as-received material to determine if this problem is unique to one portion of the PM 2000 stock or is a more generalized issue.

Table 5.1. Creep rupture test results of PM2000 after PBHT 4 h, 1385 °C.

<b>Thermal Exposure Prior to Creep Testing (<i>i.e.</i> equivalent of PBHT thermal cycle)</b>		<b>Creep Rupture Life</b>		
Temp. (°C)	Time (h)	Temp. (°C)	Stress (MPa)	Life (h)
1385	4	1000	13	> 185
			50	> 500
			85	~ 0

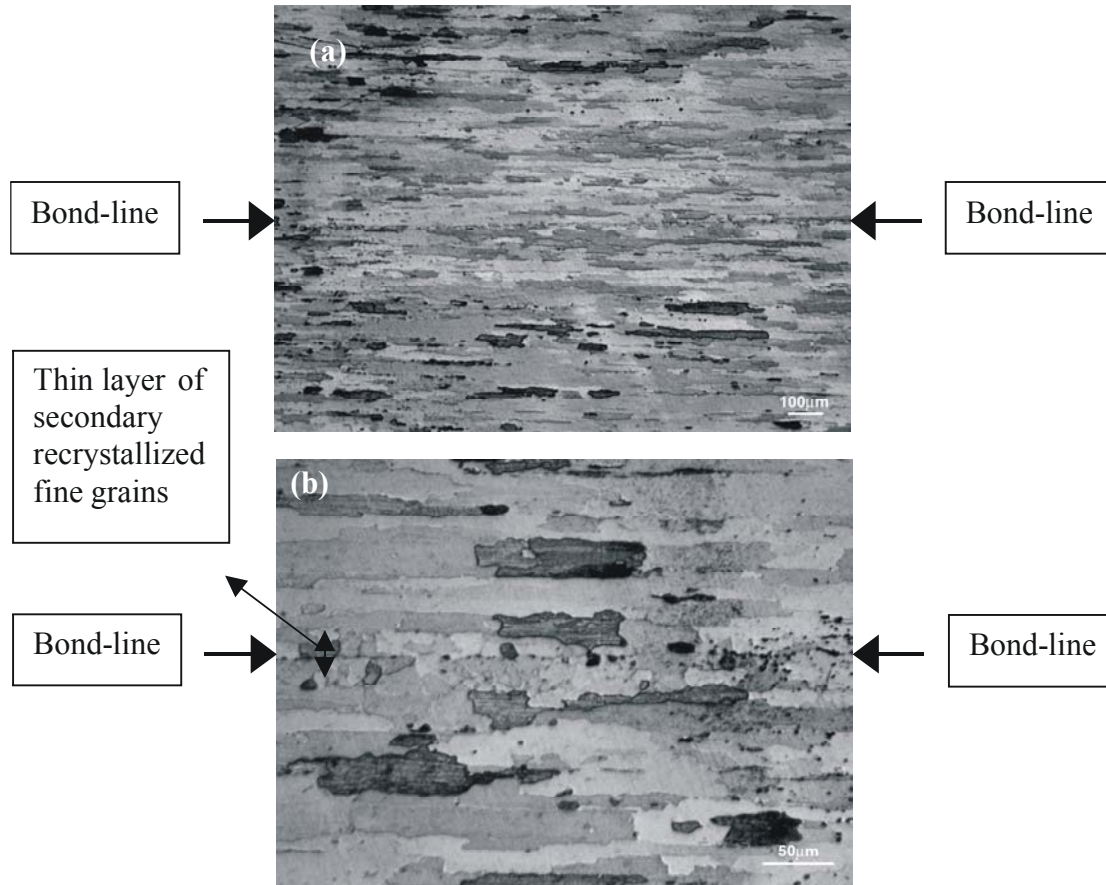


Figure 5.1. MA956 fine grain bond bonded using 1  $\mu\text{m}$  boron interlayer 120 seconds, 1250  $^{\circ}\text{C}$  (PBHT 1 hour, 1300  $^{\circ}\text{C}$ ). (a) bond-line (b) thin layer of recrystallized grains at the bondline.

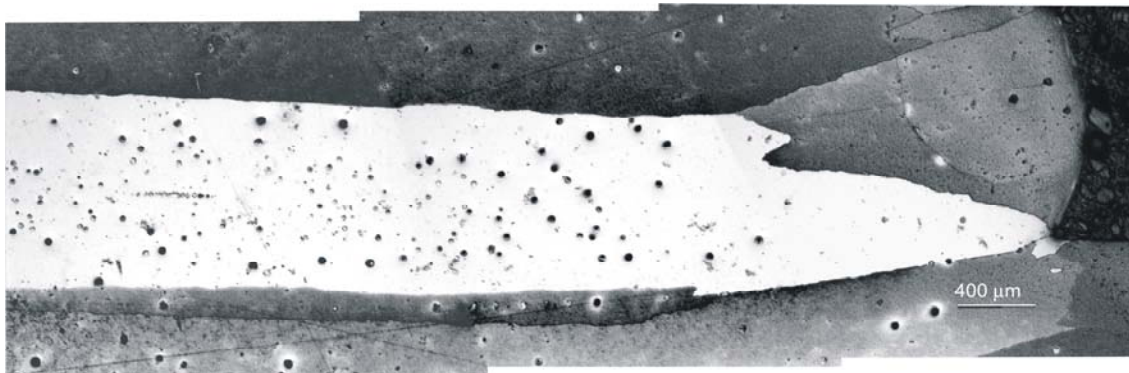


Figure 5.2. PM2000 fine grain A orientation bond 250 nm boron 30 seconds, 1250  $^{\circ}\text{C}$  (PBHT 2hour, 1385  $^{\circ}\text{C}$ ). Large recrystallized grain (bright) across the bond-line is observed.



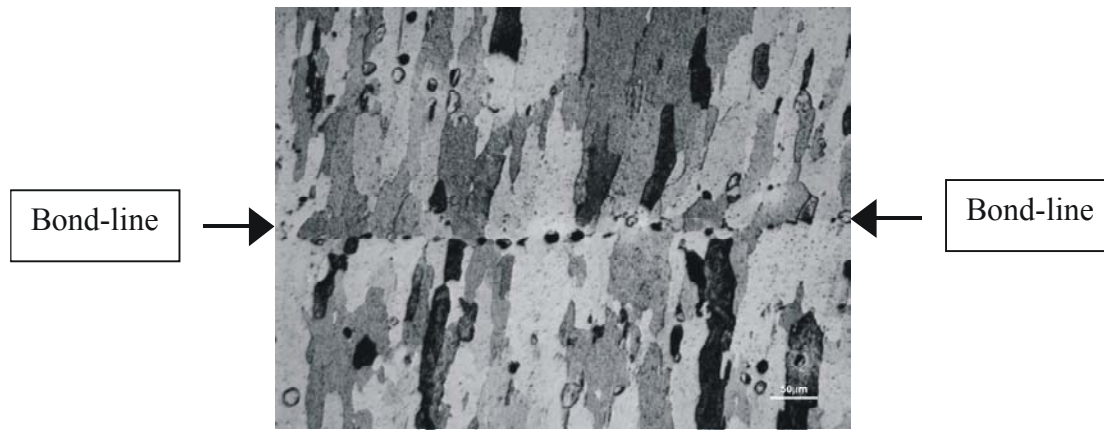


Figure 5.3. MA956 fine grain transverse orientation with respect to working direction with 1  $\mu\text{m}$  boron interlayer 256 seconds, 1250  $^{\circ}\text{C}$  (PBHT 1 hour, 1250  $^{\circ}\text{C}$  + 1 hour, 1300  $^{\circ}\text{C}$ ).

### 5.2.2 Diffusion Bonding

Successful (at least based on microstructure) diffusion bonds for the ODS materials have been produced at unusually low stresses. The mechanisms allowing this are under investigation. Diffusion bonding has been performed on MA956 material in both fine grain and coarse grain conditions. Bonds were formed when joining fine grain to fine grain substrates (Figure 5.4) and fine grain to coarse grain substrates (Figure 5.5). Occasional voids were observed in the diffusion bonds. However, bonding did not occur when bonding coarse grain to coarse grain substrates. Bonds using substrates with longitudinal orientation (parallel to working direction) had an almost invisible bond-line.

Completion of a significant portion of the ODS joining test matrix (Figure 5.6) has shown that the effect of bond-line orientation on bond quality is a key variable in eliminating, or at least minimizing, the formation of undesired fine grains. To some extent, the formation of fine grains was observed for all orientations investigated. However, as can be seen from Table 5.2, the extent of uncontrolled recrystallization varied considerably with the orientation of the substrates. As shown in Figure 5.7, the best results to date have been obtained with bonding in the longitudinal substrate – longitudinal substrate configuration, with the bond-line parallel to the working direction (orientation “A” in Figure 5.6).

Table 5.2. Effect of bondline orientation on the extent of uncontrolled recrystallization in the vicinity of the bondline for MA956.

<b>Bond Geometry as shown in Figure 5.6</b>	<b>Extent of Uncontrolled Recrystallization Leading to Fine Grained Regions at or Near Bond-Line</b>
A	Usually minor and does not extend significantly into substrates.
	Some samples had isolated recrystallized regions up to ~ 50 $\mu\text{m}$ wide.
B	No data (bonding studies moved to PM 2000).
C	Extensive and continues up to ~ 100 $\mu\text{m}$ into longitudinal substrate.
D	30 – 50 $\mu\text{m}$ wide and does not extend significantly into substrates

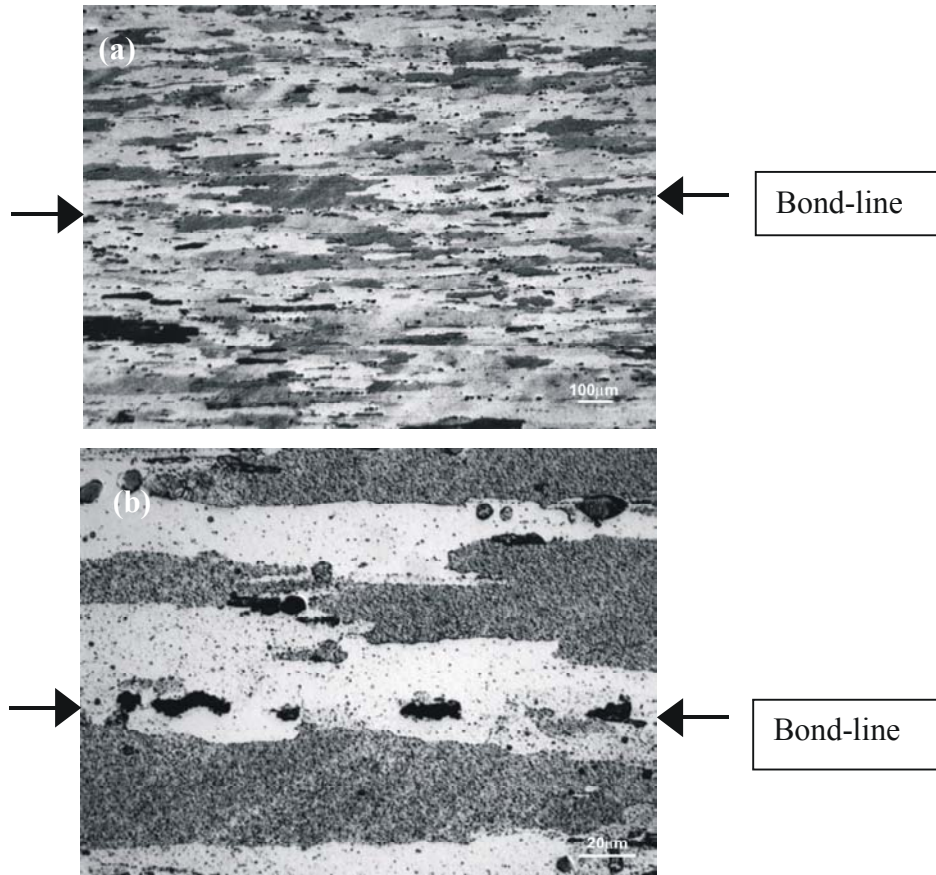


Figure 5.4. Diffusion bond of MA956 fine grain longitudinal orientation with respect to working direction at 1250°C under a 1 – 5 MPa applied stress (PBHT 1 h, 1300 °C): (a) bond-line (b) grain growth across the bond-line with occasional voids.



Figure 5.5. As-bonded diffusion bond of coarse to fine MA956 in longitudinal orientation showing continuous bond-line without any secondary recrystallization and agglomeration (1–5 MPa).

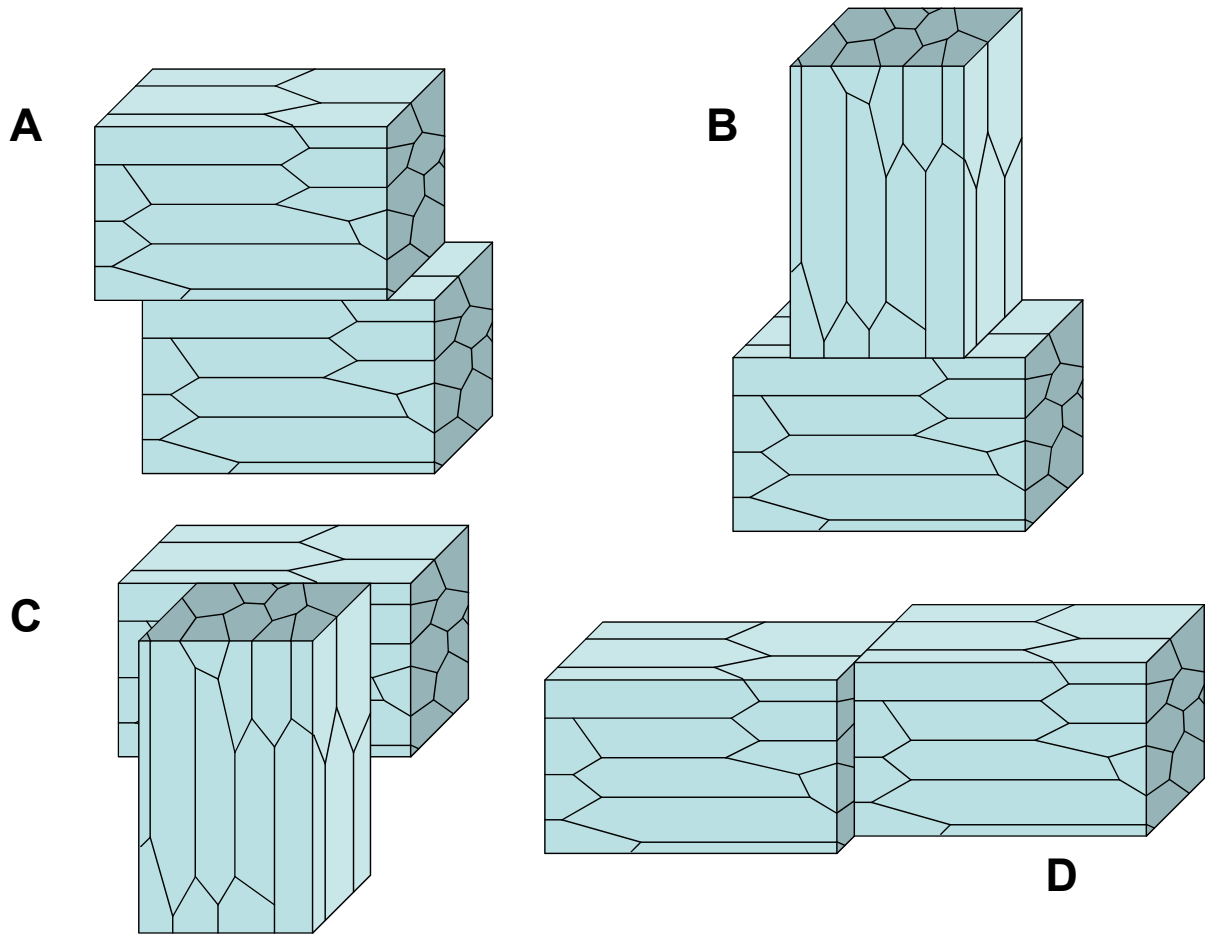


Figure 5.6. Bond geometries investigated (note the laps shown are for illustration purposes and butt joints have been employed in work to date):

- A. Longitudinal substrate bonded to a parallel longitudinal substrate, with the bond-line parallel to the working direction;
- B. Longitudinal substrate bonded to a perpendicular longitudinal substrate, with a mixed bond-line orientation;
- C. Longitudinal substrate bonded to a transverse substrate, with a mixed bond-line orientation;
- D. Longitudinal substrate bonded to a parallel longitudinal substrate, with the bond-line perpendicular to the working direction.

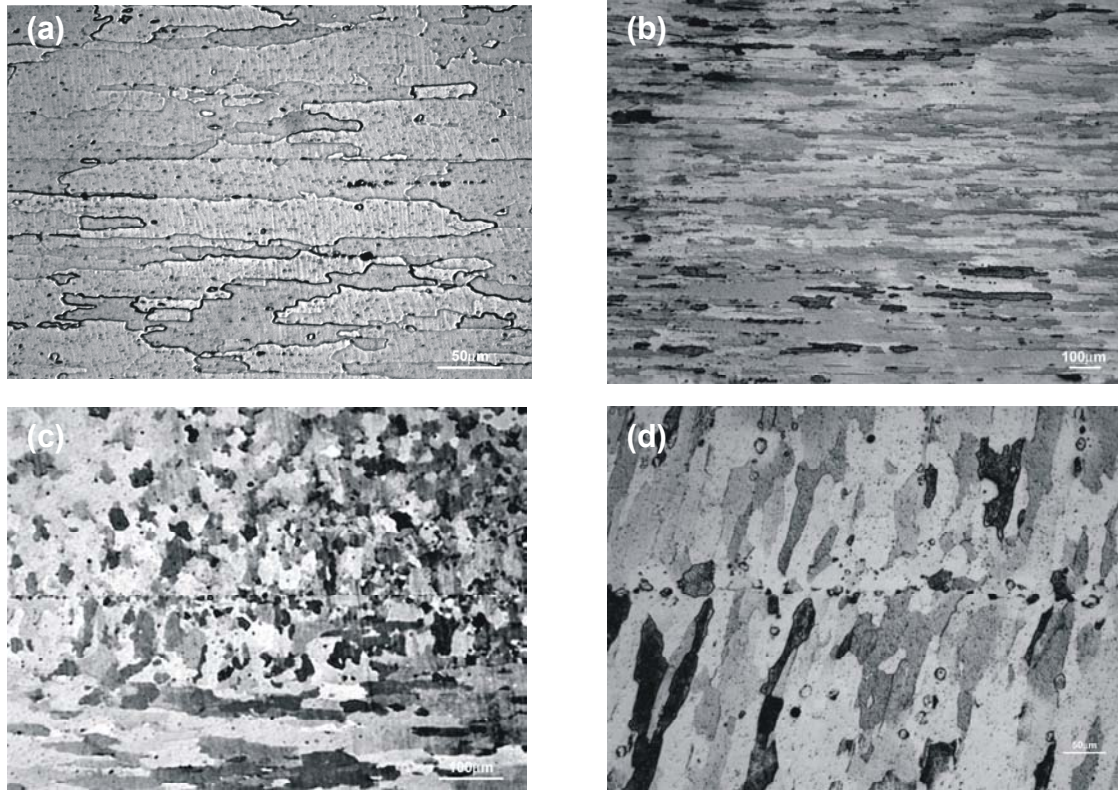


Figure 5.7. MA 956 fine grain, 1  $\mu\text{m}$  boron interlayer: (a) 'A' orientation bond 1 hour at  $\sim 1250$   $^{\circ}\text{C}$  ( PBHT 8 hours at  $1300$   $^{\circ}\text{C}$  ) (b) 'A' Orientation bond 120 seconds,  $1250$   $^{\circ}\text{C}$  (PBHT 1 hour,  $300$   $^{\circ}\text{C}$ ). (c) 'C' Orientation bond 300 seconds at  $\sim 1250^{\circ}\text{C}$  (PBHT 8 hours at  $1300$   $^{\circ}\text{C}$ ) (d) 'D' Orientation bond  $1250$   $^{\circ}\text{C}$ , 256 seconds bond (PBHT  $1250$   $^{\circ}\text{C}$  1hr + $1300$   $^{\circ}\text{C}$  1hr).

## 5.2.3 Pressure Forge Welding

### 5.2.3.1 Background

Solid state joining processes require the disruption of surface oxides and other contamination, and also typically require high temperatures to promote interdiffusion or grain growth across the boundary, to produce a monolithic structure without melting, which would destroy the unique advantages of mechanically alloyed materials. Diffusion welding and transient liquid phase bonding meet this requirement with little plastic deformation by achieving close contact at high temperatures for relatively long periods (time scale: many minutes or hours), and paying close attention to the relevant thermally activated phenomena. The flash welding method developed at ANL-W and further refined in Japan meets this requirement because, although it involves melting and vaporization at the interface (required to disrupt surface contamination), the rapid expulsion of vaporized or melted material as the parts are quickly assembled (time scale: milliseconds) leaves a joint composed essentially of unmelted material in which the dispersed oxides are undisturbed.

The approach taken in the present work, resistance pressure welding (or resistance forge welding) meets this requirement by also using high temperatures, but in addition causing intense



plastic deformation at the interface (time scale: seconds to tens of seconds), which both disrupts surface contamination and provides a driving force for dynamic recrystallization across the interface.

### 5.2.3.2 Specimen Design

Specimen design has evolved over the course of the project, beginning with a simple tapered design in inexpensive conventional stainless steel materials. Design changes were made iteratively based on successive results. The end cap design shown in Figure 5.8 is the latest design as of September 2004; it provides a 2 mm land slightly larger in diameter than the ID of the simulated tubing (machined from PM2000 material), and a tapered section to expand the tube on insertion.

The restraining ring, also made from PM2000, serves to provide the backing force for plastic deformation at the interface. The 3-4 mm wide notch in the ring provides a location for the control thermocouple to attach at the weld zone, and also facilitates the removal of the ring for further specimen testing. The ID of the ring was machined to match the computed OD of the tubing after expansion by the inserted end cap. This proved to provide insufficient restraint, so later welds were made with 0.008 in. shim stock between ring and tube.

Optimized welds made with this configuration are repeatable both in appearance and in measured parameters, and failed in tension in the tubing, away from the weld area.

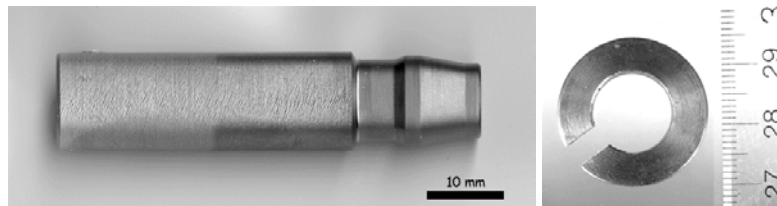


Figure 5.8. Insert specimen and restraining ring for Resistance Pressure Welding, PM2000 material.

### 5.2.3.3 Parameter Development

The thermomechanical cycle finally developed for this phase of the joining effort involves the steps shown in Figure 5.9.

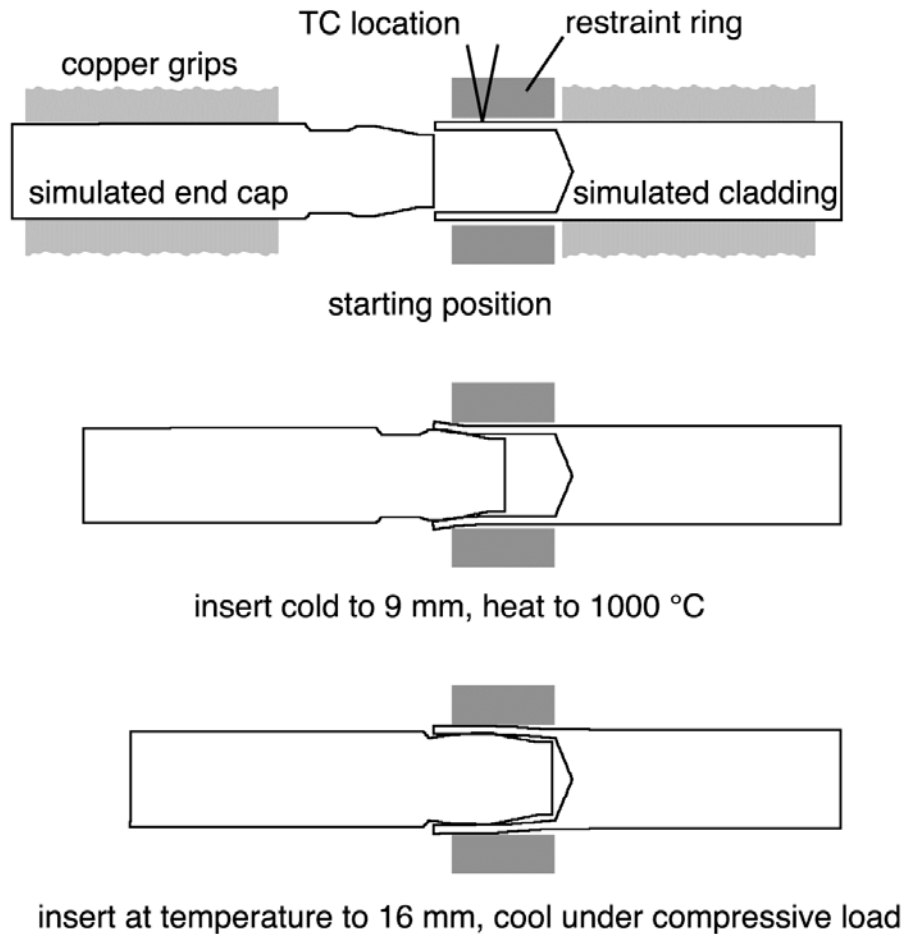


Figure 5.9. Welding technique for PM2000 material developed in current work.

#### 5.2.3.4 Weld Cross-Sections

The effects of specimen design and welding parameters were initially characterized by metallographic cross sections to measure the bonded area and examine the plastic flow phenomena. Figure 5.10 shows such a cross section optically, and Figure 5.11 shows the upper weld on this specimen on the SEM. The short cycle times at 900 to 1000 °C were not expected to cause the growth of the very large grains typical of these alloys (and desirable for high-temperature service); the existing fine grain structure was not resolved with the etching techniques used.

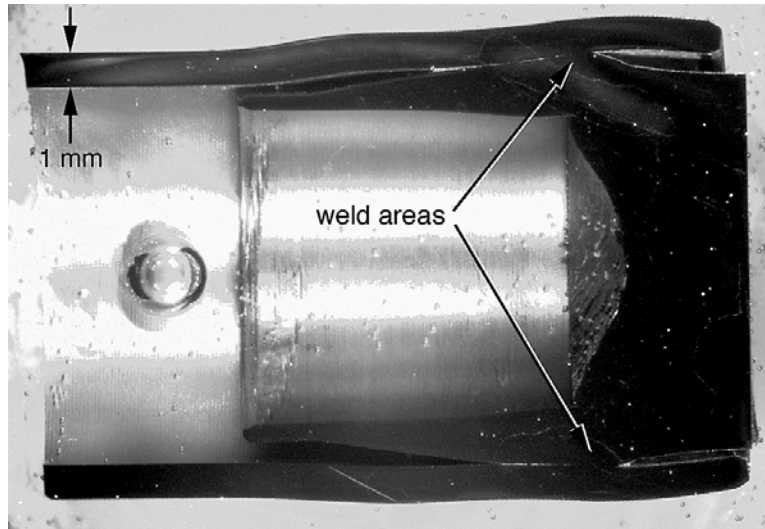


Figure 5.10. Cross section of typical weld.

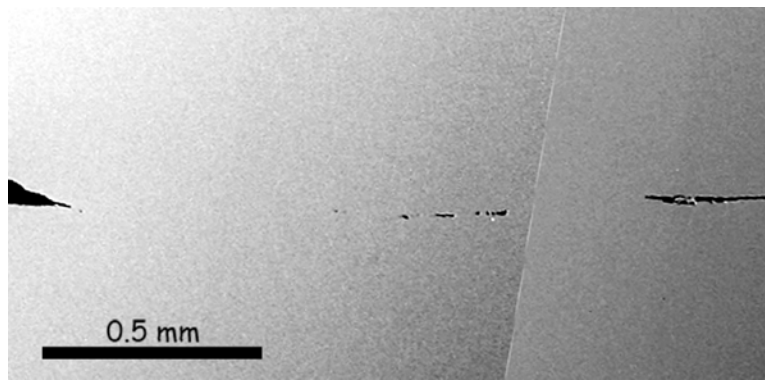


Figure 5.11. SEM view of unetched weld in PM2000 fine-grained material. Examination at higher magnification indicated full bonding in apparent bonded areas.

### 5.2.3.5 Tensile Test Results

In the later stages of parameter development, once consistent welds were achieved as judged by the metallographic cross sections, tensile tests were performed. After welding, the restraining ring was slid off, pins were inserted in holes at the distal ends of the joined parts (for positive gripping by the Gleeble's unthreaded clamping copper blocks), and they were returned to the Gleeble for mechanical testing.

The basic service criterion for this joint was taken to be an axial load due to internal pressurization of the fuel cladding by gaseous fission products, at transient temperatures up to 900 °C. The internal area of the tube is 0.139 in<sup>2</sup> and the wall thickness is 1 mm (0.0394 in.), yielding an annular area of 0.0570 in<sup>2</sup>. The loads and stresses in Table 5.3 would apply:



Table 5.3. Load and Pressure Relationships

<u>Internal pressure, psi</u>	<u>Axial load</u> Pounds	<u>Axial stress in wall</u> ksi
1000	139	2446
2000	279	4893
5000	697	12,232
10,000	1394	24,464

Near the end of the process development cycle thus far, a nominal insertion distance of 15 mm was used. These welds failed in tension at the weld interface at loads corresponding to fairly high internal pressures, but in an effort to increase weld strength, insertion distance was increased to 16 mm. These welds failed outside the weld joints, at loads indicated in Table 5.4, and the broken specimens are shown in Figures 5.12 and 5.13.

Table 5.4. Tensile Test Results for Welds

<u>Insertion distance</u> mm	<u>Test temperature</u> °C	<u>Axial load</u> pounds	<u>Cladding wall stress</u> Ksi	<u>Corresponding internal pressure</u> psi
15	20	2236	39.2	16,000
15	900	1190	20.9	8540
16	20	7942	139.4	57,000
16	900	1193	20.9	8560

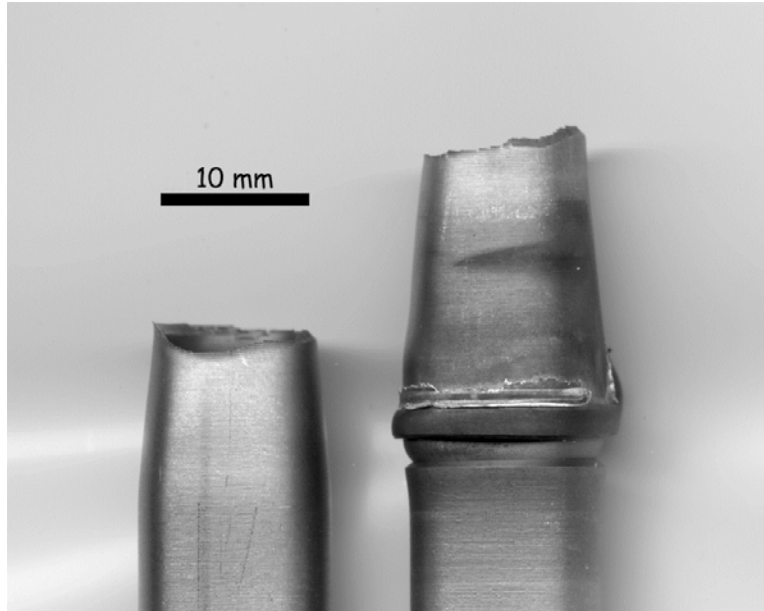


Figure 5.12. Pressure forge weld in PM2000 material, tensile tested at room temperature, failure away from weld at load of 7,942 pounds.

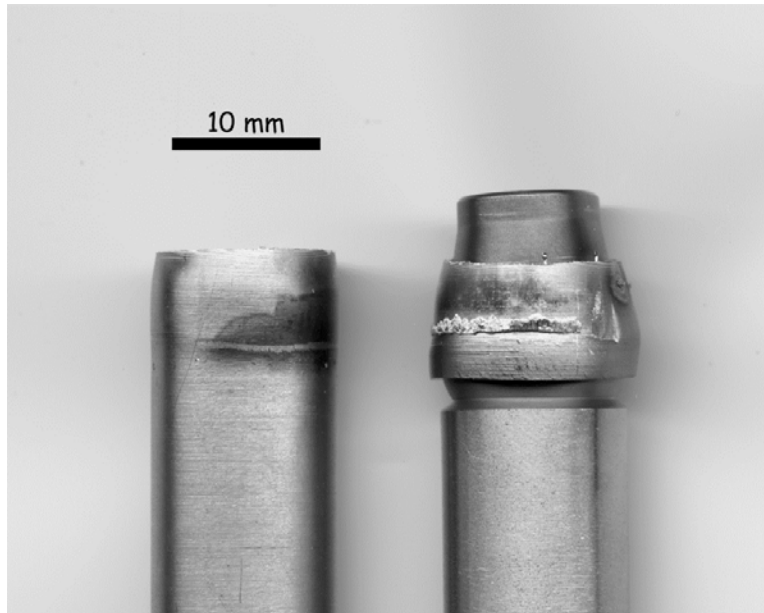


Figure 5.13. Pressure forge weld in PM2000 material, tensile tested at 900 °C, failure away from weld at load of 1,193 pounds.

### 5.2.3.6 Further Work

The Gleeble used for this work is a general-purpose thermomechanical testing machine, and the grips and setup for this series of welds were improvised. An axial motion was used for convenience because that is the loading mode of the present Gleeble configuration. Rigidity, alignment, and control were adequate to the task, but it should be noted that in a production environment, a more specialized machine would be developed, designed for the job. For example, the restraint ring would probably be replaced by a mechanically operated fixture.

Perhaps a more logical geometry for this joint would be the application of both torsional and axial loads. There would be several advantages to this method: with many rotations available, many linear mm of travel would be possible with each weld, leading to more complete surface oxide removal at lower axial loads and hence with less massive machinery; suitably restrained, the cladding wall itself can bear the axial loads; and maintaining a smooth OD and a neat outside finish on the joint, which were not attempted in the present work, should be easily done.

A torsion unit (capable of simultaneous torsional and axial loading) for the INEEL Gleeble is on order and expected to be delivered and installed early in CY 2005. It may be useful to use some of the remaining ODS material in a joint redesigned for this kind of loading.

Further examination of the tensile tested welds, including possible heat treatment to produce large grains, is under way.

## 6. GFR High Temperature Fuels

### 6.1 Screening and Down-Selection of GFR Fuel Concepts

Based on Generation IV goals and the GFR fuel attributes derived from them, a simple set of criteria with a common basis among all fuels was selected for initial screening of fuel types; these criteria are listed in Table 6.1. More comprehensive requirements were developed for specific fuel types based on the results of core neutronic and thermohydraulic studies.

Table 6.1 GFR initial fuel screening criteria.

Screening Criteria	Reference Value used for Screening
Melting temperature	> 2000°C
Fuel heavy metal density	> 5 g/cm <sup>3</sup>
Fuel burnup potential	> 5% HM

The fuel temperature requirement, derived from the goal to exclude melting under unprotected loss of flow conditions is the most limiting in terms of fuel selection, and when coupled with core neutronic requirements, severely limits the range of possible fuels. Obviously, current fuels such as zirconium-clad LWR fuel and stainless steel clad fast reactor fuels are excluded on the basis of cladding melting temperature. TRISO coated particle fuel is excluded on the basis of low heavy metal density. Burnup potential of fuels is somewhat more difficult to gauge, but does not appear to be overly restrictive.

Two categories of fuel have the highest potential for success; carbide and nitride-based composite-type (dispersion) fuels and pin-type refractory ceramic fuel. Many variants of pin-type fuels have been extensively developed, and offer a large database on which to base estimates of fuel performance (although there are still sizable gaps). This fuel type offers perhaps the shortest path to development, but currently has limitations in high temperature performance due to the lack of a suitable refractory cladding material. Breakthroughs in cladding development, such as the successful development of SiC composite cladding material may make this fuel type acceptable for GFR use. Pin-type fuel based on ODS steels (Oxide Dispersion Strengthened) may be used for a GFR demonstration core startup. Duplex-type cladding materials, consisting of a SiC fiber composite shell encasing an alloy cladding tube may also be possible, and would likely meet the criteria of ‘no core restructuring’ while still allowing seal welds to be made by more-or-less conventional fusion welding technology.

Dispersion fuels (also referred to as composite fuels) offer the potential to reach goal burnup and offer a larger range of flexibility in the choice of materials. These fuels consist of a distribution of discrete fuel particles embedded in a refractory matrix. The concept most likely to be successful for composite fuel will use thinly coated particles (or elongated elliptical ‘rods’) embedded in an inert matrix. In the ideal case, the matrix remains largely unaffected by neutron, fission fragment, and  $\alpha$ -particle damage from the fission events that take place in the fuel particles. Although this fuel type appears best suited to withstand the high temperatures possible in GFR unprotected loss-of-coolant accidents, it has limitations in terms of heavy metal density.

In addition, initial screening identified particle bed assemblies as a potential fuel type meeting GFR goals, although the resolution of certain technical issues remains uncertain. This fuel type has been selected as the front-runner for the current Japanese GFR concept.

Two fuel types, pin-type fuels and dispersion fuels, were thus selected for further study. Also considered to a lesser degree were particle bed fuels. Assessments on the feasibility of these fuels were made for on the basis of available data and modeling.

## ***6.2 Pin-Type Fuel***

### **6.2.1 Overview and Requirements**

Pin type fuel is attractive due to the large operating database accumulated for similar fast reactor fuels and cladding materials. The high outlet temperature of the GFR and the requirement for exclusion of core restructuring as a result of clad melting, however, eliminates all steel-based alloys, including ODS (Oxide Dispersion Strengthened) steels, from consideration.

Fuel response to the core conditions following a loss-of-coolant event is the overriding factor in the design of pin-type fuels. A gas plenum must be built into the fuel to accommodate gas release. During normal reactor operation at 70 bar coolant pressure, fuel can be designed such that the net stress on the cladding is compressive; the coolant pressure is larger than the pin internal pressure. The plenum length is then a compromise between internal gas pressure that can be tolerated during core depressurization and shutdown and the coolant pressure drop through the core during operation.

During an unprotected LOCA, however, core coolant pressure decreases coincident with both core and fuel temperature increases. This increase in fuel temperature causes increased fuel pin internal pressure due to both ‘ideal gas’ pressurization and an increased gas release rate from the fuel. This increase in pin internal pressure, coupled with the lack of external pressure causes a large increase in cladding tensile hoop stress. This increase in cladding tensile hoop stress occurs coincident with a decrease in cladding creep resistance and strength due to the cladding temperature increase. This combination of events during unprotected LOCA, coupled with core design constraints driven by plenum height restrictions make conventional sealed pin design for GFR fuel difficult.

Alternatives to sealed fuel pin designs that alleviate the above problem due to pressure and temperature excursions during LOCA include a common plenum in the low temperature region of the core, fuel pins containing rupture disks that allow pin depressurization to the coolant prior to ballooning, or vented fuel pins.

Specific requirements for pin-type fuel are, in general, similar to those defined for liquid metal-cooled fast reactors and are listed in Table 6.2, except that the required cladding melting temperature is much higher.

Table 6.2 Pin-type Fuel Requirements

Requirement	Reference Value
Maximum Diametral Swelling	<2%
Peak Dose	> 80 dpa
Melting Temperature	>2000°C

### 6.2.2 Fissile Phase Considerations

Two primary factors are involved in the selection of the fissile phase for pin-type fuel; these are core neutronic and fuel performance. Core neutronics calculations performed as a result of the U.S./French INERI program indicate that oxide fuel is a poor performer from the perspective of core neutronics relative to carbide and nitride fuels due to low heavy metal density and spectral softening due to the presences of oxygen. Excluding oxide fuel, the primary choices of fissile phase become mixed carbide and nitride fuels. Both fuels have been demonstrated to perform well to burnups on the order of 8-12% HM in sodium cooled fast reactor systems. These systems operate at lower cladding temperatures but higher power densities relative to current GFR requirements.

There are no outstanding considerations related to fuel behavior that separate carbide and nitride fuels. Scoping fuel performance analyses do not differentiate these fuels at a generic level. At lower burnup, mixed nitride fuel swelling and gas release tends to be lower than that of carbide fuel. As burnup increases, however, these differences in gas release and swelling behavior decrease. Considerably more fuel performance data is available for mixed carbide fuels, including swelling and gas release correlations, although much of the data is for fuels with high oxygen content, which tend to exhibit higher swelling. Data is also available for carbide sphere-pac fuel.

Another consideration is the need for  $^{15}\text{N}$  enrichment and recycle for nitride fuel for reasons of neutron economy in the GFR system. The presence of  $^{14}\text{N}$  strongly affects core breeding performance. The order of magnitude to which this additional expense affects fuel cycle cost are a source of significant uncertainty that favor the use of carbide fuel.

It is likely that the overriding factor in fissile phase (pellet) selection for a pin-type concept will be driven by cladding compatibility, a fuel performance consideration.

### 6.2.3 Cladding Selection

The goal to prevent core restructuring coupled with core neutronic requirements limits the potential choice of cladding materials. Alloy base-metals and metalloids that meet the 2000°C melting temperature requirement are B, C, Nb, Mo, Ru, Hf, Ta, W, Re, Os, and Ir. It is obvious that B and Hf are not practical materials for this application due to their effect on core neutron economy and that Ru, Os, and Ir are not practical due to cost and availability. Scoping core neutronics studies have also shown that cores clad with Ta, W, and Mo require very large heavy metal inventories to allow self breeding. Carbon and carbon/carbon composites have a service life of less than 15 dpa [7], compared to the  $\sim 80$  dpa required during the service life of fuel at 5 % burnup, and are also excluded.

The remaining allowable alloy base metal, Nb, was developed in alloy form as Nb-1Zr and PWC-11 (Nb-1Zr-0.06C) during the SP-100 space reactor program. Many fuel irradiation experiments have been conducted using variants of Nb-Zr cladding and UN fuel to burnups of approximately 6% in fast spectrum environments. [8] A thin rhenium cladding inner liner was found to be important for limiting fuel-cladding-chemical-interaction. Neutronic performance of Nb-1Zr clad fuel encased in Nb-1Zr ducts is marginal, but improves when SiC is used as the duct material. [9] Concerns related to the use of Nb-based alloys are performance in case of air ingress associated with high core temperatures during a LOCA and sensitivity to coolant impurities. In the case of air ingress at high temperature, the cladding would be heavily oxidized and may lose structural integrity and allow fuel movement. Careful control would also have to be exercised over reactor coolant impurity content

SiC is another potential cladding choice, although at a much earlier stage of development. Joining of SiC to SiC or other materials is a major issue confronting development of SiC cladding. A method for cladding development that appears promising is the NITE (Nano Infiltration Transient Eutectic) process developed in Japan at Kyoto University, although little detailed information has been published in the open literature in the English language. Work on joining SiC has also been conducted as a part of this program.

Other potential processes include CVI (Chemical Vapor Infiltration) of a fiber preform woven over a monolithic SiC tube being conducted under a DOE SBIR (Small Business Innovative Research) grant by Gamma Engineering. [10] A SiC reinforced ferritic steel cladding is also under development [11]. The best near-term approach may be the hybrid approach, where a metallic liner is used to ensure a hermetic seal and ease pin closure issues.

SiC cladding is most compatible with mixed carbide fuel. Reaction of SiC with UN is thermodynamically favorable above 550°C, although reaction could presumably be prevented

through the use of a cladding liner. SiC composites have demonstrated good irradiation behavior [12] and should be capable of maintaining mechanical properties at dose levels well beyond 50 dpa at temperatures of less than 1000°C.

#### **6.2.4 Reference and Alternate Concepts**

Significant unknowns confronting the development of SiC cladding and the integral performance of SiC clad mixed carbide fuel must be weighed against the more developed but less suitable Nb-1Zr clad nitride fuel. Nb-1Zr has the additional difficulties of requiring tight control of coolant impurity level, particularly oxygen and hydrogen; SiC is more robust in this regard. (U,Pu)N fuel, most compatible with Nb-1Zr cladding, requires enrichment in  $^{15}\text{N}$ , which represents a significant unknown in terms of fuel cycle cost. In view of these tradeoffs and the relatively unknown state of technology, neither technology offers a definite advantage.

SiC clad (U,Pu)C fuel is selected as the reference for pin-type fuel, however, in light of the potential of this fuel system in meeting Gen IV goals. SiC offers improved core neutronic performance over Nb alloys and expected robust behavior in the case of air ingress into the core during accident events. In addition, this fuel combination has the advantage of not requiring the production and recycle of enriched nitrogen.

### **6.3 Particle Bed Fuel**

#### **6.3.1 Overview**

Coated particle fuels (CPF) configured as a particle bed or as a fluidized bed have been considered primarily for nuclear propulsion applications in the past, [13, 14, 15] but have also received cursory consideration for use as a reactor system for minor actinide burning [16]. The primary advantages in using such a system are the low thermal gradients across each fuel unit (particle) and a high heat transfer area, resulting in low thermal stresses within fuel particles and the ability to resist fuel damage during transients. The primary issues with such a system are related to practical matters in fuel element design, particularly the design of a reliable frit material to keep fuel particles from exiting the reactor and preventing the possibility of frit clogging under conditions in which fuel particles generate aerosols or small fragments due to failure. Pressure drop across assemblies also tends to be higher than for fuel designs with discrete channels, although this can be offset by using thin beds, within the constraints imposed by heavy metal loading requirements in the core.

#### **6.3.2 Fuel Design**

Detailed fuel design studies have not been conducted in the U.S. The Japanese have adopted a particle bed core as the reference for the GFR under their ongoing ‘feasibility study’. The Japanese core consists of horizontal flow assemblies, as depicted in Figure 4.1 (b) [17]. Particles consist of a TiN porous buffer and seal coat of TiN over large diameter (U,Pu)N particles. The frit material is a SiC composite, as are the other structural components. Similar particle bed designs have been studied by the French CEA [18]. An alternate design (Figure 4.1(c)), consisting of a bed of particles embedded in a solid SiC matrix is also considered; this is equivalent to a ceramic matrix dispersion fuel.

Significant concerns regarding this concept relate to fuel particle integrity, performance, and retention in the subassembly. The failure behavior of ceramics is controlled by the presence of

microstructural defects introduced primarily during fabrication; failure is induced by stress concentrations around these defects leading to crack growth. A net compressive stress field does not lead to crack propagation, thus ceramics are considerably stronger in compression than tension. The SiC ‘pressure vessel’ layer in TRISO particle designs relies on irradiation-induced shrinkage of the inner and outer pyrocarbon layers in order to maintain a net compressive stress in the coating until late in its service life. The absence of the two pyrocarbon coating layers allows a net tensile stress in the coating as a result of fission gas pressurization throughout the life of the particle, and will almost certainly lead to a much less robust fuel. Because strength in ceramics is flaw controlled, statistical data from materials produced by prototypic fuel particle fabrication methods is required in order to estimate particle failure probability. This concern is offset to some degree by embedding the particles in a solid matrix, where manipulation of the relative thermal expansion coefficients can lead to a net compressive stress in the particle coating during operation.

A second concern that has not been addressed for particle bed concepts is the affect of particle-to-particle movement on fuel behavior. The particle bed is similar in design to vibratory mills, which provide effective means of reducing particle size in the ceramic industry, thus care must be taken to avoid the possibility of excessive particle motion within the bed during reactor operation. Finally, the effect of interparticle sintering or fusion on subassembly flow and particle failure must be addressed. Given these concerns, the particle bed assembly, although attractive from a core neutronics point of view, offers greater uncertainties and obstacles to development than either of the other two concepts considered.

### 6.3.3 Reference Concept

No distinct U.S. reference is suggested for the particle bed fuel concept. Given the early state of development of this concept, both the CEA or Japanese designs are considered equivalent.

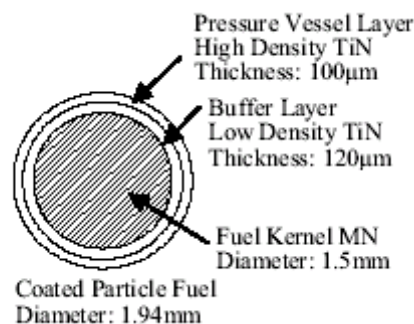


Figure 6.1 (a). Japanese coated particle concept for particle bed GFR.



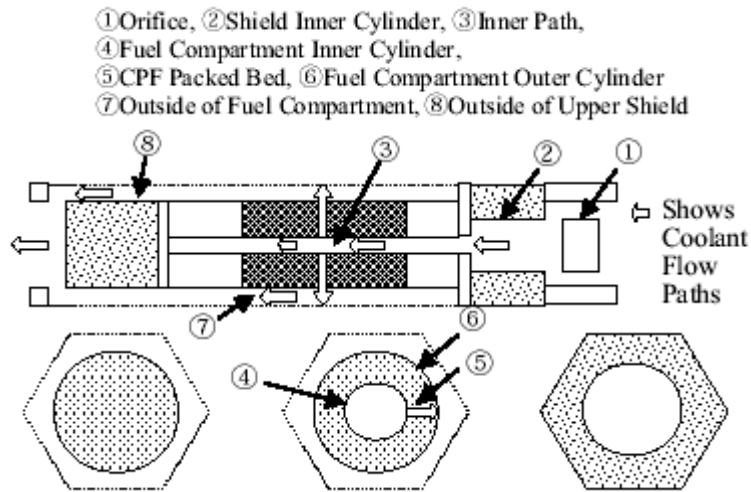


Figure 6.1(b). Japanese horizontal flow particle bed subassembly.

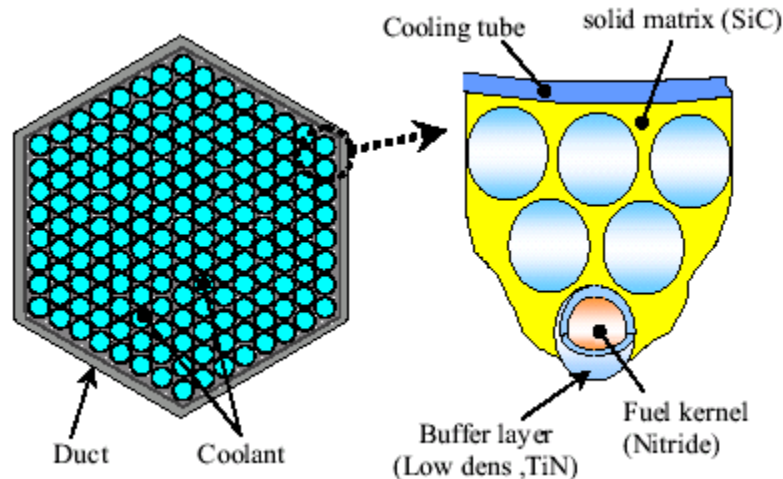


Figure 6.1 (c). Japanese 'solid matrix' coated particle fuel subassembly design.

## 6.4 Dispersion Fuel

### 6.4.1 Overview

Dispersion fuels (also referred to as composite fuels) offer the potential to reach goal burnup and offer more flexibility in choice of materials than pin-type concepts. These fuels consist of a distribution of discrete fuel particles embedded in a non-fuel matrix.

Composite fuel performance depends heavily on the microstructural characteristics of the fuel. Two primary strategies have been pursued for optimizing fuel behavior through manipulation of microstructural variables. Macrodispersions attempt to maintain the thermal conductivity and

structural integrity of the matrix during irradiation through the use of relatively large and widely distributed fissile phase particles. Microdispersions incorporate a fine dispersion of the fissile phase into a neutronically inert matrix. This is often done as a convenience for fabrication. In the case of a microdispersion, fission related damage occurs over a larger fraction of the matrix volume relative to a macrodispersion, introducing the possibility for fission fragment driven matrix swelling. Macrodispersions are thus preferred for the composite-type fuel currently envisioned for the GFR. In the ideal case, the matrix remains largely unaffected by neutron, fission fragment, and  $\alpha$ -particle damage from the fission events that take place in the fuel particles. The concept most likely to be successful for composite fuel will use thinly coated particles (or elongated elliptical ‘rods’) embedded in an inert matrix.

#### **6.4.2 Dispersion Fuel Particle Concepts**

Two types of fuel particle designs have been considered for GFR dispersion fuels. These are particles fabricated with and without a buffer layer.

The simplest dispersion fuel concept, and the one with the highest potential fuel loading, consists simply of a (non-buffered) fuel particle embedded in an inert matrix. This particle may incorporate a thin barrier coating to prevent fuel/matrix chemical interaction from occurring during fabrication and irradiation. Such particles typically include a distribution of approximately 15% open porosity to act as a fission gas ‘plenum’ reducing the gas-driven pressure on the matrix. Dispersions using this concept have been proven to work well in combination with ductile matrices such as steel [<sup>19</sup>] and niobium [<sup>20</sup>]. Figure 6.2 (a) shows a schematic drawing of this fuel type. Figure 6.2 (b) shows, as an example, a dispersion of oxide fuel in a stainless steel matrix. This combination of ductile matrix and unbuffered fuel particle has been proven to be quite robust in numerous irradiation tests, although performance has been empirically postulated to be limited by a combination of fission density and temperature. Fuel fission density is linked both to fuel particle loading and burnup. Figure 6.2 (c) shows a plot of irradiation data for plate-type dispersion fuels circa. 1963 [<sup>21</sup>]. Fuels lying to the left of the line are postulated to be stable; those to the right, unstable during irradiation. Note that the ‘stability line’ will likely be shifted further to the right for dispersion fuel configurations such as blocks and plates, due to a more favorable distribution of stress in these cases.

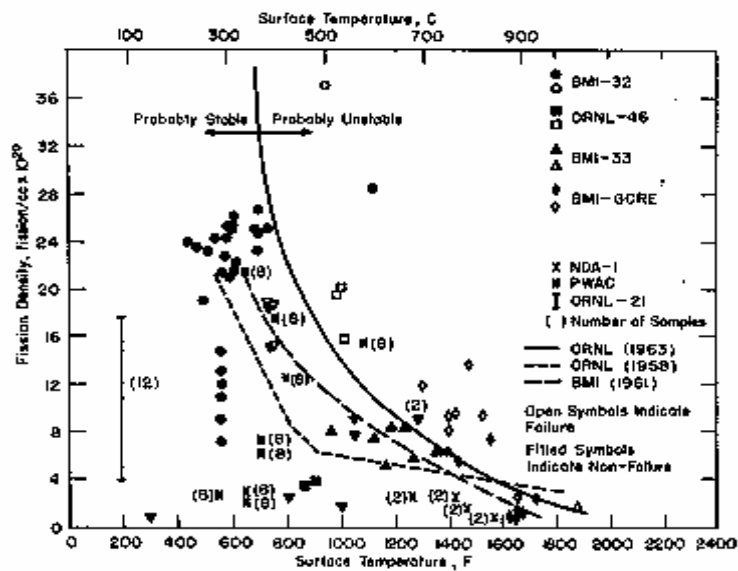
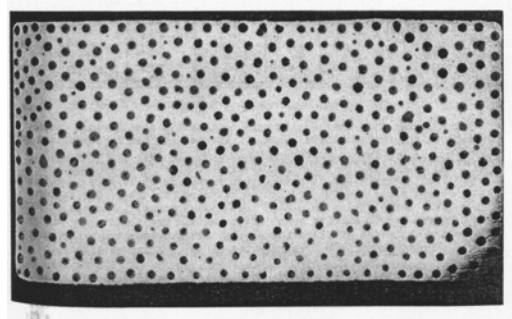
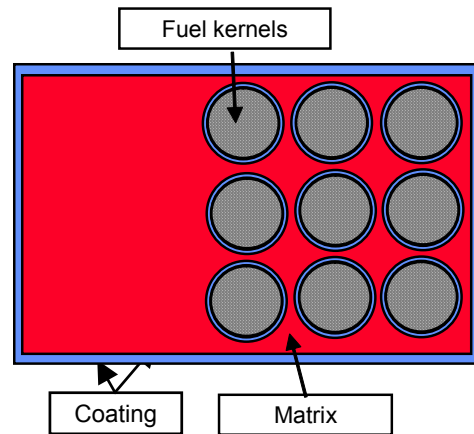


Figure 6.2. (a) Schematic on 'unbuffered' dispersion fuel. (b) Example of dispersion of  $\text{UO}_2$  in stainless steel. (c) Plot of fission density vs. surface temperature showing empirical regimes of stability for  $\text{UO}_2$  dispersions in stainless steel.

The above concept works well when used with ductile matrix materials, however experiments with unbuffered particles in ceramic matrices produce less favorable results. Several irradiation tests have been conducted using oxide-based cermet fuel concepts in France [22, 23] and Japan [24]. Matrix cracking has been observed in all of these cases, leading to higher than expected fission gas release. This behavior has been attributed to stresses imposed on the matrix both from fuel particle swelling and the differences in thermal expansion coefficient between the fuel particles and the matrix. Also examined in the THERMHET irradiation test in France was the so-called ‘jingle’ variant of the macrodispersed concept, which incorporates free space between the fuel particle and matrix. This concept shows promise in reducing matrix fracture due to fuel/matrix mechanical interaction, although some matrix cracking was still observed. [25]

Figure 6.3 (a) shows the results of a finite element calculation of the maximum principal stress induced by thermal expansion mismatch in a composite consisting of UC particles dispersed and bonded to a SiC matrix; here the stress free temperature is 25 °C. It can be seen that at 1000°C, a maximum principal stress >360 MPa occurs due to thermal expansion mismatch alone. This stress level will be unacceptable for ceramic materials, which do not readily deform and relax these stresses. (In reality, the stress free temperature will be approximately the fabrication temperature, resulting in a somewhat different stress distribution in the matrix).

Given the available cermet irradiation behavior database, the concept most likely to minimize fission gas release to the coolant will incorporate ‘buffered’ particles in a dense matrix. This concept is shown in Figure 6.3(b). Here each particle is surrounded by a low density layer of material with low crush strength. This ‘buffer’ material serves the dual role of providing volume for fission gas and providing volume for fuel particle swelling. The buffer layer is protected by a dense layer, also designed to provide for fission product retention. In this way, there are three barriers to fission product release to the coolant. These are the coating around the particle, the dense matrix, and the cladding around the fuel block.

The use of coated particles makes it more difficult to achieve high heavy metal density in the fuel. Since fuel particle volume increases in proportion to the cube of the particle radius, the net heavy metal density within a fuel particle falls rapidly with increasing coating thickness. This fact requires that the coating thickness to kernel diameter ratio be kept as small as possible while maintaining utility as a fission product barrier. Shown in Figure 6.3 (c) is a plot of matrix stress in a free particle due to fission gas release plotted over the ratio of coating thickness to kernel diameter for a fixed buffer layer thickness at 10% burnup. The buffer layer thickness was chosen to accommodate 15 volume percent fuel particle swelling. This plot is, of course, the result of specific assumptions about the fission gas release rate from the fuel kernel. From the plot, it can be seen that below a ratio of 0.1 at 1473 K, the stress in the coating outer shell increases rapidly with decreasing coating thickness. The coating thickness to kernel diameter ratio should thus be maintained at about 0.1. In order to eliminate local stresses due to differential thermal expansion, the thermal expansion coefficients of the fuel particle coating and the matrix should be matched.

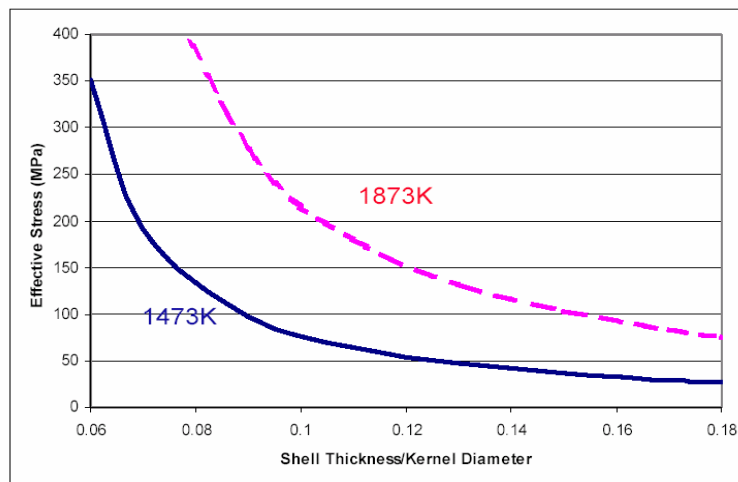
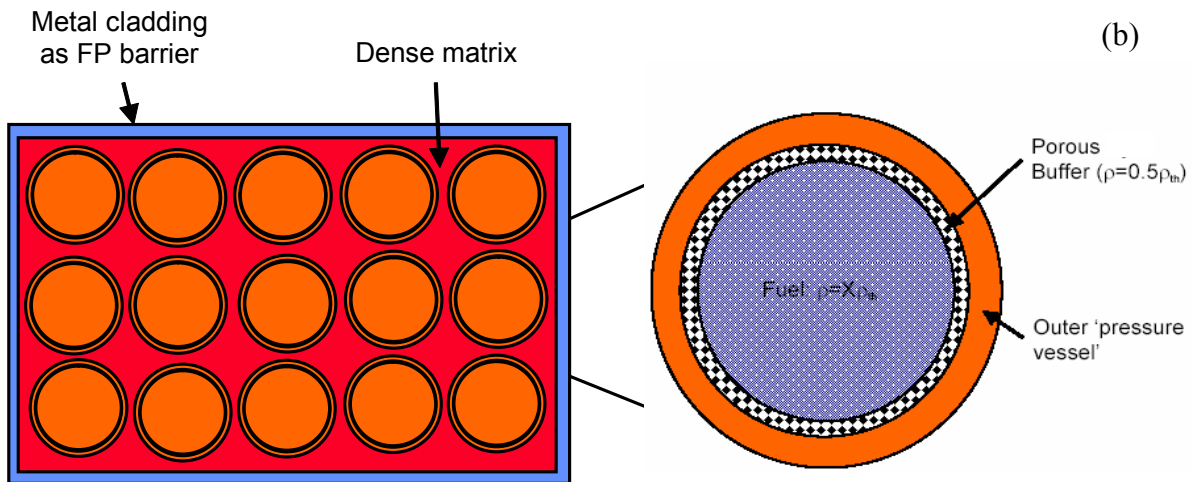
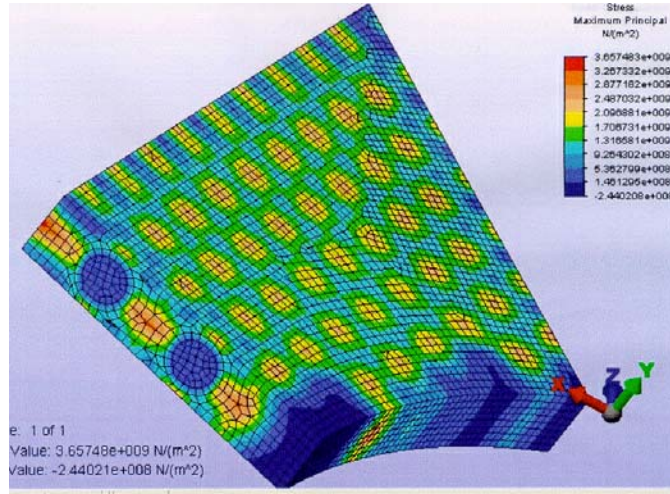


Figure 6.3. (a) FEA calculation of stress to the differential thermal expansion in a UC particle, SiC matrix dispersion. (b) 'Buffered' particle concept. (c) Plot of the effective stress in a coating due to fission gas pressure as a function of the shell thickness to kernel diameter ratio. Particle diameter 400  $\mu\text{m}$ ; buffer thickness fixed at 19  $\mu\text{m}$ .

The most likely fissile particle types for composite fuels are (U,Pu)C and (U,Pu)N, due the combination of high melting temperature and high actinide density. Although a dispersion of nitride fuel particles may exhibit lower fission gas release than the carbides, the same questions related to the use of  $^{15}\text{N}$  in the fuel matrix apply to nitride fuel particles. Chemical compatibility issues favor the use of a nitride coating system (TiN, ZrN) for mixed nitride kernels and a carbide coating system (SiC, ZrC) for mixed carbide kernels. Because of the poor irradiation performance of pyrocarbon at high fast fluence, the use of a low density pyrocarbon buffer layer is questionable. Low density carbide and nitride coatings with low crush strength deposited from non-halide precursors may be more suitable.

There has been some recent development of TiN-based coatings for particle fuels [26]. ZrC has undergone irradiation testing as a coating on TRISO fuel, and may have superior retention of some fission products, especially at high-temperature. [27] There is, however, a much larger database available for fabrication, properties, and irradiation behavior of SiC coatings. [28]

Because of the existing SiC database, SiC coated (U,Pu)C kernels are selected as the reference materials for GFR dispersion fuels. The reference design includes a low density SiC buffer layer, preferably deposited from a non-halide source, and a dense SiC overcoat for fission gas retention.

### 6.4.3 Matrix Selection

A wide variety of initial choices for the matrix phase in a composite fuel are available including refractory metals, transition metals, oxide, carbide, and nitride ceramics as binary, ternary, and higher compounds, and intermetallic compounds. Recent related work on inert matrix fuels for plutonium and minor actinide burning has focused on determining the viability of cercer concepts using oxide matrices for plutonium burning in LWRs. This work has included fabrication studies [29, 30], out-of-pile characterization, and irradiation testing of materials that employ uranium as a fissile surrogate for plutonium. [31, 32].

Requirements for GFR matrix materials are based on GFR performance requirements, Table 6.3 lists GFR fuel matrix material requirements based on Gen IV reactor design goals.

Table 6.3. GFR fuel matrix material reference requirements

Requirement	Reference Value
Melting/decomposition temperature	>2000°C
Radiation induced swelling	< 2% over service life
Fracture toughness	> 12 MPa m <sup>1/2</sup>
Thermal conductivity	> 10 W/mK
Neutronic properties	Materials allow low core heavy metal inventory of less than 15 MT and maintain good safety parameters

Based on these requirements, the list of possible matrix material candidates is narrowed. Figure 6.4 (a) is a depiction of the periodic table. Elements that are gaseous or liquid at room temperature are shaded darkly, those with melting temperatures above ambient but less than

1800°C are noted with an intermediate shade of gray in a solid pattern. Elements with melting temperatures in the range of 1800° - 2000°C are shaded in light gray. Elements that meet the melting temperature criterion of 2000°C or above are left unshaded. (Tc is not considered here as a matrix material because it is radioactive, and there are limited quantities available in separated form for core startup). The transition metals Ti, V, Cr, Fe, Ni and Zr, which are otherwise reasonable to consider as matrix materials, are thus excluded on the basis of inadequate melting temperature and lack of high-temperature creep resistance.

Figure 6.4 (b) considers additionally the impact of material neutronic properties on core heavy metal inventory and safety parameters. Scoping core neutronics studies [33] have shown that the use of the refractory metals Mo, Ta, W, and Re is not practical due to neutronic penalties associated with the high absorption cross sections of these materials that make it difficult or impossible to meet GFR design goals in terms of core heavy metal inventory and core safety parameters. Nb is marginal in this regard, and may be useable as a matrix material in some instances, when the volume can be limited. As discussed above, the combination of Nb cladding and ducts results in the requirement for large core heavy metal mass and degraded Doppler coefficient due to spectral hardening. Another potential option is the enrichment of naturally occurring molybdenum in the isotope <sup>92</sup>Mo, which dramatically decreases the absorption cross section. This is the approach being taken to the development of cermet Am targets as a part of the international FUTURIX-FTA irradiation program in the Phénix reactor. [34] This option has not been seriously pursued due to uncertainties in the cost of implementing molybdenum enrichment technology for large-scale deployment.

Carbon is also neutronically marginal due to the fact that it is a neutron moderator; limited quantities are possible in the core, however consideration of irradiation behavior eliminate carbon in the form of graphite or carbon-carbon composites. These materials exhibit anisotropic swelling under irradiation, resulting in severe degradation of mechanical properties at a dose of 10-15 dpa, far less than the estimated dose of 80 dpa (stainless steel) expected for (non-fissile) fuel materials at the initial GFR goal burnup of 5 % HM. As seen in Figure 6.4 (b), no materials in the elemental state are suitable for achieving GFR goals. This statement also applies in general to metal alloys. A possible exception is the use of niobium metal in small quantities. These considerations drive the choice of matrix materials into the realm of ceramics.

Ceramics, especially carbides and nitrides, tend to have high melting temperatures and excellent high-temperature creep resistance. There are thousands of possible binary, ternary, and higher ceramics based on combinations of elements with carbon, oxygen, nitrogen and sulfur; many of these materials have been poorly characterized with respect to properties. While intermetallic materials are a possibility, they also remain largely unknown in terms of general properties and irradiation behavior, and little can be said about the suitability of these materials for use in the GFR environment. Many of the refractory carbides and nitrides are again disqualified due to unsuitable neutronic properties. Table 6.4 (a) is a list of the more common and well characterized ceramics that meet screening requirements for melting temperature and core neutronics.

The criterion for thermal conductivity was established through the analysis of the stress generated by thermal gradients in a honeycomb matrix. The stresses in the honeycomb structure

were found to be lower than those generated in a solid hexagonal block containing cylindrical coolant channels. Figure 6.5 (a) shows an example result of finite element analysis of the temperature distribution in this body for a uniform power deposition of  $70 \text{ MW/m}^3$ . Figure 6.5 (b) is a plot of the magnitude of the maximum temperature gradient in the body and the magnitude of the maximum principal stress calculated as a function of the bulk thermal conductivity of the matrix. It can be seen that at thermal conductivity values above about  $12 \text{ W/m}\cdot\text{K}$ , matrix stress is a slowly varying function of thermal conductivity. Below this value, matrix stress increases rapidly with decreasing thermal conductivity. The criterion for minimum thermal conductivity was thus set at  $12 \text{ W/m}\cdot\text{K}$ .

Considering the minimum thermal conductivity criterion leads to the elimination of most of the oxides and CeN, as shown in Table 6.4(b). Further applying the criterion for irradiation stability of less than 2 volume percent of swelling during the in-core service life results in elimination of  $\text{Si}_3\text{N}_4$ . Spinel ( $\text{MgAl}_2\text{O}_4$ ) is marginal in this regard, and exhibits high swelling in response to high energy fission fragment damage, MgO has been found to migrate down the temperature gradient during irradiation of spinel-matrix cermets, and so is disqualified. [35] While not strictly an irradiation performance issue, MgO has a high vapor pressure and poor thermal shock resistance, and is thus also disqualified. AlN also exhibits poor irradiation behavior in some temperature regimes (see below), and is considered marginal in this application. No data is available to support the selection of  $\text{YC}_2$ , VC, or YN as matrix materials, so that they are not considered for use in the intermediate term.

After consideration of the screening criteria, a handful of materials emerge that have the potential to meet GFR fuel matrix material requirements. Based on available data, six ceramic materials and niobium have been selected for further study as potential matrix materials and coatings for GFR composite fuel concepts. The ceramics are zirconium carbide (ZrC), titanium carbide (TiC), silicon carbide (SiC), zirconium nitride (ZrN), aluminum nitride (AlN) and titanium nitride (TiN).

Despite common industrial use of many of these candidate matrix materials, there are still large gaps in mechanical and thermal property databases that make the design of a refractory ceramic matrix fuel form difficult. The response of many ceramic materials to neutrons and fission fragments is a complex function of cerker microstructure, irradiation temperature and dose history. Ceramics are also generally brittle and care must be taken that thermal and mechanical stresses in the matrix do not exceed the elastic limit of the material, or matrix cracking may occur, negating a fission product barrier and one of the useful attributes of this fuel. In addition, properties of ceramics are heavily dependent on the microstructure, and thus the route taken to fabrication. With this caution, material properties for the six ceramic materials are presented in Table 6.5. In some cases there are large ranges or ambiguities in available data; these are indicated in the table.

The mechanical strength of ceramics is flaw controlled and thus depends strongly on specimen size and the number density and size of microstructural defects. Well characterized strength and fracture toughness data are not available for many of these materials due to the difficulty in processing the large number of specimens required to obtain statistically significant data, and the lack of microstructural optimization. It can be expected that the strength and fracture toughness



of specimens prepared by conventional powder processing will be similar to that of other materials in this class, ranging from 300-700 MPa when tested in four-point flexure. Fracture toughness and thermal shock resistance are issues that must be addressed for all ceramic materials through the use of microstructural designs that incorporate stable barriers to crack growth into the matrix.

H																	He
Li	Be											B	C	N	O	F	Ne
Na	Mg											Al	Si	P	S	Cl	Ar
K	Ca	Sc	Ti	V	Cr	Mn	Fe	Co	Ni	Cu	Zn	Ga	Ge	As	Se	Br	Kr
Rb	Sr	Y	Zr	Nb	Mo	Tc	Ru	Rh	Pd	Ag	Cd	In	Sn	Sb	Te	I	Xe
Cs	Ba	La	Hf	Ta	W	Re	Os	Ir	Pt	Au	Hg	Tl	Pb	Bi	Po	At	Rn
			Ce	Pr	Nd	Pm	Sm	Eu	Gd	Tb	Dy	Ho	Er	Tm	Yb	Lu	

Figure 6.4 (a). Down-selection of matrix materials based on melting temperature criterion. Elements that are gaseous or liquid at room temperature are shaded darkly, those with melting temperatures above ambient but less than 1800°C are noted with an intermediate shade of gray in a solid pattern. Elements with melting temperatures in the range of 1800° - 2000°C are shaded in light gray. Elements that meet the melting temperature criterion of 2000°C or above are left unshaded.

H																	He
Li	Be											B	C	N	O	F	Ne
Na	Mg											Al	Si	P	S	Cl	Ar
K	Ca	Sc	Ti	V	Cr	Mn	Fe	Co	Ni	Cu	Zn	Ga	Ge	As	Se	Br	Kr
Rb	Sr	Y	Zr	Nb	Mo	Tc	Ru	Rh	Pd	Ag	Cd	In	Sn	Sb	Te	I	Xe
Cs	Ba	La	Hf	Ta	W	Re	Os	Ir	Pt	Au	Hg	Tl	Pb	Bi	Po	At	Rn
			Ce	Pr	Nd	Pm	Sm	Eu	Gd	Tb	Dy	Ho	Er	Tm	Yb	Lu	

Figure 6.4 (b). Down selection of matrix materials based on neutronic and irradiation behavior criteria. Materials that meet other criteria but are neutronicly unacceptable are shaded with a horizontal grid; materials are excluded on the basis of irradiation behavior are shown with a diagonal grid. No elemental materials meet GFR requirements, although Nb is marginal.

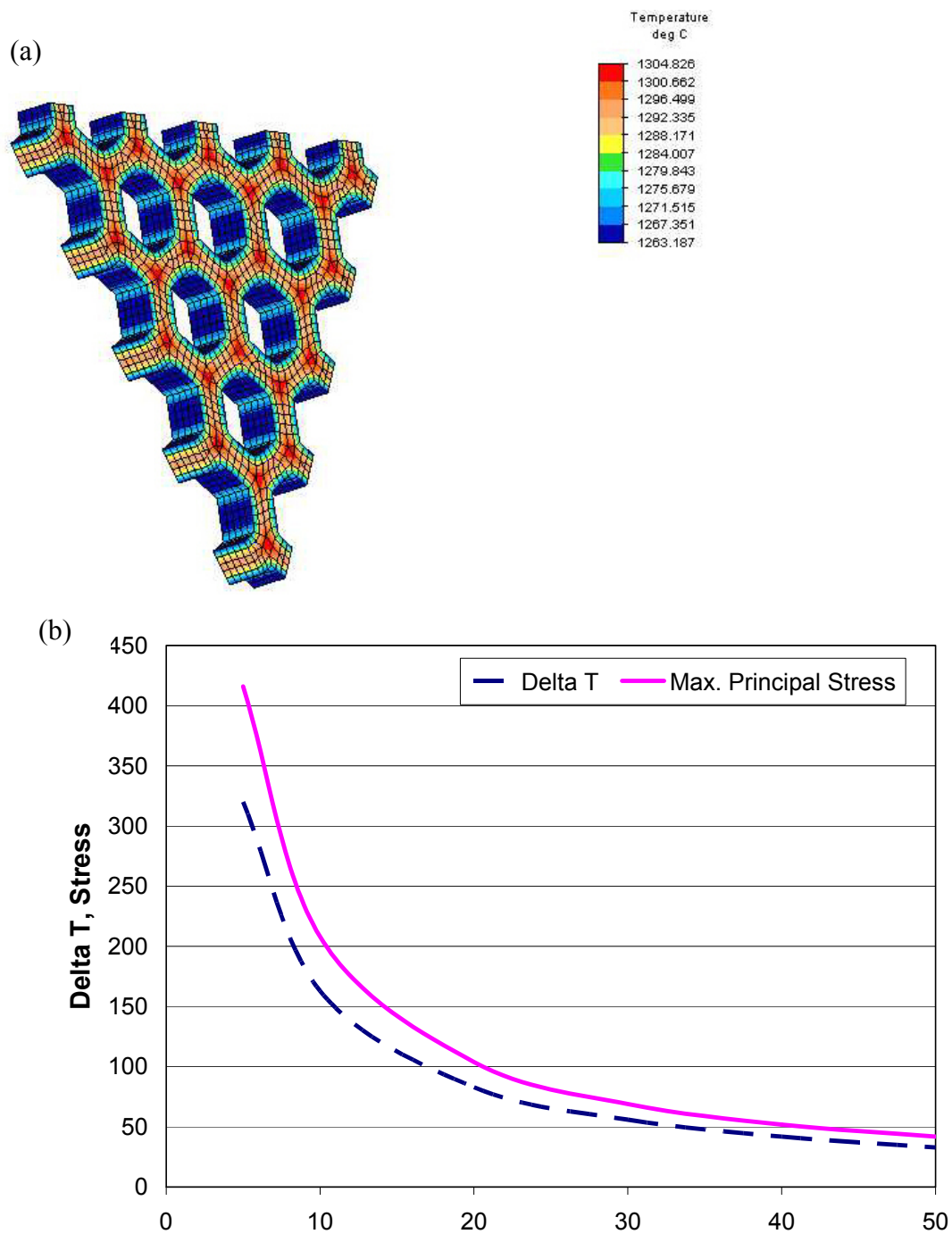


Figure 6.5. Effect of thermal conductivity on thermal gradients and matrix stress for a power density of  $140 \text{ MW/m}^3$ . (a) Example of results of FEA calculation for temperature distribution. (b) Plot of magnitudes of maximum temperature gradient and maximum principal stress.

Table 6.4 (a) Ceramics that meet melting temperature and neutronics requirements.

Oxides	Carbides	Nitrides
Al <sub>2</sub> O <sub>3</sub>	SiC	AlN
CeO <sub>2</sub>	TiC	CeN
MgAl <sub>2</sub> O <sub>4</sub>	VC	Si <sub>3</sub> N <sub>4</sub>
MgO	YC <sub>2</sub>	TiN
Y <sub>2</sub> O <sub>3</sub>	ZrC	YN
ZrO <sub>2</sub>		ZrN

Table 6.4 (b) Ceramics that meet melting temperature, neutronics, and thermal conductivity requirements.

Oxides	Carbides	Nitrides
Al <sub>2</sub> O <sub>3</sub>	SiC	AlN
CeO <sub>2</sub>	TiC	CeN
MgAl <sub>2</sub> O <sub>4</sub>	VC	Si <sub>3</sub> N <sub>4</sub>
MgO	YC <sub>2</sub>	TiN
Y <sub>2</sub> O <sub>3</sub>	ZrC	YN
ZrO <sub>2</sub>		ZrN

Table 6.4 (c) Ceramics that meet melting temperature, neutronic, and irradiation performance requirements.

Oxides	Carbides	Nitrides
Al <sub>2</sub> O <sub>3</sub>	SiC	AlN
CeO <sub>2</sub>	TiC	CeN
MgAl <sub>2</sub> O <sub>4</sub>	VC	Si <sub>3</sub> N <sub>4</sub>
MgO	YC <sub>2</sub>	TiN
Y <sub>2</sub> O <sub>3</sub>	ZrC	YN
ZrO <sub>2</sub>		ZrN

Table 6.5. Summary of properties of candidate GFR matrix materials.

Property	SiC	ZrC	TiC	AlN	TiN	ZrN
Theoretical Density (g/cm <sup>3</sup> )	3.21 ( $\beta$ )	6.51	4.91	3.25	5.42	7.35
Fracture Toughness (MPa m <sup>0.5</sup> )	4-6	--	--	3-4	5	4-7
Elastic Modulus (GPa)	480	400	450	350	250-590	380-510
Shear Modulus (GPa)	162	--	--	--	--	154
Poisson's Ratio	0.17	0.19	--	0.22	0.22	0.26
Flexural Strength @RT (MPa)	700	--	400	300-500	430	--
Compressive Strength @RT (GPa)	4.6	--	0.7-3.0	--	1.3	1.0
Specific Heat Capacity (Range 20-1000°C)(J/kg.K)	700-1300	250-500	550-880	800-1000	800-1000	800-1000
Melting Temperature (°C)	2760	3450	3067	2790 (decomp)	2950	2980
Thermal Conductivity (W/m.K)	40-120	17-36	10-20	100-200	20-60	10-15
Thermal Expansion Coeff. (10 <sup>-6</sup> /°C) (RT-1000°C)	5.3	6.7	8.3	5.0	9.4	7.2

#### 6.4.4 Reference and Alternate Dispersion Fuel Concepts

##### 6.4.4.1 Reference Dispersion Fuel Concept

Because of the acceptable properties of SiC, the large irradiation behavior database, the preference of core designers for SiC over Nb, and the experience in use of SiC as a component in TRISO fuel, a dispersion of (U,PuC) particles coated with a bi-layer SiC coating in a SiC matrix is selected as the reference GFR fuel concept. This selection is made with the realization fuel density is marginal, improvements in fracture toughness are required, as is the potential use of an outer cladding on block-type elements. Fuel parameters are listed in Table 6.6.

Table 6.6. Reference GFR dispersion fuel parameters

Parameter	Reference Value
Fuel particle type	Bi-layer SiC coated (U,Pu)C, Two size distribution (1) 1.64mm diameter (2) 480 $\mu\text{m}$ diameter
Inner coating	Buffer layer of SiC with TD<30% and low crush strength (1) buffer thickness $\sim 58 \mu\text{m}$ (2) buffer thickness $\sim 17 \mu\text{m}$
Outer coating	Dense CVD SiC, (1) thickness $\sim 61 \mu\text{m}$ (2) thickness $\sim 18 \mu\text{m}$
Fuel kernel	(U,Pu)C (1) 1.4 mm diameter (2) 410 $\mu\text{m}$ diameter
Heavy metal density	6 g $\text{HM}\cdot\text{cm}^{-3}$ , 75% particle loading 5 g $\text{HM}\cdot\text{cm}^{-3}$ , 63% particle loading
Matrix	Dense SiC

Outer coating thicknesses have been specified to protect the buffer layer during handling of the coated particles. In order to increase particle packing density, a dual sized distribution of particles is specified.

Fabrication of this fuel type will be difficult due to the high particle loading and the fragile nature of the coated particles, and will require novel processing techniques. The reference fabrication process is infiltration and reaction bonding, as sintering will not be effective and hot pressing will likely damage the thinly coated particles. CVD processing is not likely to be effective in filling the channels within the packed bed.

In order to fabricate the composite fuel, particles may be precoated with a carbonaceous precursor and then assembled into a packed bed or assembled into a packed bed and then infiltrated with a carbonaceous precursor [36]. The precursor is then thermally converted to carbon. After conversion, the matrix is infiltrated with molten silicon, and thermally treated to allow reaction of the silicon with carbon. Many variations on this method may be possible, including substitution of a portion of the SiC outer shell with pyrocarbon in order to encourage bonding of the matrix to the fuel particles, or treating the particles to discourage bonding to the matrix.

The fact that the infiltration technique has been used previously to fabricate fuel that was successfully irradiation tested lends some credibility to the process. Figure 6.6 shows lateral and transverse cross-sectional images of a fuel rod (1.27 cm diameter) consisting of a dispersion of pyrocarbon coated particles in a SiC matrix formed by reaction bonding. [37] This fuel was fabricated and irradiation tested as part of the high temperature AGR (Advanced Gas Reactor) fuel development effort in Great Britain. Irradiation experiments were conducted at temperatures between 750 and 1200°C and rod powers of 39 kW/m in two experiments. Burnup values ranged from 1.6 to 5% FIMA. Fractional fission gas release was measured during low burnup tests, and was found to be on the order of  $10^{-6}$ .

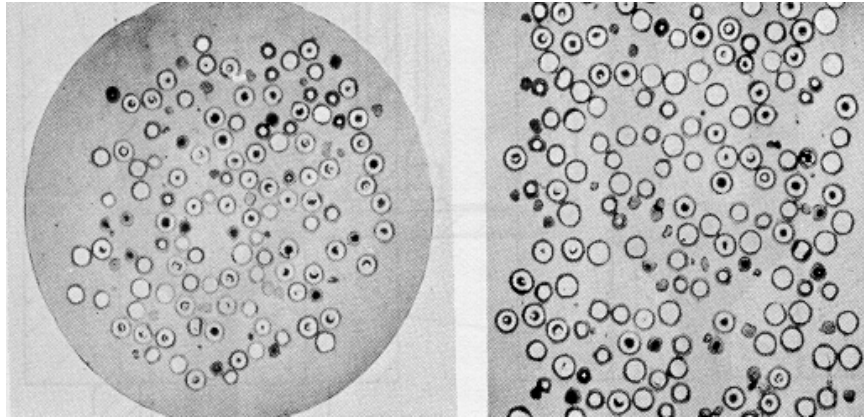


Figure 6.6. SiC matrix coated particle fuel fabricated by reaction bonding.

#### 6.4.4.2 Alternate Dispersion Fuel Concept

Due to the novel nature and uncertainties in irradiation performance of the reference SiC matrix GFR fuel, an alternate dispersion fuel based on a niobium matrix is proposed. This fuel has also been irradiation tested to burnups and temperatures consistent with GFR reference design goals, and at much higher heavy metal densities than SiC matrix fuel. Figure 6.7 shows a postirradiation image of a dispersion of  $\text{UO}_2$  particles in a niobium matrix. <sup>[38]</sup> The fuel loading in this case is 80 percent by volume. The fuel was fabricated by first CVD coating fuel particles with niobium, then isostatically pressing at 1260°C at 10,000 psi (69 MPa) for 3 hours. The fuel was subject to irradiation at a fuel centerline temperature of 1480°C to approximately 4 at.% burnup. After irradiation, the fuel exhibited a density decrease of 1.4%. Fuel heavy metal density in this case is on the order of 6.7 g/cm<sup>3</sup>. It is recommended that this fuel be reevaluated in terms of GFR system neutronic and safety performance.

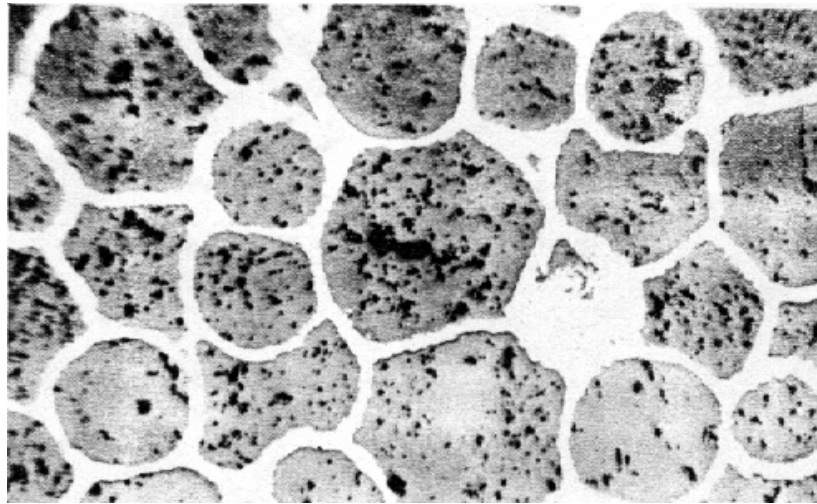


Figure 6.7. Postirradiation metallograph of an 80 vol.% dispersion of  $\text{UO}_2$  in Nb irradiated at  $T > 1400^\circ\text{C}$  to  $\sim 4\%$  burnup.

### ***6.5 Modeling to Determine the Feasibility of MA-bearing GFR Fuel***

There are three major affects that occur due to the presence of large amounts of minor actinides in fuel. These are helium gas generation, a shift in fission product distribution and resultant changes in the nature of chemical interactions between the fuel and cladding or coating layers, and shifts in oxygen potential in the fuel, also related to the fission product distribution. Of these effects, helium generation is likely to have the largest impact at high helium loading. Other factors that are likely to be factors in the determination of fuel behavior and fuel lifetime limits are the change in the fission product chemistry of TRU loaded systems and potentially decreased thermal conductivity at high TRU loadings.

Changes in fission product distribution that result from fission of the heavier actinides. These differences may result in differences in fuel/cladding chemical interaction (or fuel/matrix chemical interaction) behavior. Also possible are changes in nitrogen partial pressure for nitride fuels as a result of an increase or decrease in nitrogen scavenging fission products. Also possible are decreases in thermal conductivity resulting from the incorporation of TRU into the fuel. For example, Fig. 6.8 shows a plot of the thermal conductivity of americium oxide relative to other actinide oxides. Reduction of fuel thermal conductivity would result in increased fuel temperatures and consequently increased gas release.



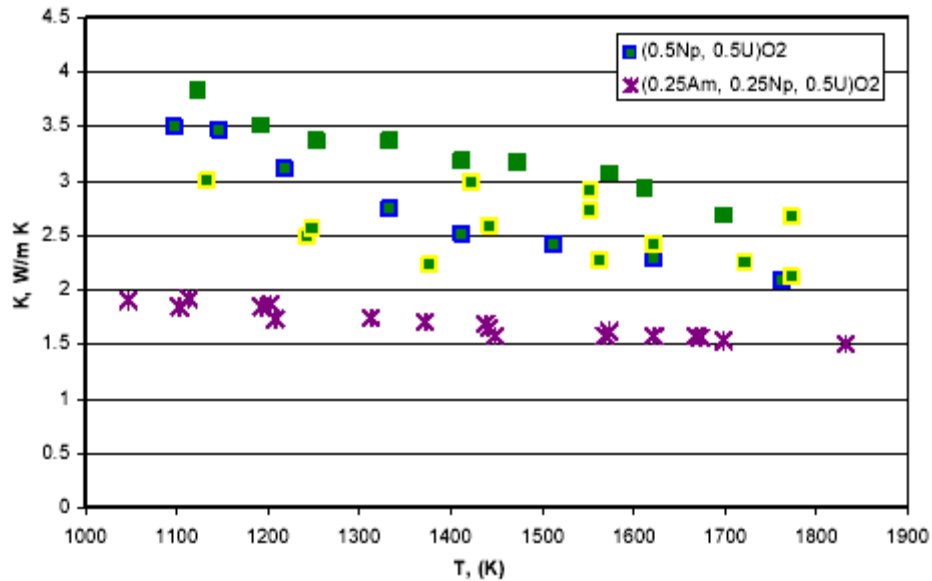


Figure 6.8. Thermal conductivity of Am-bearing oxide fuels relative to U, Pu, and Np oxide fuels. Data: Babelot, JRC-ITU-TN-99/03 (1999)

### 6.5.1 Pin-type fuel

Fuel behavior during core accident conditions drives GFR fuel design. During normal operation, core coolant pressure (7 MPa) offsets cladding tensile hoop stress generated due to fission gas pressurization of the fuel pin. This results in low tensile hoop stress (or compressive stress) in the cladding during normal operation. GFR loss-of-coolant pressure accidents, however, are severe in terms of negative consequences to the fuel. Loss of coolant pressure coupled with a core temperature rise and increased fission gas release results in a large increase in pin internal gas pressure. This increase in internal pressure, coupled with a decrease in external cladding restraint due to depressurization results in a large increase in cladding hoop stress. For metal cladding, this increase in stress is concomitant with a decrease in cladding creep strength due to increased cladding temperature. This scenario results in the potential for a high probability of massive failure of fuels that are conventionally clad in sealed pins. The introduction of americium into the fuel exacerbates this issue by increasing fuel pin gas inventory, leading to yet higher pin failure probability. Fuel pin models that capture the effect of additional gas inventory due to americium on cladding stress can be easily implemented using spreadsheet calculations and/or finite element analysis. Prediction of failure probability is, however, difficult due to the lack of high-temperature irradiation creep data germane to the cladding systems of potential interest. These include Nb-based refractory alloys, ODS alloys, SiC composites, and duplex cladding systems.

Tables 6.7 and 6.8 provide examples of the hoop stress introduced during a loss-of-coolant scenario for a sealed fuel pin originally operating at an average plenum temperature of 650°C at and a burnup level of 10 at.% prior to core depressurization followed by a temperature rise to 1600°C.

Because the fuel is designed to allow pellet to cladding mechanical contact only at end-of-life to prevent fuel-cladding-mechanical-interaction, cladding stress, and thus cladding lifetime, are

driven by gas pressure. Cladding stress can be manipulated by varying the fuel to gas plenum volume ratio. Table 6.7 shows data for a fuel to plenum length ratio of 1:1. It can be seen that under normal reactor operating conditions, the cladding is in compression, and cladding creepdown becomes a potential issue. This is also a phenomenon of concern in pressurized light water reactors, and is addressed by pre-pressurizing the fuel pins with helium gas during fabrication. LWR fuels, however, typically have very low gas release relative to fast reactors due to lower power density and peak fuel temperature. They do not, therefore, tend to exhibit the wide swings in pin internal pressure characteristic of fast reactor fuels operating at much higher power density and temperature. The higher gas release rates and the nature of the core depressurization accident make the use of prepressurized fuel pins problematic for the GFR.

Table 6.7. Example of increase in cladding hoop stress for a (U,Pu)N fuel during postulated core depressurization accident conditions. The fuel to plenum length ratio is modeled as 1:1.

Condition	Cladding hoop stress (MPa)
10% burnup, no Am, normal operation at 8 MPa, 650°	-18.7 (compressive)
10% burnup, no Am, atmospheric pressure, 1600°C	35.6
10% burnup, 2.5% Am, atmospheric pressure, 1600°C	40.5
10% burnup, 5% Am, atmospheric pressure, 1600°C	45.3
10% burnup, 10% Am, atmospheric pressure, 1600°C	55.1
10% burnup, 20% Am, atmospheric pressure, 1600°C	74.5

Table 6.8. Example of increase in cladding hoop stress for a (U,Pu)N fuel during postulated core depressurization accident conditions. The fuel to plenum length ratio is modeled as 2:1.

Condition	Cladding hoop stress (MPa)
10% burnup, no Am, normal operation at 8 MPa, 650°	-20.7 (compressive)
10% burnup, no Am, atmospheric pressure, 1600°C	18.6
10% burnup, 2.5% Am, atmospheric pressure, 1600°C	21.1
10% burnup, 5% Am, atmospheric pressure, 1600°C	23.7
10% burnup, 10% Am, atmospheric pressure, 1600°C	28.8
10% burnup, 20% Am, atmospheric pressure, 1600°C	39.0

The data in Table 6.7 show that the consequences the core depressurization overwhelm the effects due to americium below about 5% Am (percent of heavy metal). At 5% Am, additional gas inventory has a significant impact on cladding hoop stress, increasing cladding stress by approximately 25%. At 20% Am, the cladding stress more than doubles during accident scenarios relative to the case of no americium. The assumed cladding transient stress limit of 20 MPa (2900 psi) for short times at high temperature (1600°C) cannot be met for any fuel design using a short plenum.

Table 6.8 shows data for a plenum to fuel length ratio of 2:1. In this scenario, the cladding transient stress limit can be met for americium levels up to about 2%. A plenum to fuel length ratio of 4:1 would be required to accommodate 20% Am in the fuel. In other words, only 20% of

the length of the cladding tube would contain fuel. Smaller plena are required in liquid metal-cooled systems due to the less demanding nature of anticipated transients.

Increasing the fuel plenum length has the consequences of increasing pressure drop across the core and requiring a much longer core pressure vessel. It may also result in pin vibration issues. The practical limit on plenum to fuel length ratio has not been determined, but is likely to be on the order of 2:1. This would indicate that americium contents on the order of 5 at.% are likely to be possible for this type of fuel.

#### **6.5.1.1 Vented Fuel pins**

Due to the nature of the GFR depressurization accident and the consequent need for large gas plenums to prevent massive pin failure, GFR designs of the 1970's tended toward the use of vented fuel pins as a solution to this issue. Vented pin concepts typically use a long diffusion path length coupled with carbon 'traps' or 'filters' to allow the fuel pins to breath while preventing newly formed fission product release to the core coolant. Pin internal and external pressures are essentially equal, resulting in no net cladding hoop stress and no possibility for gas-driven creep rupture of the fuel pins.

Vented pins offer a solution that would be immune to the effects of additional helium gas production due to the minor actinides. These concepts are difficult to implement in practice, however, resulting in some degree of increased cost and complexity relative to sealed pins. Another potential alternative would be to vent fuel pins through a rupture disk during accident conditions. During normal operation, a plenum to fuel ratio of 1:1 or less would be sufficient to ensure that cladding stress remains at a low level. During a high temperature excursion, a 'rupture disk' fitted to the pin would be designed to release gas to the coolant only when the pin internal pressure rises beyond the rupture disk pressure limit. This would prevent potential flow blockage issues due to 'ballooning' of the cladding from arising during accident conditions. Use of this concept would likely result in a decrease in fuel reliability during normal operating conditions, however.

Modeling of vented fuel concepts offers no additional insight into the behavior of fuels with high minor actinide content, since the principal difficulties with this concept are design interface issues. The life limiting factor for the fuel shifts from internal pressurization to an issue such as cladding corrosion or pellet-cladding-mechanical interaction, which is not yet obvious.

#### **6.5.2 Dispersion Fuel**

Because of the complex microstructure of dispersion fuels, two separate finite element models are required to gauge fuel performance. An element scale model containing all of the microstructural features of a dispersion fuel (millions of particles, hundreds of millions of nodes) would be far too computationally intensive for practical application as a screening tool. Instead, a macroscopic model with no microstructural detail is used to calculate macroscopic thermal stresses and fuel temperatures. A micro-scale model is then used to calculate the local stress state of the fuel element due to gas pressure and fuel particle swelling as a function of americium content. Fuel to coolant ratio was kept constant at 50 vol.% for all concepts. Fuel particle loading was also fixed at 50 vol.%.

### 6.5.2.1 Macroscopic Stress Model

Multiple FEA models were constructed using various configurations of flow channels. A convection coefficient of  $1500 \text{ W/m}^2\cdot\text{K}$  was applied to the surfaces of the flow channels and along the outer edge of the fuel element model to simulate He coolant flow. A constant uniform heat generation rate of  $2.0 \times 10^6 \text{ W/m}^3$  was applied to the solid homogeneous fuel matrix to model the volumetric heat generation due to fission. At a constant coolant volume fraction of 0.5, this results in a core power density of  $100 \text{ MW/m}^3$  at the location of the analysis. An average ambient gas temperature of  $650^\circ\text{C}$  is used in the model calculations. The FEA models were used to complete steady-state thermal and static stress analysis. A typical fuel element model contained 100,000 – 200,000 nodes.

Hexagonal block-type fuels were first modeled as 1/6 segment models for a variety of coolant channel diameters. These elements would be stacked together to form a core similar to the manner in which HTGR elements are assembled.

Larger web thicknesses result in higher peak temperatures and temperature gradients, which result in higher peak stress values as the cylindrical channel diameter increases. Figures 6.9 and 6.10 plot the relationship between the circular coolant channel diameter and the fuel element maximum temperature and the coolant channel diameter and fuel element maximum principal stress for a 1/6 element hexagonal model. Elements modeled with coolant channel diameter less than 1 cm exhibit maximum principal stresses of less than 150 MPa. Maximum element temperature is approximately  $1000^\circ\text{C}$  for 15 cm diameter plates with 1 cm diameter channels.

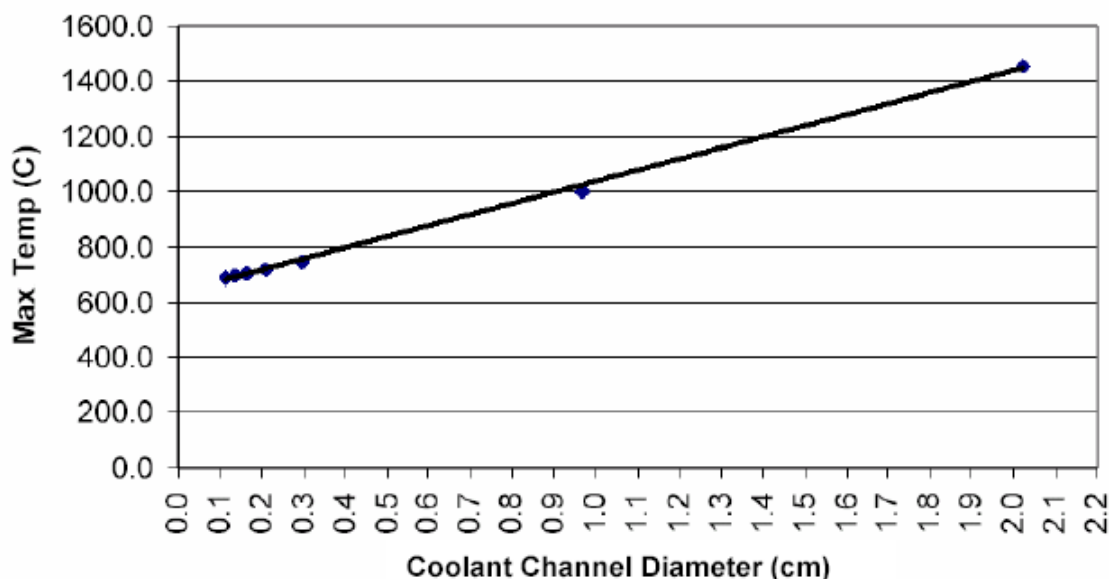


Figure 6.9. Maximum temperature in a '1/6th' hexagonal fuel model as a function of coolant channel diameter.

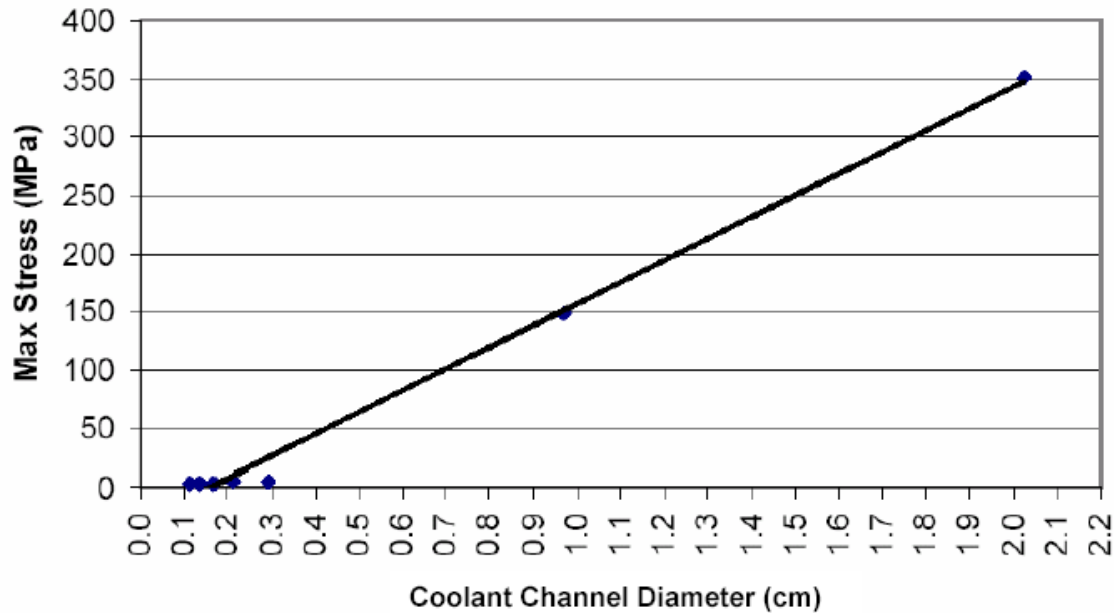


Figure 6.10. Maximum temperature in a ‘1/6th’ hexagonal fuel model as a function of coolant channel diameter.

Based on the results of the 1/6 element hexagonal model, full hexagonal fuel element models were used to further analyze fuel temperatures and the macroscopic thermal and stress distribution across a whole element. Figure 6.11 is an image of the calculated temperature distribution in a full hexagonal model. The steepest temperature gradients, and hence the largest thermal stresses occur at the 6 corners of the hexagon due to ‘over cooling’ of these areas relative to the remainder of the fuel element. To eliminate these areas of high stresses, this material was removed by cutting a 60° wedge of material including the high stress volume from the corners of the hexagon. Figure 6.12 shows that this reduced the stress significantly in these locations, however the location of the peak stress remains in the near surface region of the coolant channels nearest the six corners of the element.

Table 6.9 lists peak temperature and peak maximum principal stress data for full hexagonal fuel element models of differing edge lengths each with 91 cylindrical coolant channels. Data is shown for models with and without modifications to the geometry to reduce stress discussed above; model geometry ‘b’ denotes removal of material at the corners of the hexagon. Results from the hexagonal (full) model indicates that coolant channel diameters of less than 1 cm are required in order to maintain thermal gradients and consequent steady state thermal stresses at a reasonable level.

The large increase of stress calculated for the full hexagonal block model relative to the 1/6 element model requires further design improvement to further decrease the steady state thermal stress. Smaller diameter high aspect ratio elements bundled into a fuel assembly offer a potential alternative design that operate at a lower temperature, lower temperature gradient, and consequently a much lower internal stress level.

Table 6.9. Summary of maximum element temperature and stress for full hexagonal models with varying coolant channel diameters.

Coolant channel diameter (cm)	Model geometry	Max Temp (°C)	Max Stress (MPa)
0.27	a	692.6	23.2
0.27	b	694.3	13.5
1.0	b	1060.5	218.2
2.0	a	1535.1	1044.2
2.0	b	1604.2	607.9

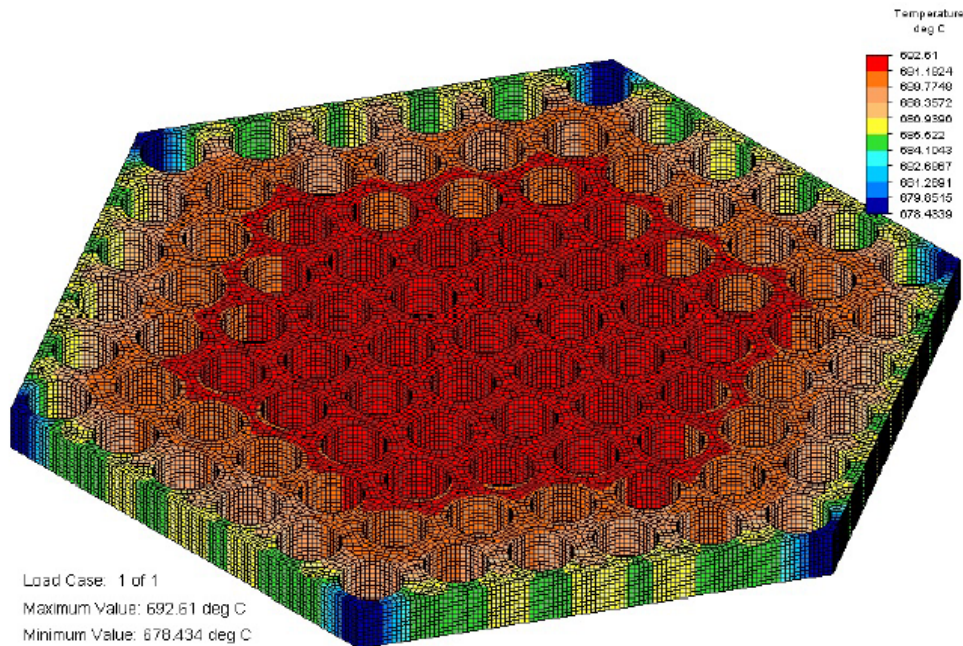


Figure 6.11. Temperature plot of ‘full’ hexagonal fuel element showing largest thermal gradients at the corners of the model (geometry a). 1 cm edge length shown.



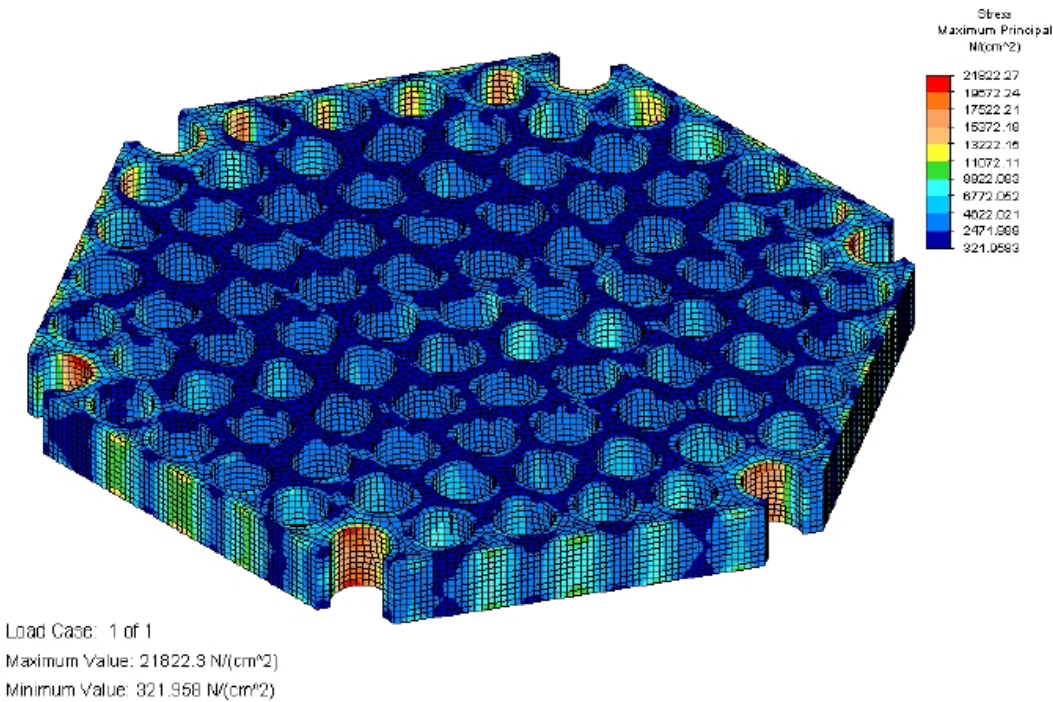


Figure 6.12. Stress plot of ‘full’ hexagonal element model with corners removed to reduce stress in these areas (geometry b) 1 cm edge length shown.

### 6.5.2.2 Microscopic Stress Model

Due to the complex geometry and stress state within the matrix of a dispersion fuel, an analytical solution for stress state is not possible. Finite element modeling was therefore used to assess the state of stress and to make judgments about the relative impact of americium on the stress within a dispersion fuel matrix.

The GFR dispersion fuel was modeled as an array of spherical fuel kernels embedded in a SiC matrix, which acted as a pressure vessel with variable thickness walls. Fuel particle volume fraction was kept constant at 0.5. Stress in the matrix was calculated on the basis of fuel swelling and gas release from the fuel as a function of burnup, temperature, and americium content. Thermal gradients and resulting thermal stresses were calculated using FEA and found to be negligible on the scale of this model and were therefore ignored.

The modeled fuel was roughly equivalent to the reference design in Table 6.6, except that a monomodal kernel size distribution was used. The cavity in the matrix includes the UC spherical kernel and the coating used as a buffer between the fuel and the matrix. The reference design calls for a low density SiC buffer that was modeled to have 50% porosity. The initial volume in the cavity available for gas expansion thus consists of the 50 vol.% void space in the buffer along with the 15 vol.% void space within the volume of an 85% dense (U,Pu)C kernel.

The release rate for fission gas into the dispersion cavity was based on data from irradiation testing of mixed carbide pellet type fuel. Results from U.S. experiments on gas release from fuels with low oxygen content indicate (conservatively) a linear release of 2% per atom percent burnup beyond a threshold burnup value of 3 at.%. Helium gas generation was estimated at 50 ml/g of  $^{241}\text{Am}$  transmuted based on the analysis of available data.

Two models were investigated for modeling the matrix stress; a 3 x 3 x 3 cubic structure consisting of 27 total kernels and a smaller model consisting of only 4 kernels. The smaller 4 kernel model gave results consistent with the 27 sphere model, and was more manageable in terms of computational resources. Figure 6.13 shows an example of the representation of stress output from the 4 kernel model. Here the model has been sliced at the mid-plane to show internal stress. Peak stresses that occur on the edges of the models are due to asymmetry at the model boundary and are ignored. The peak stress relevant to fuel performance determination occurs in the thin web of matrix material located between adjacent particles. The maximum value of principal stress always occurs at this point and was used as an indicator of the response of the matrix stress to increasing americium content.

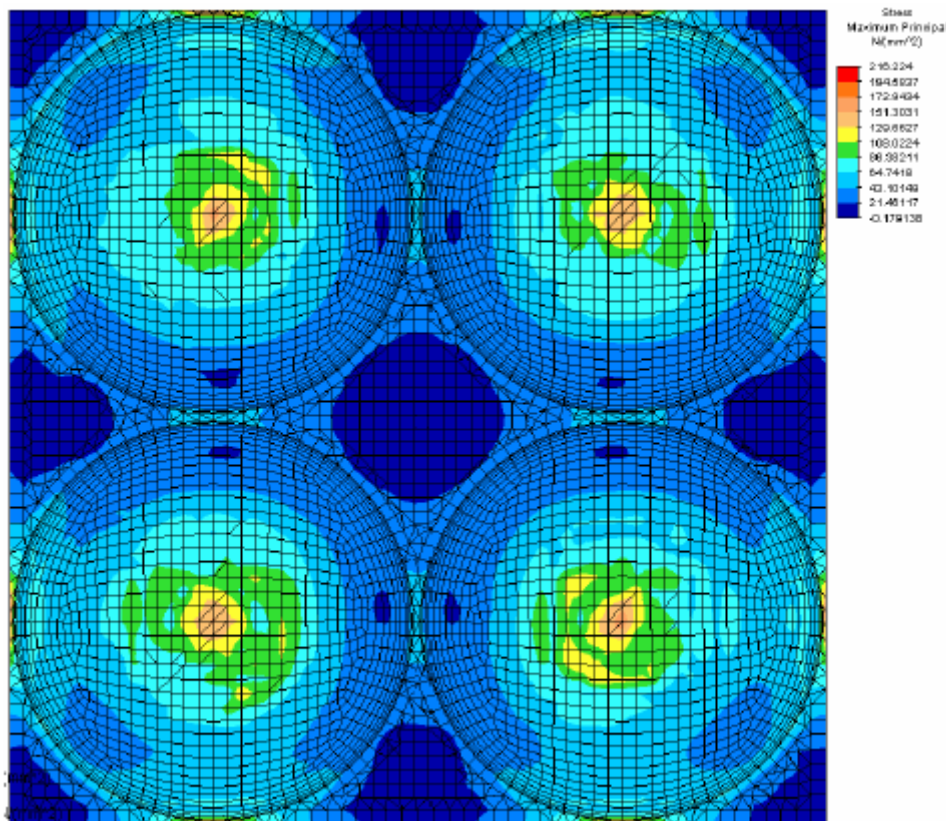


Figure 6.13. Example of stress results from 4 cell dispersion fuel model.

The 4 kernel micro-scale model was used to perform matrix stress analyses at 3 different fuel temperatures (800 °C, 1200 °C, and 1600 °C) and americium contents ranging from 0-10 at.% of heavy metal. Fig. 6.14 provides an example of the evolution of matrix stress as a function of burnup for americium contents of 0-10 at.% (percent heavy metal) at 1200°C. Figure 6.15



provides the same data at 1600°C. Matrix stress increases approximately in an exponential manner with burnup, as total gas inventory and gas release rate increase and fuel kernels swell to fill the space available for gas expansion. Assuming a low modulus buffer layer, no fuel particle to matrix contact occurs below 10 at.% burnup.

The strength of brittle materials (materials with low fracture toughness), such as ceramics, is heavily dependent on the density, size, and location of microstructural irregularities (flaws) in the material. These flaws are invariably introduced during the fabrication process. A rigid analysis of failure probability would require a statistical database consisting of test data for the material being analyzed. The strength of these materials depends not only on the type of manufacturing process used, but also on the geometry of the component (volume under stress) and the specifics of the process, such as origin and impurity levels of feedstock. In the absence of such a statistically database, it is thus very difficult to judge strength limits and failure probability. Rough assumptions are thus used to gauge the likelihood of failure, and somewhat arbitrary stress limit of 100 MPa is used as a yardstick for comparison of various scenarios.

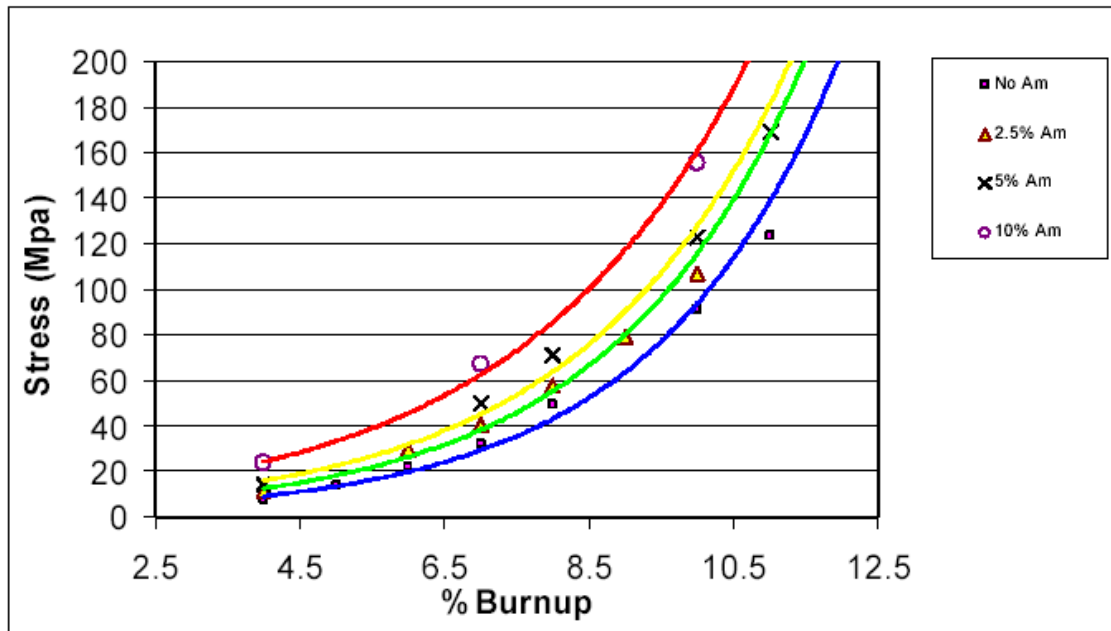


Figure 6.14. Evolution of matrix stress at 1200°C for increasing Am contents.

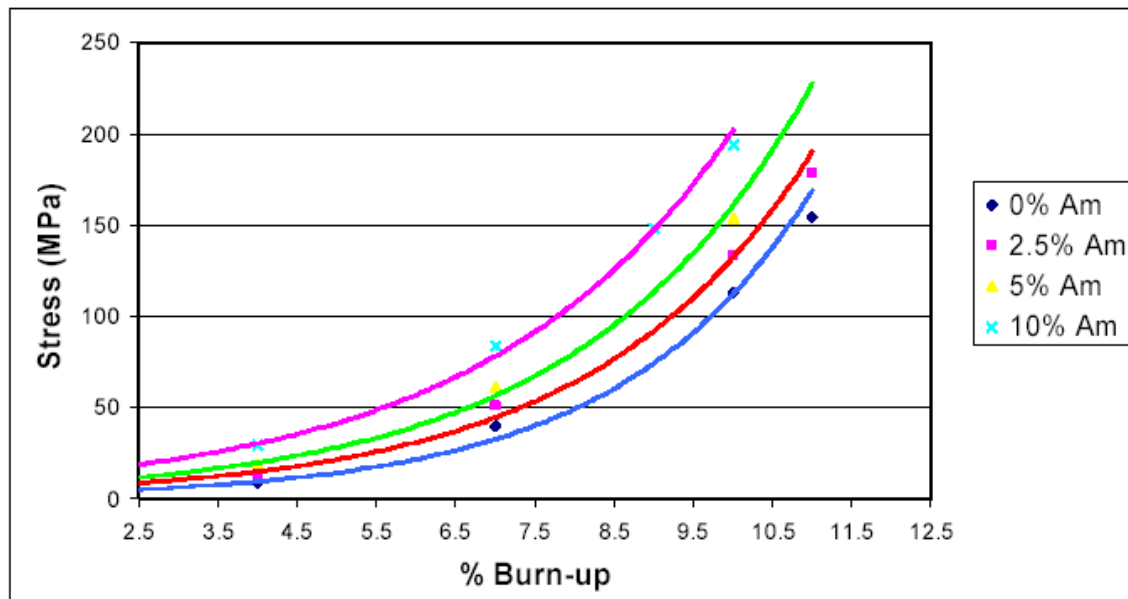


Figure 6.15. Evolution of matrix stress at 1600°C for increasing Am contents.

First considering the case of no americium (Figure 6.14), it can be seen that at an assumed fuel operating temperature of 1200°C, the modeled matrix maximum principal stress levels remain below the 100 MPa target limit for fuel burnup beyond 10 at.%. The spacing of the plotted lines indicates the exponential increase in stress with burnup, as discussed above. The addition of 2.5 at.% Am increases the stress in this case (1200°C and 10 at.% burnup) by approximately 18% relative to the case with no americium. This results in a decrease in burnup potential of approximately 0.6 at.%, assuming that the matrix stress level chosen is a valid indicator of fuel burnup limit. Likewise increasing the Am content to 5 and 10 at.% results in a matrix stress increase of 36% and 71% respectively. Since stress increases exponentially with burnup, when the 100 MPa reference stress limit is applied, decreases in burnup limits of 1.1% and 1.6 at.% result.

Also significant is the behavior of the calculated matrix stress during the 1600°C transient case. Fig. 6.15 shows calculated matrix stress as a function of burnup for americium contents of 0-10 at.% heavy metal at 1600°C. Here the reference stress of 100 MPa is exceeded at about 7.5 at.% burnup for an americium content of 10 at.%. For the case of fuel with no americium, the 100 MPa limit is reached at 9.7% burnup. The intermediate case (5 at.% Am) reached 100 MPa at approximately 8.5% burnup, a decrease of slightly over 1% relative to the case with no americium.

The results of this analysis indicate that americium contents on the order of 5 at.% result in some potential loss of margin under GFR accident conditions, but are in general acceptable. Burnup limits determined on the basis of core accident behavior can be expected to be approximately 1-2% lower than for a fuel containing no americium.

## 6.6 Ion irradiation of ZrC

The most promising candidates for GFR fuel matrix materials are SiC, TiC, ZrC, TiN, and TiC due to a combination of neutronic performance, thermal properties, chemical behavior, crystal structure, and physical properties. The typical properties for ZrC are listed in Table 1. A limited number of ZrC TRISO-type fuel particles have been irradiated to low burnup [39], but detailed post-irradiation analysis of the ZrC layer was not performed. Some ZrC data have been generated under a limited range of irradiation conditions [40, 41]. These studies show a ZrC lattice parameter increase at neutron fluences of  $\sim 1.5 \times 10^{20}$  n/cm<sup>2</sup> ( $\sim 0.2$  dpa). The response of these materials to high dose radiation damage at high temperatures is not known. Heavy ion irradiation tests offer the opportunity to perform low-cost screening studies on a wide range of materials, simulating some aspects of the fission neutron environment. Based on the results of these tests, materials that show large swelling or amorphization under irradiation to dose relevant to GFR fuels can be disqualified from further consideration as inert matrices. ZrC is the first of the five matrix materials listed above to be examined in this manner.

### 6.6.1 Experimental Procedure and Results

Commercial grade ZrC rods made by CERCOM Inc. (Vista, California 92081), fabricated using hot pressing of ZrC powders, with a dimension of 3 mm in diameter and 25 mm in length were used in this work. The density of ZrC rod was measured as 6.58 g/cm<sup>3</sup> with its chemical composition listed in Table 6.10. TEM disc samples were wet-polished using SiC paper down to a thickness around 100  $\mu$ m and then dimpled from both sides to a thickness approximately 10  $\mu$ m in the middle, followed by precision ion milling at an ion energy of 5 keV and 5~7 degree incident angle till perforation.

Table 6.10. Chemical composition of ZrC.

element	Zr	Hf	Ti	Mo	Th	U	Y	Al	others	C
wt%	84.8	1.91	0.19	<0.1	<0.1	<0.1	<0.1	<0.01	<0.01	balance

Irradiation was conducted with 1 MeV Kr ions using an intermediate voltage electron microscope (IVEM) equipped with a tandem accelerator at Argonne National Laboratory. The profile of atomic displacement damage for 1 MeV Kr into ZrC was calculated using the TRIM program [42], figure 6.16, with a default displacement energy of 25 eV for Zirconium and 28 eV for carbon. At peak damage of 3.0 displacement/ion/angstrom at a depth of 200 nm, the ion fluence for a dose of 1.0 dpa was calculated to be  $2.52 \times 10^{14}$  ions/cm<sup>2</sup>. Two TEM disc samples were irradiated at 27°C to doses of 10 and 30 dpa and the two other TEM discs irradiated at 800°C ( $T/T_m=0.29$ ) to 10 and 70 dpa, respectively. The typical dose rate is approximately  $3.0 \times 10^{-3}$  dpa/s. The vacuum level during irradiation was better than  $7 \times 10^{-8}$  torr. During the irradiation, the electron microscope used for imaging was operated at 300 kV and the microstructure evolution was continuously monitored on a CRT screen and recorded on videotape.

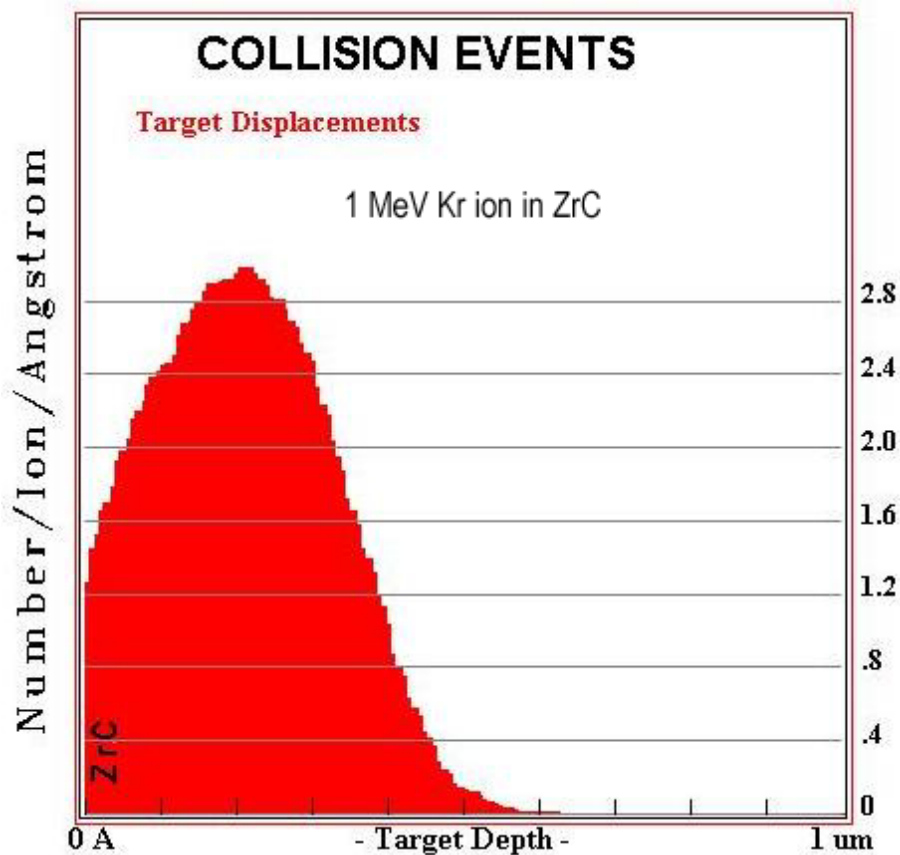


Figure 6.16. Displacement damage profile for 1 MeV Kr ion into ZrC calculated using SRIM 2003 (a Windows version of TRIM). At peak damage ( $\sim 200$  nm depth), ion fluence to reach a dose of 1.0 dpa is calculated as:  $2.52 \times 10^{14}$  ions/cm<sup>2</sup>.

The microstructure of the unirradiated ZrC is dominated by a high density of small black dots that were formed by radiation damage from ion milling, Figure 6.17(a). A few scattered dislocation lines are found in the sample, however most areas are free of dislocation lines as shown in Figure 6.17(b). Rel-rod dark field images did not reveal any faulted loops in the unirradiated ZrC. Bubbles of a size of approximately one nanometer were identified using overfocus or underfocus imaging. These small bubbles are believed due to Ar implantation during ion milling. No precipitates were found in the unirradiated ZrC. The unirradiated ZrC sample has a FCC structure with a measured lattice constant of 0.471 nm. The Kikuchi line pattern due to the inelastic scattering of electrons from atomic planes is clearly visible under the convergent beam diffraction. No ring was observed by electron diffraction. During all four irradiation conditions, a ring pattern appeared at doses as low as 2 dpa with concurrent loss of the Kikuchi patterns in the convergent beam diffraction.

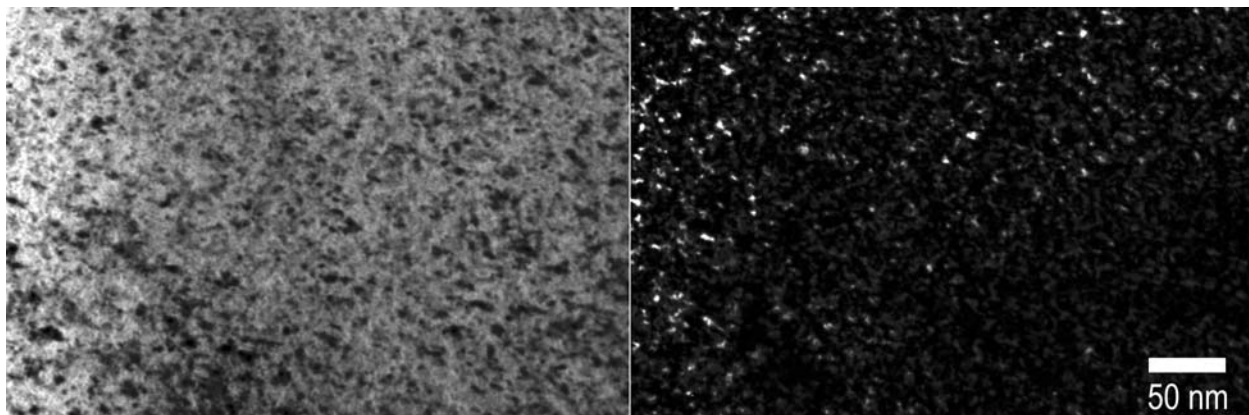


Figure 6.17 (a). Microstructure of unirradiated ZrC imaged with  $g=200$  near zone  $[011]$ . The left is bright field image and the right is weak beam dark field image pair showing black dot damage from ion milling.

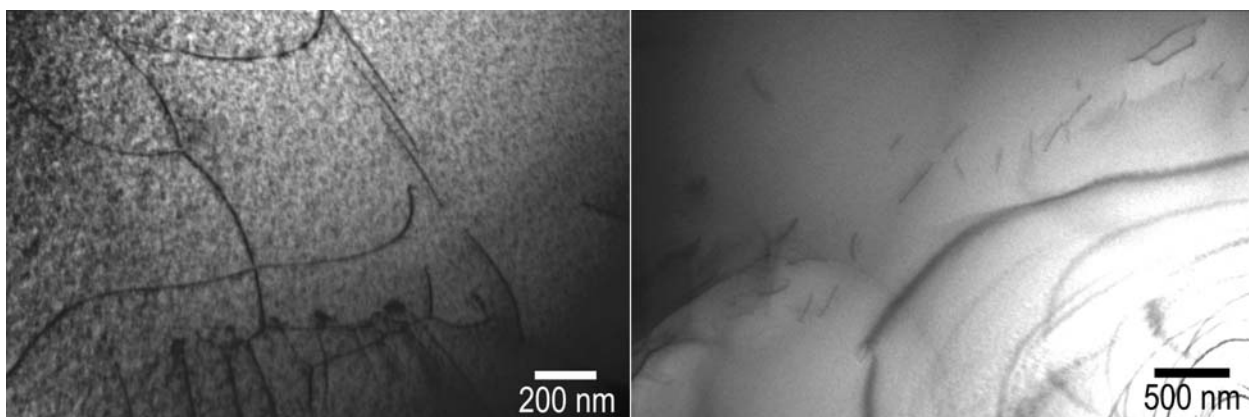


Figure 6.17 (b). Dislocation segments observed in the unirradiated ZrC.

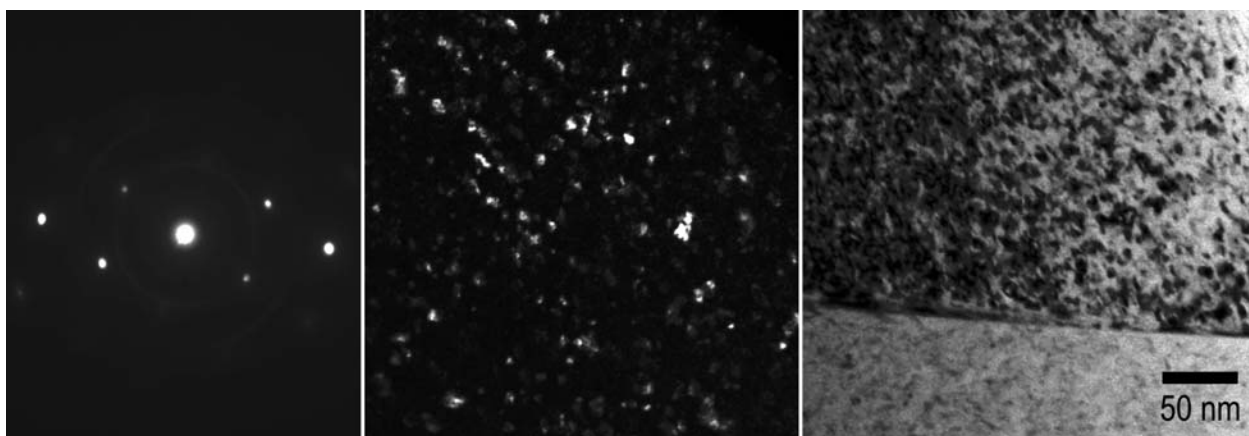


Figure 6.17 (c). ZrC irradiated at room temperature to 10 dpa, showing weak ring pattern (left), the dark field image of precipitates using  $\langle 111 \rangle$  diffraction from the 1<sup>st</sup> ring (middle) and a  $g=200$  bright field image showing dislocations with a grain boundary (right).

Although the damage rate was high, in-situ TEM observation didn't show rapid changes in dislocation structure using two-beam diffraction condition ( $g=200$ ). Sample drifting and tilting due to ion beam fluctuation, stress release and crack formation complicated the in-situ monitoring of the microstructural changes.

For the sample irradiated at 27°C to a dose of 10 dpa, a weak ring pattern of a FCC structure developed with a lattice constant approximately 7% greater than the unirradiated matrix, Figure 6.17(c). Post-irradiation microstructure analysis of rel-rod images did not reveal the faulted dislocation loops on  $\langle 111 \rangle$  type planes although faulted loops would be typically observed as a signature of radiation damage in FCC metals. No micro voids were observed and the small bubbles remained similar to that of the unirradiated condition. The dark field image taken using the  $\langle 111 \rangle$  diffraction of the rings for precipitates and a bright field image ( $g=200$ ) of dislocations is shown in Figure 6.17(c). The dark field image showed precipitates in irregular shapes. The energy dispersive spectrum (EDS) analysis indicated no difference in chemical composition between matrix and precipitates although the detector has large uncertainty for reliable quantitative measurement of carbon content. Measurement of the spacing of diffraction spots indicates a 0.68% increase in lattice constant for the 10 dpa sample compared to unirradiated ZrC.

For ZrC irradiated to 30 dpa at 27°C, the intensity of the ring pattern significantly increased. The ring pattern, dark field precipitate image using the  $\langle 111 \rangle$  diffraction of the rings and the dislocation image ( $g=200$ ) are shown in Figure 6.18(a). The sizes of the rings are the same as the rings observed from 10 dpa ZrC. Similarly, no faulted loops, micro voids or other type of precipitates are observed. Few grain boundary cracks are found. From visual inspection of the micrograph, the sizes and density of precipitates appeared increased than in the 10 dpa sample. Moiré fringes in some large precipitates are clearly visible. The dislocation density in 30 dpa samples appears larger than in the 10 dpa sample. The measurement showed an increase of 0.86% in the lattice constant.

For the ZrC disc samples irradiated at 800°C, the microstructure development was similar to that during irradiation at 27°C. No faulted loops and micro voids are observed for the sample irradiated up to 70 dpa. Figure 6.18 (b) shows the ring pattern and the images of precipitates and dislocations. The sample irradiated at 800°C to 10 dpa has a better ring visibility, and larger precipitate sizes compared to the sample irradiated to 10 dpa at 27°C. The micrograph shows the precipitates in the 800°C\_10dpa sample to have similar sizes but a lower density than the sample irradiated at 27°C to 30 dpa. There is a 0.63% increase in lattice constant. The dislocations in ZrC irradiated to 10 dpa at 800°C seem to have a lower density and large segments than the sample irradiated at room temperature.

For the sample irradiated to high dose (70 dpa), the irradiated microstructure is shown in Figure 6.19(a). The ring pattern in diffraction is more visible than from the sample irradiated at 800°C to 10 dpa, but has less intensity than the sample irradiated at room

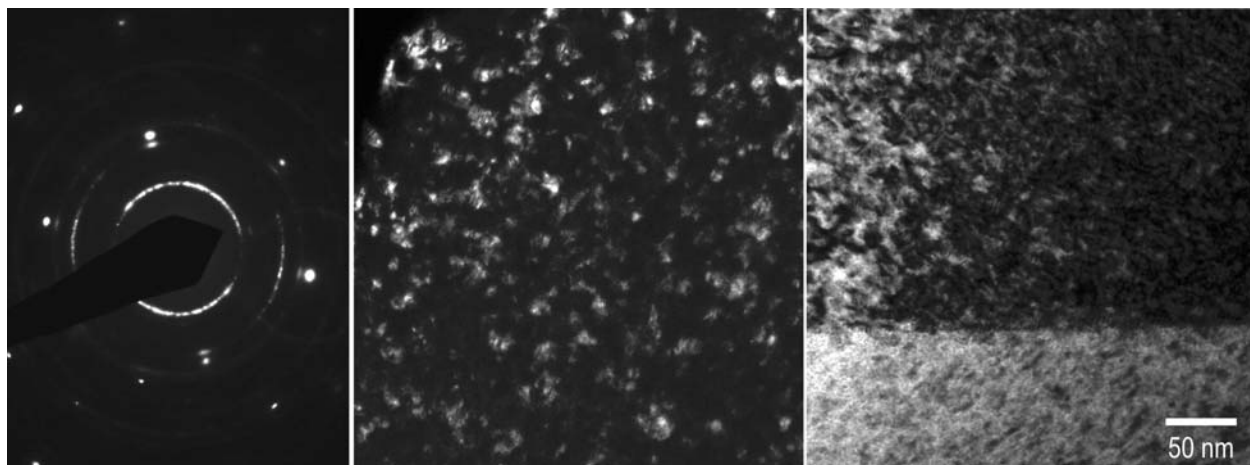


Figure 6.18 (a). ZrC irradiated at room temperature to 30 dpa, showing strong ring pattern (left), the dark field image of precipitates using  $\langle 111 \rangle$  diffraction from the 1<sup>st</sup> ring (middle) and a  $g=200$  bright field image showing dislocations with a grain boundary (right).

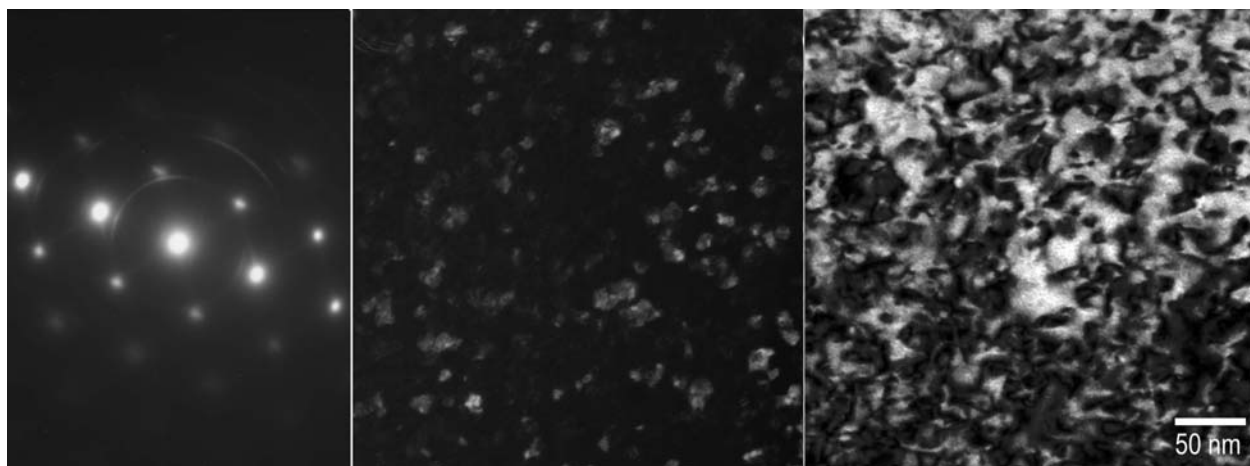


Figure 6.18 (b). ZrC irradiated at 800 °C to 10 dpa, showing ring pattern (left), the dark field image of precipitates using  $\langle 111 \rangle$  diffraction from the 1<sup>st</sup> ring (middle) and a  $g=200$  bright field image showing dislocations (right).

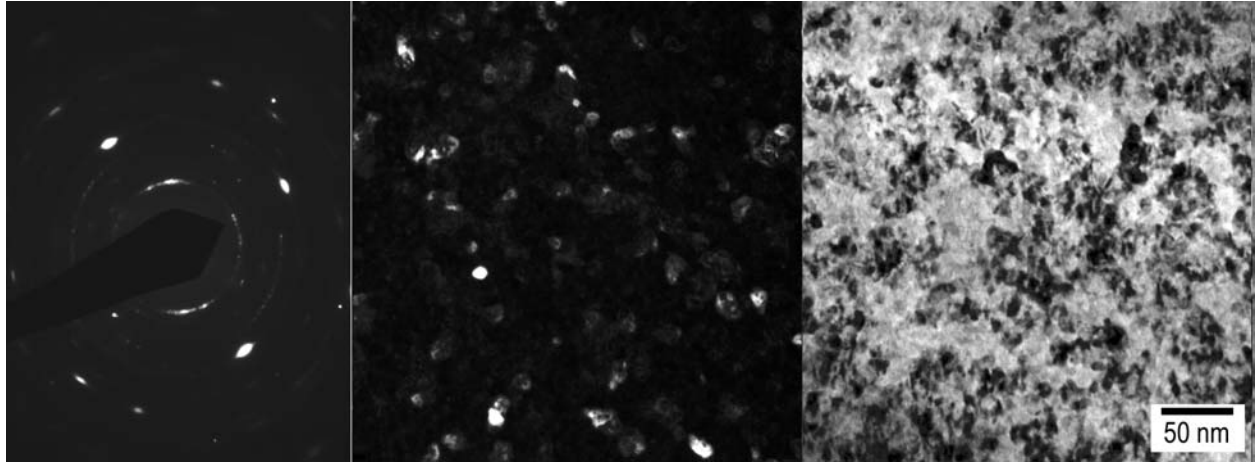


Figure 6.19 (a). ZrC irradiated at 800 °C to 70 dpa, showing ring pattern (left), the dark field image of precipitates using  $\langle 111 \rangle$  diffraction from the 1<sup>st</sup> ring (middle) and a  $g=200$  bright field image showing dislocations (right).

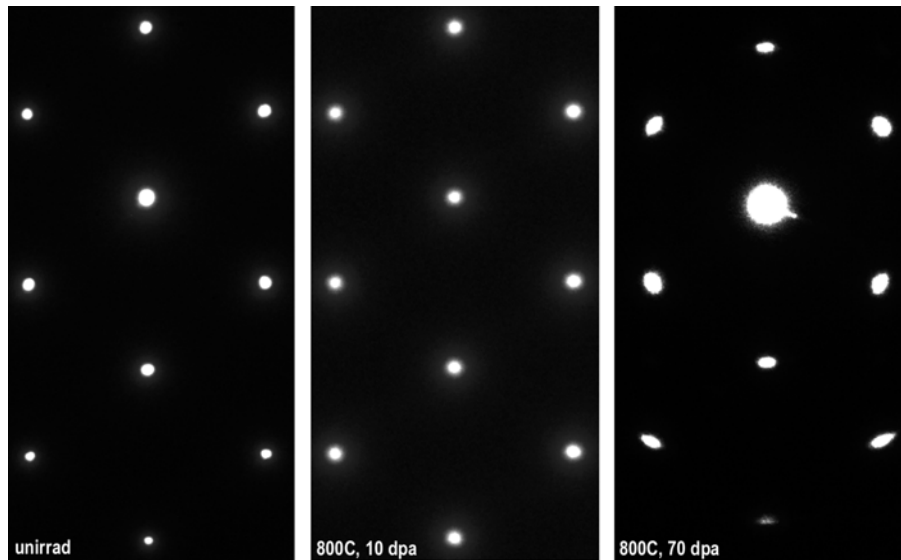


Figure 6.19 (b). Selected area diffraction of zone [011] in ZrC for the unirradiated (left), irradiated to 10 dpa at 800°C (middle) and irradiated to 70 dpa at 800°C (right) showing approximately 7% increase in lattice constant.

temperature to 30 dpa. While the sizes and density of the precipitates looks similar between 10 dpa and 70 dpa at 800°C, there is difference in the dislocation features. The dislocation density appeared decreased in 70 dpa sample compared to the 10 dpa sample irradiated at 800°C. More cracks along the grain boundaries are observed than in the 30 dpa sample irradiated at room temperature. The measurement of the lattice constant indicates a 7.1% increase compared to unirradiated ZrC, Figure 6.19(b).



The results of ZrC irradiated with Kr ions are summarized in Table 6.11. Ring patterns are observed in all the irradiated cases and the sizes of the rings remain the same although the visibility and the intensity of the rings are different for the different irradiation. Strong ring intensity was observed for the irradiation at room temperature to 30 dpa. The ring pattern is generated from FCC precipitates with a lattice constant approximately 7% greater than the unirradiated ZrC matrix. Samples irradiated at 800°C have larger precipitate sizes than in samples irradiated at room temperature. For dislocation segments, the density appeared lower and sizes larger for the samples irradiated at 800°C.

Table 6.11. Summary of radiation effects in ZrC microstructure.

Irradiation		27°C		800°C	
Dose (dpa)	unirradiated	10	30	10	70
Ring in diffraction	Not observed	Weak intensity	Strong intensity	Weak intensity	Weak intensity
Precipitate size density	Not observed	Observed ~ 15 nm low	Observed 15~30 nm high	Observed 15~30 medium	Observed 15~30 medium
Dislocation feature	Black dots, high density	Black dots, high density	Black dots, high density	Small segment, reduced density	Small segment, reduced density
Grain boundary cracks	Not observed	Not observed	Few cracks	Not observed	Several cracks
Lattice constant increase (%)	none	0.68	0.86	0.63	7.1

### 6.6.2 Discussion and Conclusion

ZrC samples irradiated to 10 dpa at both 27°C and 800°C showed similar amount of lattice expansion, 0.68% and 0.63%, respectively. It appears the radiation damage on lattice expansion is not sensitive to the irradiation temperature up to 800°C. The difference in the intensity of ring pattern in diffraction pattern, however, and the sizes of precipitates suggests the development of precipitates is enhanced at higher irradiation temperature. Combining both radiation effects of lattice expansion and precipitate formation, the irradiation to 10 dpa at 800°C produces more damage than irradiation to the same dose at room temperature. One explanation could be that precipitate development is more favorable for the irradiation temperature of 800° for ZrC. The appearance of a ring pattern at doses as low as 2 dpa (in about 11 min) indicates the precipitation is an irradiation driven process. The ZrC sample irradiated to 30 dpa at room temperature showed a significant increase in precipitate density and size compared to the 10 dpa sample, although the amount of lattice expansion is only slightly increased from 0.68% at 10 dpa to 0.86% at 30 dpa. The presence of grain boundary cracks suggests an increase in internal stress and decrease in grain boundary strength. It seems the development of precipitates is responsible to the formation of grain boundary cracks.

Previous work by Keilholtz et al. [43] on ZrC irradiated with neutrons at 300-700°C suggested that lattice expansion results from defect agglomeration. They reported a volume increase of approximately 3% at doses of ~ 3 dpa that remained nearly constant up to a dose of 8 dpa. Their calculated volume increase from lattice expansion was about 1/2 of volume change

measurements, indicating a 0.5% increase in lattice constant at doses of 3~8 dpa. The work by Kovalchenko and Andrievskii on neutron irradiated ZrC to a dose of 0.2 dpa at 50, 150 and 1100°C revealed lattice increases of 0.26%, 0.46% and 0.13%, respectively. The results of this work for ZrC irradiated at 27°C to 10 and 30 dpa or 800°C to 10 dpa are in general agreement with results of neutron irradiated ZrC. There is no microstructure characterization for neutron irradiated ZrC reported in the open literature.

The sample irradiated at 800°C to a dose of 70 dpa had in a 7% lattice expansion compared to the unirradiated ZrC matrix. It is difficult to believe that the 7% increase in lattice constant resulted from point defect agglomeration since the sample irradiated to 30 dpa at 27°C only has a 0.86% expansion in lattice. Note that two parallel processes occurring during irradiation. One is radiation induced defect accumulation which leads to the slow increase in lattice expansion and the other is the radiation driven precipitation which leads to a new phase of FCC ZrC with a lattice constant 7% greater than the unirradiated ZrC matrix. It may be possible that at 70 dpa, the ZrC has nearly completed a transition to a new phase with a 7% greater lattice constant. However, there remains a critical question as to why such an FCC phase does not exist after the fabrication of ZrC.

Bubbles preexisted in the ZrC due to extensive ion milling damage did not grow into micro voids even at irradiation with 1 MeV Kr ions to 70 dpa at 800°C. Kr implantation during irradiation did not occur in this work. The lack of micro voids in the irradiated ZrC suggests the material is highly resistant to void swelling. The lack of faulted loops in the irradiated ZrC at 27°C and 800°C suggest that ZrC has very different response to radiation than FCC metals. The change in the dislocation structure in 70 dpa samples is likely due to annealing. Since the unirradiated ZrC does not contains copper, the presence of Cu precipitates in ZrC irradiated to 70 dpa at 800°C is believed due to the sputtering of Cu out of microscope objective aperture (made of copper) onto the ZrC during the lengthy 70 dpa irradiation.

Irradiation produces point defects and defect clusters in the material. Evolution of these defects and clusters under radiation-enhanced diffusion, plus the interactions of these defects with various sinks, determines the irradiated microstructure. The crystal structure of ZrC can be envisioned as a FCC lattice of Zr with C filling in the octahedral interstitial sites. According to the work of Li et al [<sup>44</sup>] on the interatomic potential of ZrC, the properties of ZrC are dominated by the strong covalent bonds. The weak ionic bonds between Zr and C and metallic Zr-Zr bonds can be neglected. The strong covalent bonding between Zr and C, plus the occupying of the octahedral interstitial sites in FCC Zr by C atoms, make the ZrC respond different to irradiation than a typical FCC metal. It is possible that this unique structure and strong chemical bonding may significantly slow down the diffusion and increase the formation energy for nucleation of voids and faulted loops.

From the above analysis, precipitation is likely a direct product of cascade processes, consistent with the early appearance of diffraction ring pattern at dose as low as 2 dpa (roughly 11 min irradiation time). The irradiation of ZrC at 800°C to 70 dpa may have rearranged the precipitates into new phase with a lattice constant the same as the precipitates. The details of this proposed process need further investigation. Post irradiation microstructure characterization at doses between 10 dpa and 70 dpa at 800°C irradiation will be needed. The stretch of diffraction spots

at 70 dpa and the missing of Kikuchi lines in convergent beam diffraction compared to the unirradiated ZrC suggest there is significant amount of disordering of atomic rearrangement in the 70 dpa ZrC. The presence of grain boundary cracks at 30 dpa (27°C) and 70 dpa (800°C) indicates the large amount stress.

## **6.7 GFR Program Documents**

Two documents were submitted to complete milestones: “GFR Five-Year Fuel Research and Development Plan” (ANL W7520-0677-ES-00), and “Report on the Feasibility of GFR Fuel for Minor Actinide Management.”

## **7. GFR Fuels Support**

### **7.1 Fuel Material Interactions**

Fuel material interaction studies were performed on the oxidation of UC and UN for the case of air ingress, or CO<sub>2</sub>/fuel interaction when CO<sub>2</sub> is used as either the primary coolant, or the makeup coolant in an ECCS. The studies found the following:

- Oxidation of UC and UN involves a volume increase. However, UN is reported to be considerably more stable to oxidation (in hot water) than UC. (E.H.P. Cordfunke, “The Chemistry of Uranium”, Elsevier [1969].)
- Experiments were conducted and analyzed on the oxidation of UC and US, and UCUS molecular mixtures by CO<sub>2</sub>. It was found that over time spans measured in hours the subject materials were oxidized to UO<sub>2</sub>. In particular, US did not significantly protect against oxidation under conditions that would be encountered in GFR fuel elements having cladding defects.

The results of the experiments showed that oxidation of both the UC reference fuel, and UN backup fuel, will occur and produce uranium oxides. Details of the work can be found in the MIT report, “Fuel Material Interactions,” MIT-GFR-011, published in March 2004.

### **7.2 ATR Calculations and Irradiations**

Irradiations of candidate fuel matrices were initiated, which can also be used as core structural materials. The GFR samples utilized the current set of AFCI irradiations being performed in the ATR, where the “dummy” capsules were replaced with the candidate materials. This includes the refractory ceramics, and a few high temperature metals. Below is a list of the fuel matrix/cladding materials being irradiated, and a summary of the work performed under this task:

- Ceramics: SiC, TiC, ZrC, TiN, ZrN, AlN
- Metals/alloys: T122, 800H, MA754 (ODS), MA957 (ODS)
- ATR support calculations for the GFR-F1 irradiations were performed, per experiment requirements.
- The GFR-F1 fuel matrix materials were inserted in the ATR for irradiation on February 24, 2004 in the east flux trap (EFT).
- GFR-F1-1 samples were removed in August 2004 and were visually inspected.

- GFR-F1-2 samples will remain in the EFT of the ATR for the duration of the AFC-1 campaign, on a space available basis.

## 8. References

1. T.Y.C. Wei and J. Rouault, "Development of Generation IV Advanced Gas-Cooled Reactors with Hardened/Fast Neutron Spectrum", International Nuclear Energy Research Initiative Project, 2001-002-F Proposal, U.S. Department of Energy.
2. G. Rimpault et al., "GFR 012 – Core Neutronics Design for Tradeoff Studies," report, issued under Project 2001-002-F of International Nuclear Energy Research Initiative, U.S. Department of Energy, January 2004.
3. U.. Mertyurek, R.B. Vilim, J.E. Cahalan, "GAS-PASS/H: A Simulation Code for Gas Reactor Plant Systems," submitted, Proceedings of ICAPP'04, Pittsburgh, PA, USA, June 13-17, 2004.
4. R.B. Vilim, "Passive Full Power Safety," Report GFR-016, January 2004, Development of Gen IV Advanced Gas Cooled Reactor with Hardened/Fast Neutron Spectrum, International Nuclear Energy Research Initiative #2001-002-F.
5. D. Carosella, personal communication, General Atomics, San Diego, CA.
6. R.B. Vilim, "Gas Reactor Plant Simulation Code," ANL Intra-Laboratory memo, September 25, 2003.
7. L.L. Snead, J.W. Klett, "Ceramic Composites for Structural Applications," *Proc. GLOBAL 2003*, American Nuclear Society (2003) 1077-1078.
8. see for example B.J. Makenas, J. W. Hales, A.L. Ward, "Fuels Irradiation Testing for the SP-100 Program," *Proc. 8<sup>th</sup> Symposium on Space Nuclear Power Systems*, AIP (1991) 886-891.
9. E.A. Hofman, T.A. Taiwo, "Physics Studies of Preliminary Gas-Cooled Fast Reactor Designs," *Proc. GLOBAL 2003*, American Nuclear Society (2003) 82-91.
10. Gamma Engineering Proposal to DOE for FY-2003 SBIR Phase 1 Solicitation, "Development of a Hybrid SiC/SiC Ceramic Composite for Gas Cooled Fast Reactor Fuel Cladding and Core Structural," January, 2003.
11. D. Smith, P. McIntyre, B. Basaran, M. Yavuz, "SiC Composite: A New Fuel Cladding for High-Temperature Cores," *Proc. GLOBAL 2003*, American Nuclear Society (2003) 1821-1823.
12. S.J. Zinkle, "Nonfissile Ceramics for Future Nuclear Systems," *Proc. GLOBAL 2003*, American Nuclear Society (2003) 1066-1067.
13. L.P. Hatch, W.H. Regan, J.R. Powell, "Fluidized Bed for Rocket Propulsion," *Nucleonics* 18 [12] (1960) 102.
14. A.C. Marshall, "A Review of Gas-Cooled Reactor Concepts for SDI Applications," Sandia report SAND-87-0558 (1989).
15. J.R. Powell, H. Ludewig, F.L. Horn, K. Araj, R. Benenati, O. Lazareth, G. Slovik, M. Solon, W. Tappe, J. Belisle, B. Short, R. DeMars, C. Caldwell, W. Pettus, R. Zavadowski, R. Boyle, A. Pietsch, "Nuclear Propulsion Systems for Orbit Transfer based on the Particle Bed Reactor," *Space Nuclear Power Systems 1988*, Eds. M.S. El-Genk, M.D. Hoover, Orbit Book Company, Malabar, FL (1989) 185-198.

16. H. Ludewig, J.R. Powell, M. Todosow, G. Maise, R. Barletta, D.G. Schweitzer, "Design of Particle Bed Reactors for the Space Nuclear Thermal Propulsion Program, *Prog. Nucl. Energy*, Vol. 30, No. 1 (1996) 1-65.
17. M. Konomura, T. Saigusa, T. Mizuno, Y. Ohkubo, "A Promising Gas-Cooled Reactor Concept and its R&D Plan," *Proc. GLOBAL 2003*, American Nuclear Society (2003) 57-64.
18. INERI GFR Project CEA/ANL Technical Workshop, Cadarache, France October (2002).
19. see for example, J.D.B. Lambert, "Irradiation Study of  $\text{UO}_2$ -Stainless Steel and  $(\text{Pu,U})\text{O}_2$ -Stainless Steel Cermet Fuels in Rod and Plate Geometry," p. 237-254 in *High Temperature Nuclear Fuels*, Metallurgical Society Conference Vol. 42, ed. A.N. Holden, Gordon and Breach (1966).
20. D.L. Keller, G.W. Cunningham, W.E. Murr, E.O. Fromm, D.E. Lozier, "High-Temperature Irradiation Test of  $\text{UO}_2$  Cermet Fuels," report BMI-1608 (1963).
21. W.C. Thurber, F.R. McQuilkin, E.L. Long, M.F. Osborne, "Irradiation Testing of Fuel for Core B of the Enrico Fermi Fast Breeder Reactor," report ORNL-3709 (1964).
22. Neeft, E.A.C., Bakker, K., Schram, R.P.C., Conrad, R., Konings, R.J.M., "The EFTTRA-T3 Irradiation Experiment on Inert Matrix Fuels," *J. Nucl. Mater.* **320** (2003) 106-116.
23. Georgenthum, V., Chauvin, N., Pelletier, M., Noitor, J., Berlanga, C., Brenet, D., "Influence of the Microstructure for Inert Matrix Fuel Behaviour: Experimental Results and Calculations," Proceedings of the GLOBAL 99 International Conference on Future Nuclear Systems, Jackson Hole, WY USA August 29-September 3, (1999).
24. Nitani, N., et al., "In-pile irradiation of rock-like oxide fuels", *J. Nucl. Mater.* **319** (2003) 102.
25. Noirot, J., Desgranges, L., Chauvin, N., Georgenthum, V., "Postirradiation Examinations of THERMHET Composite Fuels for Transmutation," *J. Nucl. Mater.* **320** (2003) 117-125.
26. R.A. Lowden, J.C. McLaughlin, J.R. Kelley, "Nitride Ceramic Coatings for Gas-Cooled Fast Reactor Particle Fuel," *Proc. GLOBAL 2003*, American Nuclear Society (2003) 523-524.
27. Minato, K., Ogawa, T., Fukuda, K., Sekino, H., Kitagawa, I., Mita, Naoaki, "Fission Product Release from ZrC-coated Fuel Particles During Postirradiation Heating at 1800 and 2000°C," *J. Nucl. Mater.* **249** (1997) 142-149.
28. For a comprehensive review of the state of the art with respect to coated particle fuels circa. 1977 see, *Nucl. Tech.* **35**, No. 2 (1977).
29. Kurina, I.S., Moseev, L.I., "Fabrication and Study of the Properties of  $\text{PuO}_2$ - $\text{MgO}$ ," *Atomnaya Energiya* vol. 82, No. 5 (1997) 355-358.
30. Fernandez, A., Konings, R.J.M., Somers, J., "Design and Fabrication of Specific Ceramic-Metallic Fuels and Targets," *J. Nucl. Mater.* **319** (2003) 44-50.
31. Proceedings of the 8th Inert Matrix Fuel Workshop (IMF-8), *J. Nucl. Mater.* **319** (2003) 1-187.
32. Proceedings of the 2nd Seminar on European Research on Materials for Transmutation, *J. Nucl. Mater.* **320** (2003) 1-176.
33. INERI GFR Project CEA/ANL Technical Workshop, Cadarache, France, March (2003).

34. S. Pillon, N. Schmidt, E. Abonneau, Y. Croixmarie, L. Donnet, S. Hayes, M. Meyer, K. Chidester, B. Margevicius, A. Fernandez, D. Hass, "The FUTURIX-FTA Experiment in Phenix," *Proc. GLOBAL 2003*, American Nuclear Society (2003) 220-227.
35. Nitani, N., et al., "In-pile irradiation of rock-like oxide fuels", *J. Nucl. Mater.* **319** (2003) 102.
36. see for example E.E. Hucke, U.S. Patent 3,859,421, "Methods of Producing Carbonaceous Bodies and the Products Thereof," Jan. 7, 1975.
37. J.V. Shennan, "Dispersed Ceramic Fuels for the Advanced Gas-Cooled Reactor," p. 96-110 in Preparation of Nuclear Fuels, Nuclear Engineering Part XVIII, eds. A.D. Tevebaugh and D.L. Keller, Chemical Engineering Progress Symposium Series No. 80, Vol. 63 (1967).
38. D.L. Keller, G.W. Cunningham, W.E. Murr, E.O. Fromm, D.E. Lozier, "High-Temperature Irradiation Test of UO<sub>2</sub> Cermet Fuels," report BMI-1608 (1963).
39. K. Minato, T. Ogawa, K. Fukuda, H. Sekino, I. Kitagawa, N. Mita, *J. Nucl. Mater.* 249, (1997) 142-149.
40. Andrievskii, R., et al., 1978, *Izv. Akad. Nauk SSSR, Neorg. Mater.* Vol. 14, pp 680-83.
41. Kovalchenko, M., Rogovoi, Y., 1973, *Izv. Akad. Nauk SSSR, Neorg. Mater.* Vol. 9, pp 321-22.
42. J.F. Ziegler, J.P. Biersack and U. Littmark, *The Stopping and Range of Ions in Solid*, Pergamon Press, New York, 1996.
43. G.W. Keilholtz, R.E. Moore, and M.F. Osborne, *Nuclear Application*, 4 (1968) 330.
44. J. Li, D. Liao, S. Yip, R. Najafabadi, L. Ecker, *J. Appl. Phys.*, Vol. 93, No. 11 (2003) 9072.